# Préparation et caractérisation de nanoparticules de semi-conducteurs pour application dans la photocatalyse et les capteurs de gaz.

Sabri Ouni

Université Claude Bernard Lyon 1

**THESE de DOCTORAT DE**
**L'UNIVERSITE CLAUDE BERNARD LYON 1**
**EN COTUTELLE AVEC L'UNIVERSITE DE MONASTIR**

**Ecole Doctorale** N° 206
**Chimie, Procédés, Environnement**

**Discipline** : Physique des matériaux et nanostructures

Soutenue publiquement le 08/12/2023, par :

**Sabri OUNI**

# Préparation et caractérisation de nanoparticules de semi-conducteurs pour application dans la photocatalyse et les capteurs de gaz

Devant le jury composé de :

| | | |
|---|---|---|
| Présidente de jury : | Mme BORDES Claire | Professeure, Université Lyon 1, Lyon |
| Rapporteurs : | Mme. Hafsa KORRI-YOUSSOUFI | Directrice de recherche CNRS, France |
| | Mr. Wissem DIMASSI | Professeur, CRTEn, Tunisie |
| Examinateurs : | Mme DEBEDA Hélène | Maître des Conférences, Université de Bordeaux, Bordeaux |
| | Mr. Hassen FREDJ | Professeur, Université de Monastir, Tunisie |
| Directeur de thèse : | Mr. Abdelhamid ERRACHID | Professeur, Université UCBL, France |
| Co-directeur de thèse : | Mr. Mohamed HAOUARI | Maitre des conférences, Université de Monastir, Tunisie |
| Invitée | Mme. Nicole JAFFREZIC-RENAULT | Directrice de recherche émérite CNRS, France |

## Résumé :

Depuis quelques années, les NCs binaires ont connu un développement exponentiel grâce à leurs intéressantes propriétés, notamment, leur photoluminescence qui peut non seulement être contrôlée par leur taille mais également par leur composition. Dans le cadre de cette thèse, nous avons développé une nouvelle méthode de synthèse en milieu aqueux de NCs de ZnS par voie colloïdale. Nous avons tout d'abord commencé par la synthèse des nanocristaux de Sulfure de Zinc (ZnS) en utilisant l'acide thioglycolique (TGA) comme stabilisant. Ces nanocristaux de ZnS-TGA ont été utilisés comme alternative peu coûteuse et respectueuse de l'environnement pour la photodégradation du bleu de méthylène (MB) et de l'orange de méthyle (MO) à partir de solutions aqueuses par irradiation solaire. L'activité photocatalytique des nanocristaux de ZnS-TGA sous irradiation solaire pour dégrader les colorants MB et MO testés et leur mélange dans des solutions aqueuses a été évaluée. Une efficacité élevée de dégradation du colorant a été obtenue en très peu de temps (27 min) et cette performance a été attribuée à la charge de surface négative, à la surface, aux défauts de surface et à la forte dispersion des nanocristaux de ZnS-TGA sur le milieu aquatique. Ensuite, nus rapportons une voie facile et verte pour une nouvelle synthèse de nanoparticules de ZnS à l'aide d'extrait de plante d'Artemisia Herba Alba (AHA) pour une adsorption/photodégradation efficace du colorant bleu de méthylène. Les résultats ont montré un décalage vers le bleu dans la bande d'absorbance et des valeurs de bande interdite d'énergie plus élevées que les matériaux ZnS massifs, ce qui était dû aux effets de confinement quantique. Ces NCs vertes de ZnS-AHA ont montré une surface spécifique de 36,82 cm2 $g^{-1}$ et une capacité d'adsorption de 31,17 mg $g^{-1}$ pour bleu de méthylène. Les performances de dégradation photocatalytique des nanoparticules vertes sous irradiation solaire ont montré un taux de dégradation remarquable du colorant de 94,09 % en 180 min. Enfin, capteur de gaz à base des nanocristaux de ZnS-AHA est proposé pour la détection de vapeur de méthanol. La partie sensible de ce microcapteur de méthanol est préparée par encapsulation de nanoparticules de ZnS dans le chitosane. Un film mince de composite chitosane/ZnS-NPs a été électrodéposé sur les électrodes d'or interdigitées par essai chrono-ampérométrique. Les réponses de détection de gaz d'éthanol, de méthanol et d'acétone des films ont été mesurées à température ambiante, par des mesures conductométriques différentielles à 10 kHz. Le temps de réponse des capteurs ($t_{Rep}$) pour le méthanol est de 11 à 25 s des concentrations les plus faibles aux plus élevées. La limite de détection du méthanol est de 1400 ppm en phase gazeuse.

Le capteur de méthanol présente une sensibilité 3,8 fois plus faible pour l'éthanol et 30 fois plus faible pour l'acétone. La durée de conservation du capteur de méthanol est d'un mois.
**Mot clés** : Nanoparticles ; ZnS ; Adsorption ; Photocatalyse ; capteur de gaz

## Abstract:

In recent years, binary NCs have experienced exponential development thanks to their interesting properties, in particular, their photoluminescence which can not only be controlled by their size but also by their composition. As part of this thesis, we have developed a new method for the synthesis in aqueous medium of ZnS NCs by colloidal route. We first started with the synthesis of Zinc Sulfide (ZnS) nanocrystals using thioglycolic acid (TGA) as a stabilizer. These ZnS-TGA nanocrystals have been used as an inexpensive and environmentally friendly alternative for the photodegradation of methylene blue (MB) and methyl orange (MO) from aqueous solutions by solar irradiation. The photocatalytic activity of ZnS-TGA nanocrystals under solar irradiation to degrade the MB and MO dyes tested and their mixing in aqueous solutions was evaluated. High dye degradation efficiency was obtained in a very short time (27 min) and this performance was attributed to the negative surface charge, surface area, surface defects and high dispersion of ZnS- nanocrystals. TGA on the aquatic environment. Next, we report an easy and green route for novel synthesis of ZnS nanoparticles using Artemisia Herba Alba (AHA) plant extract for efficient adsorption/photodegradation of methylene blue dye. The results showed a blue shift in the absorbance band and higher energy bandgap values than the bulk ZnS materials, which was due to quantum confinement effects. These green ZnS-AHA NCs showed a surface area of 36.82 cm2 g−1 and an adsorption capacity of 31.17 mg g−1 for methylene blue. The photocatalytic degradation performance of green nanoparticles under solar irradiation showed a remarkable dye degradation rate of 94.09% in 180 min. Finally, a gas sensor based on ZnS-AHA nanocrystals is proposed for methanol vapor detection. The sensitive part of this methanol microsensor is prepared by encapsulation of ZnS nanoparticles in chitosan. A thin film of chitosan/ZnS-NPs composite was electrodeposited on the interdigitated gold electrodes by chrono-amperometric test. The ethanol, methanol and acetone gas sensing responses of the films were measured at room temperature, by differential conductometric measurements at 10 kHz. The sensor response time ($t_{Rep}$) for methanol is 11–25 s from lowest to highest concentrations. The detection limit for methanol is 1400 ppm in the gas phase. The methanol sensor has 3.8 times lower sensitivity for ethanol and 30 times lower sensitivity for acetone. The shelf life of the methanol sensor is one month.

**Keywords** : Nanoparticules ; ZnS ; Adsorption ; Photocatalysis ; Gas sensor

## Remerciements

***E**n premier lieu, je tiens à remercier Mr Christophe MORELL, directeur du Laboratoire Institut des Science Analytiques à Lyon (ISA) et Mr Mustapha MAJDOUB, directeur du Laboratoire Interfaces et Matériaux Avancés (LIMA) à Monastir de m'avoir accueilli au sein de leurs laboratoires.*

***J**e tiens particulièrement à témoigner ma profonde reconnaissance envers mes deux directeurs de thèse : Mr Abdelhamid ERRACHID et Mr Mohamed HAOUARI.*

***J**e tiens particulièrement à exprimer ma profonde gratitude à mon directeur de thèse Mr Abdelhamid ERRACHID, pour m'avoir donné l'opportunité de rejoindre son équipe et travailler sur un sujet attractif ayant donné le fruit de trois articles et qui m'a permis d'acquérir de nouvelles connaissances scientifiques et développer mes compétences. Je le remercie pour l'accueil chaleureux au sein de son équipe ainsi que pour sa grande disponibilité, ses conseils avisés et ses idées pertinentes qui m'ont aidé à résoudre les problèmes rencontrés durant ces trois années de thèse. Je remercie aussi Mr Mohamed HAOUARI, pour avoir encadré ce travail de thèse. Je vous témoigne en cette occasion ma gratitude pour votre support qui a permis le bon déroulement de cette thèse. Vos qualités humaines et vos conseils qui m'ont prodigué durant ce travail et m'ont permis de gagner en rigueur aussi bien sur le plan technique que sur le plan scientifique.*

*Mes remerciements s'adressent aussi à mes co-encadreurs, Madame Nicole JAFFREZIC-RENAULT Directrice de recherche émérite CNRS en France et Monsieur Naim BEL HAJ MOHAMED, Maître assistant à l'Institut supérieur des sciences appliquées et de la technologie de Kairouan (ISSATK) en Tunisie. Merci pour la grande bienveillance à mon égard. Je tiens à vous exprimer ici ma gratitude et mon profond respect. Vos qualités humaines et vos conseils qui m'ont prodigué durant ce travail et m'ont permis de gagner en rigueur aussi bien sur le plan technique que sur le plan scientifique. Je vous remercie énormément pour vos conseils scientifiques tout au long du travail, votre grande disponibilité, vos encouragements et vos qualités humaines. J'ai beaucoup appris à votre côté et je suis très reconnaissant pour tout cela.*

*Je tiens à remercier chaleureusement Madame BORDES Claire, Professeur à Université Lyon 1 en France, m'a fait un grand honneur de présider le jury de ce travail. Qu'il veuille bien trouver ici toute ma gratitude et mes sentiments de respect.*

*Un très grand merci à Monsieur Wissem DIMASSI Professeur au Centre de Recherches et des Technologies de l'Energie CRTEn en Tunisie et Madame Hafsa KORRI-YOUSSOUFI Directrice de recherche CNRS en France qui ont accepté de rapporter et d'évaluer ma thèse.*

*J'adresse également mes sincères remerciements à Madame DEBEDA Hélène Maître de Conférences à Université de Bordeaux en France et Monsieur Hassen FREDJ Professeur à l'Université de Monastir en Tunisie qui m'ont fait l'honneur de bien vouloir examiner mon travail.*

*Je ne saurais terminer sans remercier vivement Madame Rym MLIKA Professeure à l'Université de Monastir en Tunisie, pour son encouragement, son soutien et son aide. Cette personne exceptionnelle a cru en moi et a énormément contribué pour que je finisse dans de bonnes conditions ces travaux.*

*Je ne peux bien évidemment pas oublier tous les membres de notre équipe pour les beaux moments qu'on a passés ensemble, leur support moral et leur compagnie. Je me sens très chanceux de vous avoir tous rencontré. Vous allez me faire garder de beaux souvenirs.*

*Enfin, je ne serai pas là non plus sans le soutien constant de ma famille et de mes amis. Merci donc à mes parents, je ne saurai trouver les mots qui conviennent pour vous remercier, c'est grâce à vous que j'avance.*

*Région Auvergne Rhône-Alpes est remerciée pour son soutien financier à travers le projet Pack Ambition International, EMBAI #246413.*

*CNRS est remercié pour son soutien dans le cadre de l'IRP NARES.*

*Campus France est remercié pour son soutien financier à travers le PHC Maghreb EMBISALIM.*

*Je remercie l'Université de Monastir pour la bourse d'alternance.*

# *Sommaire*

# Liste des abréviations

| | |
|---|---|
| θ | Angle de diffraction de Bragg |
| EMA | Approximation de la masse effective |
| AHA | Artemisia Herba Alba |
| BC | Bande de conduction |
| BV | Bande de valence |
| ε | Constante diélectrique |
| D | Diamètre |
| LED | Diode électroluminescentes |
| e- | Electron |
| Eg | Energie de gap |
| k | Facteur de forme |
| FT-IR | Fourier-Transform Infrared Spectroscopy |
| HR-TEM | High-Resolution Transmission Electron Microscopy |
| Izn | Interstitiel de Zinc |
| K | Kelvin |
| Vs | Lacune de Soufre |
| $V_{Zn}$ | Lacune de zinc |
| β | Largeur à mi-hauteur |
| L-Cys | L-Cysteine |
| MO | Méthylène orange |
| MB | Méthylène bleu |
| NA | Nano-adsorbant |
| NC | Nanocristal |
| NP | Nanoparticule |
| PL | Photoluminescence |
| QDs | Quantum Dots |
| QY | Quantum yield |
| $r_B$ | Rayon de Bohr (2.5 nm pour le ZnS) |
| RQ | Rendement quantique |

| | |
|---|---|
| S | Souffre |
| CdS | Sulfure de Cadmium |
| ZnS | Sulfure de Zinc |
| TEM | Transmission Electron Microscopy |
| TGA | Thioglycolic acid |
| $h^+$ | Trou |
| Zn | Zinc |
| ZB | Zinc Blende |
| UV | Ultraviolet |
| XRD | X-ray diffraction |

# *Introduction générale*

Le développement des nanotechnologies est l'un des axes de recherche privilégiés ces dernières décennies. Diverses applications dans une multitude de secteurs sont des témoins allant de l'ordinateur quantique à l'imagerie médicale en passant par les écrans, l'éclairage, les capteurs, les biocapteurs, les lasers, les batteries, la conversion photovoltaïque et la photocatalyse pour la dégradation des polluants persistants. Ceci est initié par l'élaboration de nouveaux nanomatériaux qui sont à la fois intéressants de point de vue fondamentale ainsi que technologique. En particulier, les nanocristaux des semi-conducteurs II-VI (également appelés « points quantiques ») en sont de parfaits exemples. Ce sont des nanoparticules colloïdales formées de quelques centaines à quelques milliers d'atomes seulement qui émettent de la fluorescence après leur excitation par une source de lumière UV ou visible. Certaines de leurs propriétés optiques et électroniques (spectres d'émission fins et accordables par la taille, bons rendements quantiques de photoluminescence) sont exceptionnelles et sont directement corrélées à leur taille et/ou à leur composition. En effet, leur taille réduite induit le confinement spatial des porteurs de charges conduisant à la discrétisation des niveaux d'énergies ainsi qu'à l'élargissement de la bande interdite du matériau. C'est l'effet du confinement quantique. Ainsi, en changeant la nature ou le rayon de nanoparticule semi-conductrice, il est possible de balayer une bonne partie du spectre électromagnétique. Par exemple, les nanocristaux de séléniure de cadmium (CdSe) peuvent émettre dans l'ensemble du spectre visible (de 450 à 700 nm environ) lorsque leur taille varie de 2 nm à 10 nm. Ces nanocristaux sont stabilisés par une couche de ligands organiques adsorbés à la surface, ce qui permet d'assurer la stabilité colloïdale et la passivation de défauts de surface. Cette couche organique améliore de façon spectaculaire le rendement quantique de fluorescence des cœurs inorganiques. Malgré l'augmentation significative de l'intensité de luminescence des nanocristaux de semi-conducteurs, cette intensité reste encore trop faible pour répondre aux besoins technologiques et énergétiques mondiaux. Il a alors fallu développer des voies alternatives afin d'obtenir d'intenses émissions de photons à partir de ce matériau. Par exemple, les nanocristaux de séléniure de cadmium (CdSe) peuvent émettre sur tout le spectre visible (environ 450 à 700 nm) lorsque leur taille varie de 2 à 10 nm. Ces nanocristaux sont stabilisés par une couche de ligands thiols organiques tels que l'acide mercaptopropionique (MPA) et le glutathion (GSH), qui sont adsorbés à leur surface pour assurer la stabilité colloïdale et la passivation des défauts de surface. De plus, ils sont généralement stabilisés par de l'alcool polyvinylique (PVA) et du chitosane. D'autres revêtements peuvent être utilisés tels que les matrices en silice. Par conséquent, cette couche organique peut améliorer considérablement l'efficacité de fluorescence quantique du noyau inorganique. Cependant, il est important de synthétiser des nanocristaux à très faible toxicité

tels que ZnO, ZnSe, TiO2 et ZnS , qui doivent avoir toutes les caractéristiques requises pour leur intégration dans diverses applications et notamment dans les activités photocatalytiques. Les méthodes traditionnelles de fabrication des nanoparticules (NPs), en revanche, impliquent souvent l'utilisation de produits chimiques et de solvants toxiques, qui peuvent être nocifs pour l'environnement. Par conséquent, il existe un intérêt croissant pour le développement de méthodes respectueuses de l'environnement pour la biosynthèse des nanoparticules. Une de ces approches est l'utilisation d'agents biologiques, tels que des micro-organismes, des plantes et des enzymes, pour la synthèse des nanoparticules. Ces agents peuvent réduire les ions métalliques et générer des NPs par un processus connu sous le nom de bio-réduction. Par exemple, les nanoparticules peuvent être synthétisées à partir de substances biologiques telles que des plantes, des algues, des bactéries et des champignons, ce qui est défini comme une alternative nouvelle, simple, rapide, économique et écologique. Actuellement, il existe un intérêt croissant pour la méthode de chimie verte pour la synthèse du sulfure de zinc. Les extraits de plantes présentent plusieurs avantages, tels qu'une manipulation sûre et la non-toxicité. En outre, ils peuvent agir à la fois comme agents réducteurs et stabilisants pour les nanoparticules.

Les problèmes de pollution de l'environnement sont pertinents dans le monde entier et nécessitent le développement de procédés de traitement efficaces pour éliminer/dégrader les polluants avec de meilleures performances que les technologies actuelles, en particulier pour celles appliquées au traitement de l'eau. L'une des principales sources de pollution de l'eau est l'élimination inappropriée des colorants utilisés dans les fibres textiles, la coloration des métaux et la peinture. Ces produits chimiques sont miscibles dans l'eau même à de faibles concentrations et ils contribuent aux problèmes de pollution liés à la génération d'une quantité considérable d'eaux usées contenant des molécules de colorants résiduels. Ces colorants peuvent être toxiques et cancérigènes et, par conséquent, il est nécessaire de trouver des techniques pour dégrader/éliminer ces polluants dangereux. L'une de ces nouvelles méthodes repose sur le processus écologique d'oxydation avancée (PAO) qui fait intervenir de puissantes espèces oxydantes pour parvenir à la minéralisation complète des polluants organiques en $CO_2$ et $H_2O$ ou au moins à leur transformation en intermédiaires biodégradables. La photocatalyse est le processus d'irradiation d'un matériau semi-conducteur soit naturellement, soit par un flux de photons. Un électron est ainsi photo-libéré en effectuant une transition d'énergie de la bande de valence (BV) vers la bande de conduction (BC). Cette transition génère un couple ($e^-$ /$h^+$) dans le matériau. Les paires électron-trou diffusent vers la surface du catalyseur où l'interaction

avec les molécules d'eau générerait des espèces hautement oxydantes de peroxyde ($O_2^{*-}$) et de radical hydroxyle ($OH^*$), responsables de la dégradation des molécules organiques adsorbées à la surface du photocatalyseur. Cette méthode de traitement est efficace et verte pour résoudre la pollution causée par une variété de polluants de l'eau, y compris les molécules de colorant. Les molécules de colorant sont hautement solubles dans l'eau avec une faible pression de vapeur et, par conséquent, elles peuvent être utilisées comme composés modèles pour tester et évaluer les performances de nouveaux photocatalyseurs. Parmi les nanoparticules couramment utilisées pour dégrader ces molécules toxiques, les nanocristaux de sulfure de zinc (ZnS) sont une alternative intéressante en raison de leur grande stabilité, de leur non-toxicité et de leur abondance dans la nature.

Ainsi, le développement d'un capteur d'alcool présentant une sensibilité élevée ainsi qu'une sélectivité optimisée, pouvant fonctionner à température ambiante doit être bien adapté à cette demande. Afin de faciliter la détection en ligne et la mesure portable, l'objectif principal du développement des capteurs d'alcool est la détection de l'alcool en phase gazeuse. L'alcool de méthanol est un solvant organique très utile avec des applications répandues dans les carburants automobiles et la fabrication de couleurs, de colorants, de médicaments, de parfums, de formaldéhyde, etc. Cependant, il est hautement toxique et souvent mortel pour les êtres humains. Le large éventail d'applications, la toxicité et les implications cliniques du méthanol rendent impératif le développement d'un capteur de méthanol fiable et sélectif. L'objectif principal est donc de détecter le méthanol en présence d'autres alcools. La principale forme de transduction étudiée dans les approches de détection est ici décrite : onde acoustique, résistance ou changements capacitifs. Le capteur de gaz conductimétrique est le plus largement utilisé parmi les dispositifs connus et utilisés pour contrôler les gaz dangereux et inflammables dans le diagnostic médical, les processus industriels et les études environnementales. Les capteurs conductimétriques présentent une conception simple qui se compose de seulement deux composants : une couche conductrice sensible et des électrodes de contact.

Dans le cadre de cette thèse, nous avons développé une nouvelle méthode de synthèse des nanocristaux de ZnS. L'impact de la surface sur les propriétés optiques et structurales des NCs a été étudié à travers l'utilisation de deux types de ligands organiques et biologiques. Par la suite, la performance de ces NCs synthétisés a été évaluée par l'utilisation dans deux applications environnementales : la photocatalyse des polluants organiques et les capteurs de gaz.

La thèse est composée de quatre chapitres :

***Le Chapitre I*** est une étude bibliographique qui comprend une description de la structure des NCs, leurs méthodes de synthèse, leurs propriétés ainsi que leur application. Nous nous intéresserons plus particulièrement aux NCs de ZnS en présentant leurs propriétés, leurs méthodes de synthèse ainsi que leurs applications pour mettre en évidence l'avantage de ce type de NCs par rapport aux autres nanocristaux.

***Le Chapitre II*** représente les résultats de l'article « *High impact of thiol capped ZnS nanocrystals on the degradation of single and binary aqueous solutions of industrial azo dyes under sunlight* », *publié dans le journal of Environmental Chemical Engineering en 2021 :* S. Ouni, N. Mohamed, M. Bouzidi, A. Bonilla-Petriciolet, M. Haouari J. Environ. Chem. Eng. 9 (2021) 105915. *https://doi.org/10.1016/j.jece.2021.105915*. Ce chapitre est consacré à la synthèse en milieu aqueux des NCs de ZnS en utilisant un ligand organique de TGA, à l'étude de leurs propriétés optiques et structurale.
Ces NCs synthétisés ont été utilisé pour la dégradation de solutions aqueuses simples et binaires de colorants azoïques industriels sous la lumière du soleil.
***Le Chapitre III*** représente les résultats de l'article « *A Novel Green Synthesis of Zinc Sulfide Nano-Adsorbents Using Artemisia Herba Alba Plant Extract for Adsorption and Photocatalysis of Methylene Blue Dye* », *publié dans le journal Chemistry Africa en 2023 : S. Ouni, N. B. H. Mohamed, M. Haouari, A. Elaissari, A. Errachid, and N. Jaffrezic-Renault Chemistry Africa (2023), https://doi.org/10.1007/s42250-023-00667-7.* Ce chapitre est consacré à la synthèse en milieu aqueux des NCs de ZnS par la chimie verte en utilisant l'extrait de l'Artemisia Herba Alba et à l'étude de leurs propriétés optiques et structurale.

Ces NCs synthétisés ont été utilisé pour l'adsorption et dégradation de solutions du bleu de methylene.

***Le Chapitre IV*** représente les résultats de l'article « *A novel conductometric micro-sensor for methanol detection based on chitosan/zinc sulfide-nanoparticles composite obtained by green synthesis*», *publié dans le journal of Inorganic and Organometallic Polymers and Materials en 2023 : S. Ouni, A. Madaci, M. Haouari, N. B. H. Mohamed, F. Bessueille, A. Elaissari, A. Errachid, and N.Jaffrezic-Renault, J Inorg Organomet Polym (2023), https://doi.org/10.1007/s10904-023-02696-8.*

Ce chapitre est consacré à l'élaboration d'un micro-capteur conductimétrique pour la détection du méthanol basé sur un composite chitosane/sulfure de zinc-nanoparticules obtenu par synthèse verte.

Une partie annexe présente les différentes techniques de caractérisation utilisée dans le cadre de cette thèse.

Le manuscrit se termine par une conclusion générale qui présente les principaux résultats obtenus et les perspectives de recherche sur les travaux réalisés.

# *Chapitre I*

## *Etude bibliographique sur les nanoparticules semiconducteurs II-IV*

# Introduction

Dans ce premier chapitre, nous commencerons par donner un aperçu général sur les différentes propriétés des semiconducteurs massifs II-VI. Ensuite, nous nous focaliserons sur un bref état de connaissances actuelles sur les nanocristaux (NCs) semi-conducteurs de type II-VI, en particulier leurs propriétés électroniques, optiques et structurales venants de leurs dimensions nanométriques. Enfin, Nous exposerons les différentes voies de synthèse des nanocristaux semi-conducteurs II-VI et leurs applications les plus développées jusqu'à présent.

# I. Généralités sur les semiconducteurs massifs II-IV

## I.1 Définition

Un semi-conducteur est un matériau qui a la capacité de conduire l'électricité à un niveau intermédiaire entre un conducteur (comme les métaux) et un isolant (comme le verre). Il possède une conductivité électrique intermédiaire entre celle des isolants ($10^{-22}$ à $10^{-14}$ $\Omega^{-1}.cm^{-1}$) et celle des métaux ($10^{-6}$ $\Omega^{-1}$ $.cm^{-1}$) [1]. Cette conductivité varie sous l'effet de la température, excitation lumineuse et la présence d'impuretés (dopage, défauts du réseau). Les semi-conducteurs sont principalement les éléments de la colonne IV du tableau de la classification des éléments (Si, Ge) mais aussi des composés III-V (GaAs, InP) et II-VI (ZnS, CdSe, CdTe) [2]. Il existe plusieurs types de matériaux semi-conducteurs dont quelques exemples et leurs propriétés sont présentées dans le ***Tableau I.1***. Ce qui nous intéresse dans ce travail, ce sont les semi-conducteurs de la famille II-VI, en particulier le ZnS. Ce dernier est l'association d'un élément de la colonne II (Zn) avec un élément de la colonne VI (S) de la classification périodique de Mendeleïev. Donc ces composés ne possèdent que deux électrons de valence de l'élément Zn sur leur dernière orbitale (s) et quatre électrons sur les orbitales s et p de l'élément S. Dans le cadre de la théorie des bandes, les semi-conducteurs II-VI massifs sont caractérisés par deux bandes d'énergie : une bande de conduction (BC) qui est la bande permise de la plus haute énergie qui peut être partiellement remplie d'électrons ou bien vide et la bande de valence (BV) de plus basse énergie remplie d'électrons [3]. L'écart entre ces dernières est appelé bande interdite ou gap. Cette bande est faible relativement aux matériaux isolants (1-4 eV). La ***Figure I.1*** montre les niveaux d'énergie relatifs à ces deux bandes.

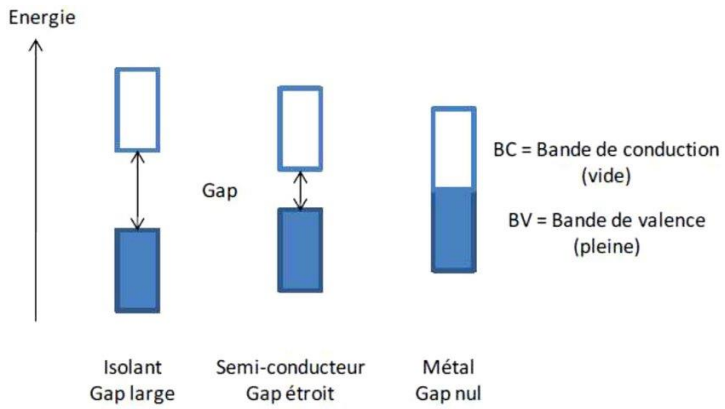


***Figure I.1*** **:** Diagramme énergétique schématique des matériaux conducteurs, semi-conducteurs et isolants.

***Tableau I.1*** : Exemple de matériaux semi-conducteurs et quelques paramètres associés [4]

| **Semi-conducteur** | **Type** | **Energie de bande interdite du massif à 300 K (eV)** | **Structure cristal-line** | **Rayon de Bohr (nm)** |
|---|---|---|---|---|
| **Oxyde de Zinc (ZnO)** | II.VI | 3.30 | Wurtzite | 2.4 |
| **Seleniure de Cadmium (CdSe)** | II.VI | 1.76 | Wurtzite | 5.30 |
| **Sulfure de Cadmium (CdS)** | II.VI | 2.52 | Wurtzite | 3.00 |
| **Sulfure de Zinc (ZnS)** | II.VI | 3.60 | Zinc blende | 2.50 |
| **Seleniure de Zinc (ZnSe)** | II.VI | 2.70 | Zinc blende | 4.50 |
| **Arseniure de Galium (GaAs)** | III.V | 1.42 | Zinc blende | 12.2 |
| **Arseniure d'Indium (InAs)** | III.V | 0.35 | Zinc blende | 31.2 |
| **Phosphorure d'Indium (InP)** | III.V | 1.34 | Zinc blende | 9.9 |

## I.2 Structure cristalline

A température ambiante, les semi-conducteurs II-VI, en particulier le ZnS, existent sous deux structures cristallines distinctes [5] :

- Structure Zinc blende (sphalérite) : dans laquelle les deux sous réseaux du Zn et du S sont

cubiques à faces centrées l'un par rapport à l'autre de ¼ du paramètre de maille. Elle possède donc un empilement cubique à faces centrées (cfc).

- Structure Wurtzite (hexagonale) : dans cette structure les sous réseaux dans le cristal sont hexagonaux compacts.

Ces deux structures sont très similaires de point de vue structural mais l'alternance des plans est différente :la structure Zinc-blende est constituée d'une alternance de type ABCABCABC… et la structure Wurtzite est caractérisée par une alternance de plans de type ABABAB…En conséquence, la différence énergétique entre les deux structures est faible et il est courant que ces deux structures coexistent au sein du même matériau [6]. Dans le cas du sulfure de zinc (ZnS), la structure Zinc-blende est la phase qui est thermodynamiquement stable à basse température, alors que la structure Wurtzite est la plus stable à température élevée. La ***Figure I.2*** représente ces deux types de structures cristallines.

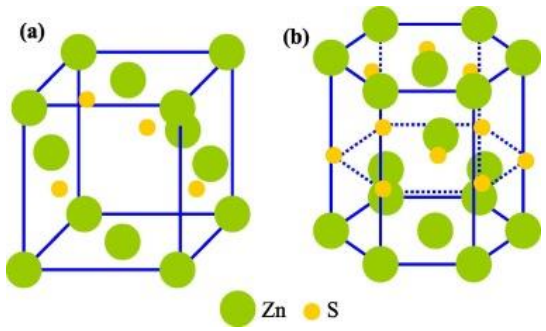


***Figure I.2*****:** Structure cristalline de ZnS : (a) Zinc-blende et (b) Wurtzite

Les paramètres de maille sont :

- **a = 5.41Å** pour la structure zinc blende
- **a = 3.82 Å et c = 6.62 Å** pour la structure Wurtzite.

## I.3 Propriétés optiques

Le ZnS est un semi-conducteur à gap direct, c'est à dire le sommet de la BV et le minimum de la BC correspondent au même vecteur d'onde. L'excitation optique d'une manière résonante ($h\nu_{exc}$ = Eg) ou non résonante ($h\nu_{exc} \geq$ Eg) donne naissance à une paire électron-trou suite à l'excitation d'un électron de la BV vers la BC. L'électron et le trou sont liés par attraction Coulombienne et forment un état lié appelé exciton (***Figure I.3***), leur distance moyenne est appelée rayon de Bohr de l'exciton par analogie avec le rayon de Bohr de l'atome d'hydrogène. Dans le cas du ZnS, le rayon de Bohr de l'exciton est de l'ordre de 2.5 nm [7]. L'électron et le trou relaxent vers des niveaux d'énergie plus bas par émission de phonons vers le réseau et leur

recombinaison peut se faire d'une façon radiative par émission de photon : c'est le phénomène de la photoluminescence. Dans le ***Tableau I.2*** on présente quelques propriétés physiques de ZnS à 300K

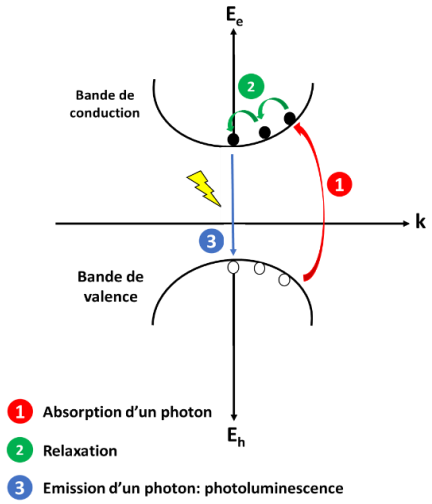


***Figure I.3*** **:** Mécanisme d'émission dans un semi-conducteur massif

***Tableau I.2*** **:** Propriétés physiques de ZnS à 300K [8].

| Propriétés | Structure de ZnS | |
|---|---|---|
| | Zinc-blende | Wurtzite |
| Paramètres de maille (Å) | a=0,541 | a = 3,82 et c = 6,26 |
| Point de fusion (°C) | 1185 | |
| Constante diélectrique statique ε (F/m) | 8,9 | |
| Constante diélectrique ε (F/m) | $8{,}854 \times 10^{-12}$ | |
| Masse d'électron libre (kg) | $m_0 = 9{,}109 \times 10^{-31}$ | |
| Masse effective de l'électron | $m_e^* = 0{,}28 m_0$ | |
| Masse effective du trou | $m_h^* = 0{,}61 m_0$ | |
| Rayon de Bohr (nm) | $a_B =$ 2,5 | |
| Energie de gap (eV) | Eg =3,6 | |

## II. Généralités sur les semi-conducteurs nanocristaux

Les nanocristaux (NCs) semiconducteurs, souvent appelés points quantiques (quantum dots, QDs), sont des petites particules cristallines ayant typiquement un diamètre compris entre 1 et

10 nm. Ils sont généralement constitués d'un cœur cristallin composé d'un métal (Zn, Cd, Cu, …) associé à un chalcogénure (Se, S, Te, …), recouvert d'une couche de molécules qu'on appelle ligand (***Figure I.4***). Cette couche est indispensable pour assurer la stabilité des NCs sous forme des particules colloïdales et éviter leur agrégation ainsi que pour définir leur polarité. Le cœur contient une quantité dénombrable d'atomes, typiquement quelques centaines à plusieurs dizaines de milliers, avec une importante fraction d'atomes à la surface et qui augmente avec la diminution de la taille des NCs [9].

L'augmentation de la proportion des atomes à la surface des NCs, suite à la réduction de leur taille, peut donner naissance à des imperfections de surface tels que des états pièges dus aux liaisons pendantes. Ces dernières génèrent des recombinaisons non-radiatives des paires électrons-trou qui affectent les propriétés optiques des NCs, notamment leur rendement quantique (RQ) de fluorescence. Afin de contourner ces obstacles, il faudra réaliser une bonne passivation de la surface des NCs. Ceci est possible soit par un échange de ligands [10] ou par la croissance d'une ou plusieurs coquilles inorganiques [11,12].

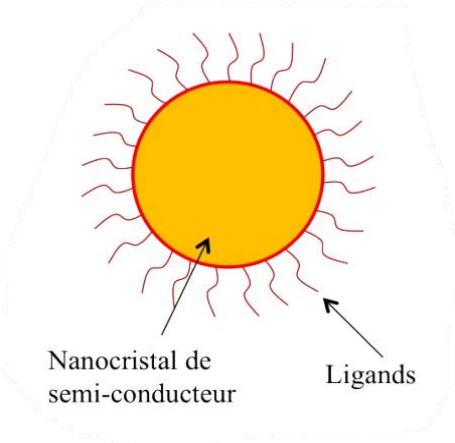


***Figure I.4*****:** Représentation schématique d'un NC recouvert d'une couche de ligand

## II.1 Nanocristaux colloïdaux : Forme et taille

Les nanocristaux colloïdaux, également connus sous le nom de nanocristaux semi-conducteurs (NCs) ou de points quantiques, sont des particules cristallines de taille nanométrique (typiquement de l'ordre de quelques nanomètres à quelques dizaines de nanomètres) dispersées dans un milieu colloïdal, généralement une solution liquide.

Historiquement, les premiers NCs synthétisés en 1993 par Murray et al étaient sphériques [13]. Cette morphologie est la plus thermodynamiquement favorisée puisqu'elle minimise le rapport

surface/volume des NCs. Afin d'induire une anisotropie morphologique, il est important de favoriser une croissance cinétique en jouant sur les ligands et la quantité de monomères en solution. En effet les ligands vont avoir des affinités accrues pour certaines facettes du NC. Ainsi, en contrôlant la nature des ligands, il est possible d'orienter la croissance dans une direction ou une autre [14].

En termes de forme, les nanocristaux colloïdaux peuvent présenter une variété de morphologies **(*Figure I.5*)**, notamment des sphères, des batônnets, des branchées, etc. La forme spécifique dépend des conditions de synthèse et des interactions entre les atomes ou les molécules constituant les nanocristaux.

En résumé, les nanocristaux colloïdaux peuvent adopter différentes formes et tailles en fonction des conditions de synthèse. Leur forme et leur taille influencent leurs propriétés physiques et chimiques, ce qui en fait des matériaux intéressants pour une large gamme d'applications, notamment en optoélectronique, en biotechnologie, en catalyse et en nanomédecine [15–18].

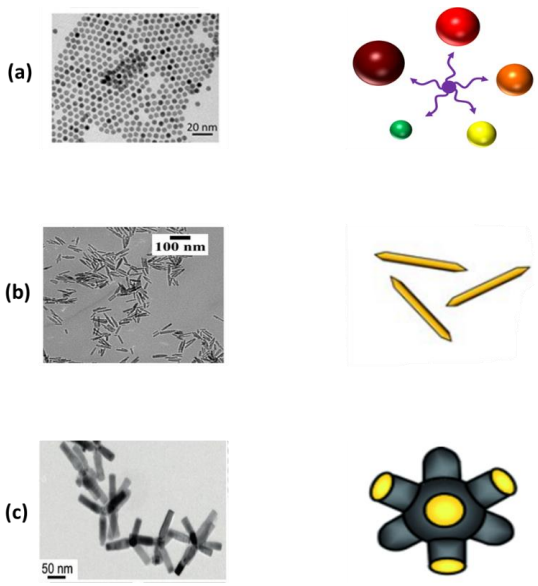


***Figure I.5***. Différentes formes des nanocristaux : (a) sphériques, (b) batônnets, et (c) branchées

### II.1.1 Qu'est-ce qu'un nanocristal colloïdal

Un nanocristal colloïdal est un cristal semi-conducteur de taille nanométrique synthétisé par voie chimique, celle-ci pouvant être solide (verre, polymère) ou liquide. Ils furent découverts dans les années 80 par Alexei Ekimov, [19] et la première synthèse colloïdale organométallique

fut publiée par l'équipe de Bawendi au MIT en 1993. Il s'agit d'assemblages de quelques dizaines à quelques milliers d'atomes arrangés en monocristaux ou poly-cristaux. Les atomes situés au cœur de la nanoparticule auront des environnements électroniques différents de ceux situés à sa surface. Les conséquences de ce phénomène sont nombreuses et nous pouvons notamment citer la modification du paramètre de maille du NC en comparaison avec le matériau massif.

Afin d'assurer la stabilité colloïdale en solution et d'éviter l'agrégation des nanoparticules, les nanocristaux sont enrobés par des ligands organiques. Ces ligands sont implantés sur la surface des nanocristaux. Ils contiennent une tête polaire et une queue apolaire, qui peut être une ou plusieurs chaines alkyles (***Figure I.6***). Un bon contrôle de la croissance des nanocristaux est assuré par l'échange des ligands à la surface des particules [20].

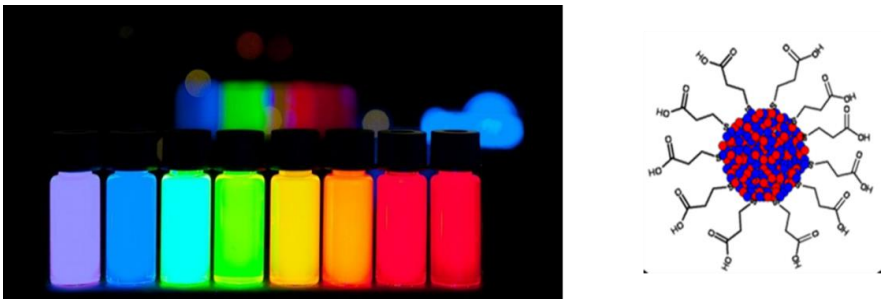

***Figure I.6*** **:** (a) Suspensions colloïdales de nanocristaux de CdSe de différentes tailles illuminées par une lampe à ultraviolets (b) schéma d'un nanocristal colloïdal de CdSe entouré de ses ligands assurant la stabilité colloïdale

### II.1.2 Synthèse par voie colloïdale

L'objectif de synthèse des nanocristaux par voie colloïdale est d'obtenir des dispersions composées d'objets absolument similaires (***Figure I.7***). Il est alors essentiel de contrôler les tailles de ces nano-objets afin d'obtenir une population monodisperse. Parmi ces méthodes de synthèse par voie colloïdale on distingue deux principaux types : la synthèse en milieu aqueux et la synthèse en milieu non-aqueux. Notre étude est basée sur la synthèse en milieu aqueux. Ce procédé de synthèse, mis au point pour la fabrication des nanocristaux de ZnE (E étant un chalcogènure: soufre S, Sélénium Se ou tellure Te), a été développée pour inclure d'autres semi-conducteurs tels que les groupes II-VI (CdSe, CdS, HgTe ...) et III-V (InP, InAs…). Afin d'assurer la stabilité colloïdale en solution et d'éviter l'agrégation, les NCs sont entourés de ligands. Ces ligands sont situés à la surface des NCs et possèdent une tête avec une bonne affinité pour la surface des NCs et une queue avec une bonne affinité pour le solvant.

***Figure I.7*** **:** Synthèse de nanocristaux en solution par voie colloïdale

### II.1.3 Synthèse en milieu aqueux et organique

La synthèse des nanocristaux semi-conducteurs, également appelés points quantiques, est généralement réalisée par des méthodes chimiques colloïdales. Il existe plusieurs approches pour synthétiser ces nanocristaux.

- La synthèse en phase solide (par voie physique) qui peut être réalisée soit par des techniques lithographiques [21,22], soit par des techniques épitaxiales [23,24].

- La synthèse en phase liquide (par voie chimique), on l'appelle aussi synthèse colloïdale. Cette méthode, sur laquelle se focalisera notre travail, fait appel à des techniques de la chimie de colloïdes. Elle a attiré une grande attention grâce aux résultats remarquables concernant l'obtention de QDs de forme et de taille contrôlées [25]. Cette méthode peut être développée en milieu aqueux en présence d'un stabilisant et à des températures relativement basses (généralement 100-150°C) [26,27] ou en milieu organique (synthèse organométallique, décomposition thermique) à des températures généralement supérieures à 200°C [28,29]. Quel que soit le solvant, le principe est basé sur la séparation temporelle des étapes de la nucléation et de la croissance.

  - **<u>Synthèse en milieu organique</u>**

La synthèse en milieu organique (non aqueux) est utilisée lorsque les matériaux semi-conducteurs ne sont pas solubles dans l'eau ou lorsque l'eau peut interférer avec la réaction chimique souhaitée. Les solvants non aqueux couramment utilisés dans ce contexte comprennent les solvants organiques tels que l'oxyde de tri-n-octylphosphine (TOPO) [30], ,

l'hexane [31], le toluène [32]et l'acétone [33] qui jouent le rôle de ligands et qui sont hydrophobes. La synthèse en milieu non aqueux peut impliquer des techniques telles que la microémulsion inverse ou la synthèse en phase vapeur, où les réactifs sont dissous dans un solvant non aqueux et la réaction chimique a lieu dans ce milieu. Les solvants non aqueux offrent souvent des conditions réactionnelles différentes, permettant un contrôle plus précis de la taille, de la forme et de la composition des nanocristaux.

- **Synthèse en milieu aqueux**

La synthèse en milieu aqueux est couramment utilisée pour la préparation de nanocristaux semi-conducteurs tels que les sulfures de cadmium (CdS) et les séléniures de cadmium (CdSe) [34,35]. Dans cette méthode, les réactifs et les précurseurs sont dissous dans un solvant aqueux, généralement de l'eau, pour former une solution réactionnelle. La réaction chimique a lieu dans cette solution aqueuse à des températures élevées, généralement avec l'aide de ligands ou de stabilisants pour contrôler la taille et la croissance des nanocristaux. Les ligands peuvent également jouer un rôle dans la stabilisation des nanocristaux et la prévention de leur agrégation.

La synthèse en milieu aqueux possède plusieurs avantages ; elle est spécifiée par sa simplicité, son importante reproductibilité et sa faisabilité dans la production de grandes quantités des nanoparticules.

### II.1.4 Les étapes de nucléation et de croissance

Généralement, la synthèse des NCs en milieu aqueux se déroule en deux étapes bien distinctes (théorie de V.K. LaMer [36]) : une phase de nucléation qui est très courte suivie d'une phase de croissance qui est plus lente (***Figure I.8***).

**1) La nucléation** : La nucléation est la première étape de formation d'un nouveau matériau à partir d'une solution, d'un gaz ou d'un état désordonné. Elle se produit lorsque des agrégats de taille critique, appelés noyaux, se forment à partir des espèces moléculaires ou atomiques présentes dans le système. La nucléation peut être spontanée ou induite par des agents de nucléation tels que des catalyseurs, des surfaces spécifiques ou des chocs mécaniques.

**2) La croissance** : Une fois que les noyaux sont formés, ils peuvent croître en taille et en nombre en incorporant des molécules ou des atomes supplémentaires provenant de la solution ou de l'environnement. La croissance peut se produire par diffusion des espèces chimiques vers les sites actifs sur la surface des noyaux, ou par agglomération des noyaux existants.

Lors de la synthèse des NCs, un troisième phénomène thermodynamique appelé murissement d'Ostwald peut avoir lieu quand il n'y a plus de précurseurs permettant la croissance homogène des nanoparticules [37]. Il s'agit d'une interdiffusion des particules les plus petites ayant une énergie de surface élevée vers les plus grosses. Par conséquent, une dégradation de la dispersion en taille des nanoparticules est observée. Afin d'obtenir des nanoparticules monodisperses, il est donc nécessaire d'arrêter la synthèse avant que le murissement d'Ostwald ne se produise.

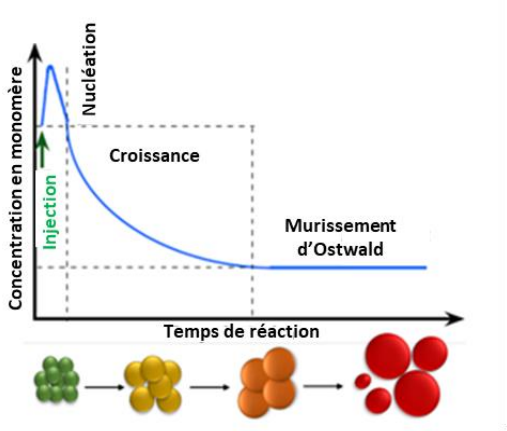


***Figure I.8*** : Croissance des nanoparticules

### II.1.5 Le rôle des ligands dans la synthèse colloïdale

Lorsqu'on réduit la dimension d'un semi-conducteur massif, sa surface peut présenter des imperfections en raison de la présence d'atomes sous-coordonnés à la surface, ce qui peut grandement affecter les performances optiques des nanocristaux. Les effets de surface sont commandés par le rapport entre les atomes situés en surface et dans le volume. Par exemple, la température de fusion est inversement proportionnelle au rayon et donc proportionnelle au rapport surface/volume. Ceci est dû à la diminution du nombre de coordination à la surface, ce qui réduit l'énergie moyenne de liaison et par conséquent la température de fusion ($T_f$). Ces défauts induisent la présence de nouveaux niveaux d'énergie dans le diagramme énergétique. Ces niveaux peuvent être compris entre la bande de valence et la bande de conduction. Ils piègent les porteurs de charges donnant lieu à des recombinaisons radiatives et non radiatives. Ces recombinaisons vont diminuer le rendement quantique (RQ), qui correspond au rapport du nombre de photons émis sur celui des photons absorbés. La plupart des NCs de semi-conducteurs « nus » présentent un RQ inférieur à 10 % à cause d'un grand nombre de défauts présents à leur surface [38]. Pour assurer la passivation de ces liaisons pendantes à la surface, on doit alors utiliser des ligands organiques ou des coquilles inorganiques pour obtenir des nanocristaux fluorescents. En effet, les ligands peuvent parfois diminuer le nombre de défauts (sous-coordination) et assurer une passivation de la surface [39].

## II.2 De l’organique vers la chimie verte

La transition de la chimie organique vers la chimie verte est un domaine d'évolution important dans le domaine de la chimie. La chimie verte vise à concevoir et à développer des processus chimiques qui sont plus durables, respectueux de l'environnement et économiquement viables.

La chimie verte encourage l'utilisation de substances chimiques moins toxiques ou non toxiques, en remplaçant, par exemple, des solvants organiques dangereux par des solvants aqueux ou d'autres solvants verts [40]. Cela réduit les risques pour la santé des travailleurs, diminue l'impact environnemental et favorise une production plus sûre. Cette alternative favorise la minimisation des déchets chimiques en favorisant les réactions sélectives, la régénération des catalyseurs, le recyclage des solvants et l'utilisation de méthodes de purification efficaces [41]. Cela conduit à une production plus propre et à une réduction de la pollution. La chimie verte vise à aligner les progrès de la chimie avec la préservation de l'environnement et la durabilité à long terme. En adoptant des principes et des pratiques de la chimie verte, il est possible de réduire l'impact négatif de la chimie sur la planète, tout en développant des produits et des processus chimiques qui répondent aux besoins actuels et futurs de la société.

### II.2.1 Synthèse Verte des nanoparticules

La chimie verte des nanoparticules se réfère à l'utilisation de principes de la chimie verte dans la synthèse, la manipulation et l'application de nanoparticules. La chimie verte, également appelée chimie durable, est un concept qui vise à minimiser l'impact environnemental des processus chimiques en favorisant des méthodes plus durables, économes en énergie et respectueuses de l'environnement.

La fonctionnalisation de surface dans la chimie verte vise à modifier les nanoparticules en ajoutant des groupes fonctionnels respectueux de l'environnement à leur surface [40]. Cela permet de les rendre plus stables, réactives ou compatibles avec d'autres matériaux, tout en minimisant l'utilisation de produits chimiques nocifs. A titre d’exemple les ligands biodégradables qui sont utilisés pour fonctionnaliser la surface des nanoparticules peuvent être choisis parmi des matériaux biodégradables ou issus de sources renouvelables. Par exemple, des polymères naturels tels que la cellulose, la chitosane ou l'acide polyglutamique peuvent être

utilisés comme revêtements de surface respectueux de l'environnement [42–44]. Ces ligands se dégradent facilement et minimisent l'impact environnemental. Les nanoparticules peuvent être fonctionnalisées avec des molécules provenant de sources renouvelables, telles que des extraits de plantes, les algues ou des composés dérivés de la biomasse [45–47]. Ces molécules peuvent agir comme des agents de liaison, des stabilisateurs ou des agents réactifs sur la surface des nanoparticules, offrant ainsi des fonctionnalités spécifiques tout en réduisant l'utilisation de produits chimiques synthétiques.

La fonctionnalisation de surface dans la chimie verte des nanoparticules vise à obtenir des propriétés améliorées tout en minimisant l'utilisation de produits chimiques nocifs et en favorisant des approches respectueuses de l'environnement. Cela permet d'ouvrir la voie à des applications plus durables et responsables des nanoparticules.

### II.2.2 Synthèse des nanocristaux à base des extraits des plantes

La synthèse de nanocristaux à base d'extraits de plantes est une approche de chimie verte qui utilise des extraits de plantes riches en composés réducteurs pour la réduction et la croissance contrôlée de nanocristaux. Cette méthode évite l'utilisation de réactifs chimiques toxiques ou dangereux souvent utilisés dans les méthodes de synthèse conventionnelles. Les extraits de plantes contenant des composés réducteurs, tels que les polyphénols, les flavonoïdes ou les acides organiques, sont sélectionnés pour leur capacité à réduire les précurseurs de nanocristaux [48]. Différentes plantes peuvent être utilisées en fonction de la disponibilité des extraits et des propriétés souhaitées des nanocristaux. Les extraits de plantes sont préparés en utilisant des techniques appropriées telles que l'extraction par solvant ou l'extraction à l'eau [49,50]. Les extraits sont obtenus en extrayant les composés réducteurs de la plante et en les concentrant pour une utilisation ultérieure. Les sels métalliques ou les précurseurs appropriés pour les NCs souhaités sont préparés séparément. Ces précurseurs peuvent être des sels de métaux tels que l'argent, le cuivre, le zinc ou le fer, qui seront réduits par les extraits de plantes. Les extraits de plantes sont mélangés avec les précurseurs de NCs dans une solution réactionnelle appropriée. La réduction des précurseurs est initiée par les composés réducteurs présents dans les extraits de plantes. Les extraits agissent comme des agents réducteurs pour convertir les ions métalliques en atomes métalliques. Une fois que les ions métalliques sont réduits, les atomes métalliques se regroupent pour former des noyaux de nanocristaux. La croissance contrôlée des nanocristaux est obtenue en ajustant les conditions réactionnelles telles que la température, le pH, la concentration des précurseurs et la durée de réaction. Cela permet de contrôler la taille, la forme et la composition des nanocristaux formés. Après la synthèse, les NCs sont

généralement purifiés par lavage pour éliminer les résidus réactionnels et les excès d'extraits de plantes. Les NCs peuvent ensuite être caractérisés en utilisant des techniques d'analyse telles que la microscopie électronique, la spectroscopie UV-Visible, la photoluminescence etc., pour évaluer leur taille, leur forme, leur structure et leurs propriétés optiques. Il est important de noter que la synthèse des nanocristaux à base des extraits de plantes peuvent varier en fonction des plantes utilisées, des précurseurs de nanocristaux et des conditions spécifiques de la réaction. ***Tableau I.3*** présente la caractérisation des nanoparticules biosynthétisées à partir d'extraits de plantes.

***Tableau I.3*** **:** caractérisation de nanoparticules biosynthétisées à partir d'extraits de plantes.

| NPs | Plante | Partie du Plante | Taille du NPs | Morphologie des NPs | Références |
|---|---|---|---|---|---|
| Ag | T. officinale | Feuille | 5-30 | Sphérique | [51] |
| $TiO_2$ | *E. purpurea* | Plante entière | 120 | Sphérique | [52] |
| Au | *Zinnia elegans* | Plante entière | <25 | Sphérique | [53] |
| CuO | *T. procumbens* | Feuille | 16 | Tige, sphérique | [54] |
| ZnO | *C. scolymus* | Feuille | 65.9 | Sphérique | [55] |
| $Fe_3O_4$ | *A. pseudocotula* | Pièces aériennes | 11-19 | Sphérique | [56] |
| MnO | *D. tombolens* | Pièces aériennes | 38 | Sphérique | [57] |
| ZnS | *Acalypha indica* | Plante entière | 32 | Sphérique | [58] |

## II.3 Propriétés spécifiques des nanocristaux

### II.3.1 Propriétés structurales

Les NCs semi-conducteurs présentent majoritairement une structure cristalline zinc blende, à savoir une structure cubique face centrées de groupe d'espace $F\overline{4}3m$ [59]. Cependant, une seconde structure, moins fréquente, de type wurtzite ou une structure hexagonale de groupe d'espace p63mc [60]. Pour le cas de ZnS, la structure ZB est la phase thermodynamiquement stable à basse température alors que la structure WZ est plus stable à haute température [61]. Les principaux facteurs qui déterminent la structure des NCs sont les conditions de synthèse (température, nature de solvant…) et la nature des ligands [62].

### II.3.2 Propriétés électroniques

#### II.3.2.1 Confinement quantique

A l'état massif, la structure électronique d'un semi-conducteur présente une bande de valence (BV) pleine et une bande de conduction (BC) vide, séparées par une bande interdite, le gap, de largeur Eg. Dans le cas d'un nanocristal, les bandes se séparent en niveaux discrets. **(*Figure***

***I.9)***. Par ailleurs, un nanocristal peut être considéré comme un puits de potentiel de taille nanométrique où sont confinés les électrons. Cette taille étant du même ordre de grandeur que la longueur d'onde de Broglie (λ) définie par [63] :

$$\lambda=\frac{\hbar}{\sqrt{2m^{*}E}} \qquad \text{(I.1)}$$

Où $\hbar$ est la constante de Planck, E est l'énergie du porteur de charge et m* sa masse effective. L'effet de taille quantique apparaît pour des distances inférieures à la longueur d'onde thermique de De Broglie sinon la quantification est occultée par l'agitation thermique $k_B T$.Cela modifie la structure électronique et tend à écarter les niveaux électroniques les uns des autres, d'autant plus que le rayon du nanocristal r est faible : c'est le confinement quantique. La diminution de taille des NCs semi-conducteurs conduit à une augmentation de la gap bande interdite. Ainsi les maximums d'absorption et de luminescence se décalent vers les hautes énergies (petites longueurs d'onde) par rapport au matériau massif. Il est donc possible de moduler la longueur d'onde d'émission des NCs du proche infrarouge à l'ultraviolet en contrôlant la taille.

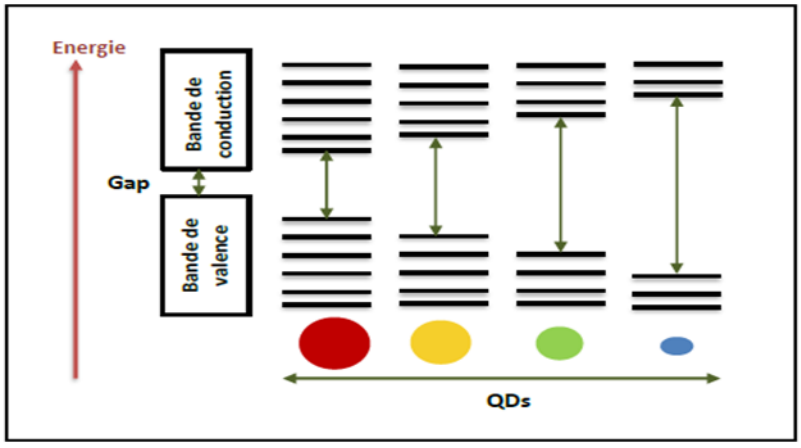


***Figure I.9*** **:** Présentation schématique de l'évolution de la structure électronique entre solide massif et nanocristal de taille décroissante

### II.3.2.2 Effet de la taille sur le confinement quantique

En fonction de la taille de la particule, il devient possible de faire varier la largeur de la bande d'énergie interdite Eg, qui se situe entre la BV et la BC. Eg peut se définir en première approximation avec l'équation déterminée par L.E. Brus en 1986 [64]. Il a proposé un modèle simple pour le calcul du gap donné par l'équation (1) :

$$E_g^{Nano}(\mathrm{r})=E_g^{massif}+\frac{\hbar}{2}\frac{\pi^2}{r^2}\left(\frac{1}{m_e^*}+\frac{1}{m_h^*}\right)-\frac{1.8e^2}{\varepsilon r}-0.248E_{Rydberg}^{*}$$

(I .2)

Le premier terme est la valeur de la bande interdite du matériau massif en (eV), le deuxième terme représente l'énergie cinétique avec **r** le rayon de la nanoparticule en (nm), le troisième terme est relatif à l'interaction Coulombienne entre l'électron et le trou (avec $\boldsymbol{\varepsilon = \varepsilon_0 \varepsilon_r}$). Le dernier terme concerne la corrélation spatiale entre l'électron et le trou, il est très faible par rapport aux autres termes de telle sorte qu'on peut le négliger.

Comme mentionné précédemment, la valeur énergétique de la bande interdite augmente avec la diminution du rayon et est caractérisé par le rayon de Bohr de l'exciton de matériau massif $r_B$. Celui-ci représente l'interaction coulombienne entre les charges de l'électron et du trou :

$$\mathbf{r_B = \frac{\hbar^2 \varepsilon_r}{e^2} \frac{1}{m_e^*} + \frac{1}{m_h^*}} \qquad \text{(I .3)}$$

Il est possible d'introduire ce rayon dans l'équation (I.2) afin de pouvoir calculer la valeur de la bande interdite à partir des paramètres du matériau semi-conducteur :

$$\mathbf{E_g^{Nano}(r) = E_g^{massif} + \frac{e^2}{\varepsilon_r r} \frac{\hbar \pi^2 r_B}{2r} - \frac{1.8}{\varepsilon_0} = E_g^{massif} + \frac{2.6}{\varepsilon_r r} \left( 2.74 \frac{r_B}{r} - 1 \right)} \qquad \text{(I .4)}$$

Après formation de l'exciton, le système aura tendance à revenir à son état initial, plus stable, et l'électron se recombine avec le trou. Si le retour à l'état initial donne lieu à l'émission d'un photon, alors le phénomène est dit radiatif. Cependant, certains éléments peuvent perturber ce phénomène, en particulier le milieu extérieur et les défauts de structures en volume et en surface de la particule.

### II.3.2.3 Régime de confinement quantique

La mise en évidence expérimentale de l'effet de la taille sur le confinement quantique de l'exciton a été obtenue par Ekimov et Onushchenko en 1981 [65] sur des micro- cristallites de CuCl dispersés dans un verre silicaté. Ils observèrent un décalage vers le bleu du principal pic d'absorption avec la diminution de la taille des particules. Et c'est en 1982 qu'Efros [66] y apposèrent un modèle théorique. Il repose sur les hypothèses suivantes :

- Les particules possèdent une forme sphérique avec une barrière de potentiel infinie à l'extérieur des particules.
- L'approximation des masses effectives (EMA)
- Des bandes d'énergie paraboliques.

On distingue 3 régimes de confinement **(*Figure I.10*)**. Ils sont définis par comparaison du rayon R du NC relativement au rayon de Bohr $a_B$ **[52]** :

- **Le régime de confinement faible : R > $\boldsymbol{a_B}$ :**

Dans ce régime de confinement, les dimensions de la nanoparticule sont plus grandes que le rayon de l'exciton ($R >> a_B$) et l'énergie coulombienne est dominante. Par conséquent, la formation de l'exciton est plus favorable. On retrouve alors le cas de l'exciton du SC massif.

- **Le régime de confinement intermédiaire : R ~$a_B$:**

Dans ce cas le rayon de Bohr est de même ordre que celui du nanocristal. L'électron et le trou, sont confinés différemment.

- **Le régime de confinement fort : R< $a_B$ :**

Ce régime de confinement apparaît quand la taille de la particule est inférieure au rayon de l'exciton ($R \leq a_B$). L'énergie de confinement dans ce cas est dominante et les deux porteurs de charges (électron et trou) sont indépendamment confinés.

Enfin, l'expérience montre que les conditions requises pour être dans l'un de ces deux régimes sont : R > 3 $a_B$ pour le régime de confinement faible et R <$a_B$ pour le régime de confinement fort.

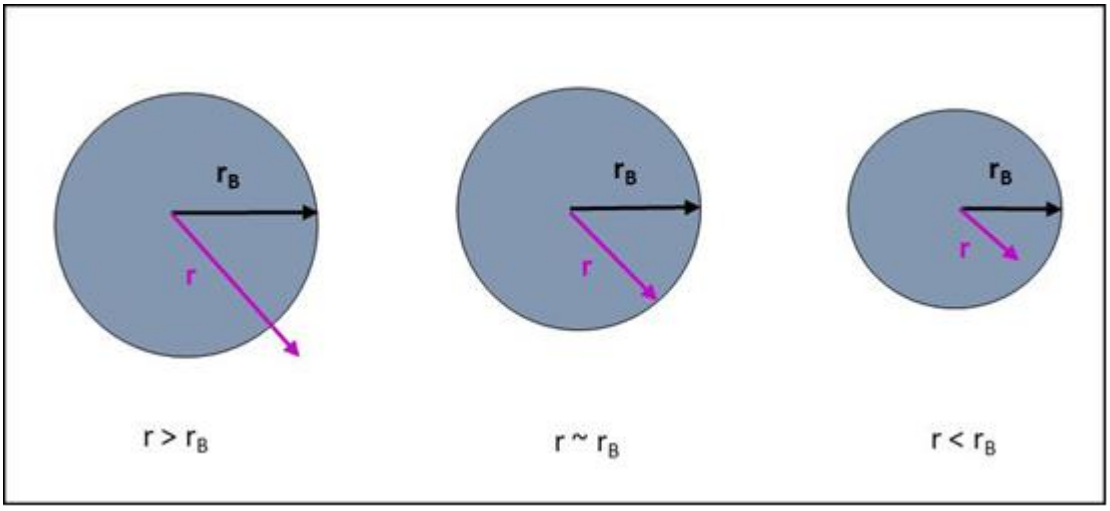


***Figure I.10*:** Représentation schématique des trois régimes de confinement d'un nanocristal

### II.3.3 Propriétés optiques

#### II.3.3.1 Absorption UV-visible

L'absorption d'un photon par le NC a lieu si son énergie est supérieure ou égale au gap du matériau à des niveaux d'énergie confinés. En raison du phénomène de confinement quantique, une diminution du diamètre des nanocristaux entraîne un déplacement hypsochrome, c'est-à-dire vers des énergies plus élevées et donc vers des longueurs d'onde plus faibles au seuil d'absorption. Le spectre d'absorption révèle un maximum bien défini correspondant à la transition

optique du premier état excitonique [67]. La position de ce signal dépend de la valeur énergétique de la bande interdite. Cette bande d'absorption est reliée à la taille des NCs et sa forme et sa largeur résultant de la distribution en taille des NCs considères. Ainsi, un échantillon polydispersé ne présentera généralement qu'un épaulement à la longueur d'onde de la transition excitonique **(*Figure I.11*)**.

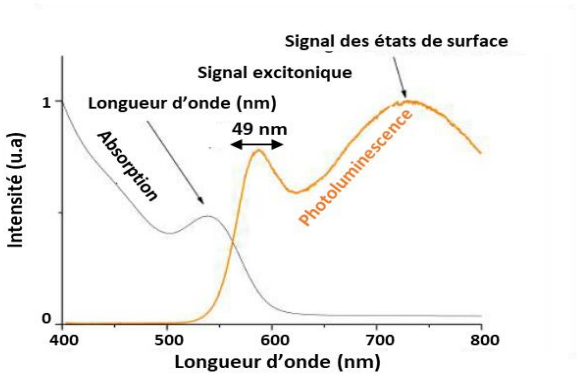


***Figure I.11*** : Spectres d'absorption et de photoluminescence d'une solution colloïdale de NCs semi-conducteurs

### II.3.3.2 Photoluminescence

L'absorption d'un photon par un matériau va exciter un électron à partir de la bande de valence vers la bande de conduction en formant un trou dans la bande de valence. Le retour de l'électron à l'état fondamental se traduit par l'émission d'un photon (ou d'un phonon). On distingue plusieurs chemins pour la désexcitation de pair électron – trou :**(*Figure I.12*)**

- **Une émission radiative des bords de bandes** (interbande) : dans ce cas les spectres d'émission se caractérisent par un pic intense dont l'énergie est liée à la taille des nanocristaux et dont la largeur à mi-hauteur est une caractéristique de la dispersion en taille des nanocristaux.
- Une émission radiative faisant intervenir des niveaux intermédiaires : elle est assurée via des impuretés ou bien des défauts, les spectres d'émission se caractérisent par un pic large à une énergie plus faible que celle du pic d'émission de bord de bande. Ce type d'émission est dû à des pièges de surface « deep traps » qui créent des niveaux d'énergie dans la bande interdite.
- Des émissions non radiatives : Elles peuvent faire intervenir des défauts. Plus ils sont nombreux, plus le rendement quantique est faible.

En théorie, la photoluminescence correspond à l'émission d'un photon d'énergie égale au gap Eg. En fait, la raie de PL est déplacée de quelques nm vers les grandes longueurs d'onde par rapport au pic excitonique dans le spectre d'absorption. Ce décalage appelé décalage de Stokes [68]. Ce déplacement est dû à une légère perte d'énergie de l'électron excite entre le moment de son excitation et de sa relaxation. Cette perte se fait soit sous forme de chaleur, soit sous forme de phonons (énergie de vibration). La présence de défauts peut également engendrer la recombinaison électron-trou a plus faible énergie par des canaux non radiatifs entrainant alors une perte d'efficacité de l'émission du QD [69]. Ce phénomène se traduit par l'apparition d'un large signal à hautes longueurs d'ondes que nous appellerons « signal des états de surface » (***Figure I.12***).

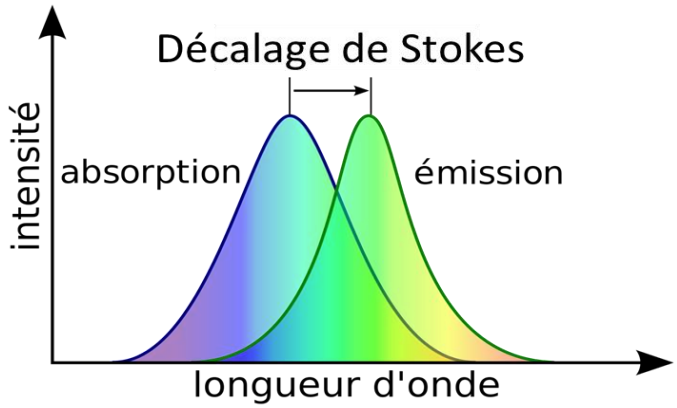


***Figure I.12*****:** Représentation schématique de décalage de Stockes dans les NCs

### II.3.3.3 Rendement quantique (RQ)

Le rendement quantique de luminescence (RQ) est la probabilité d'émission d'un photon par luminescence après absorption d'un photon d'énergie supérieure. En général des phénomènes de désexcitation non radiatifs ont lieu et donc le rendement quantique est inférieur à 100 %. Cette mesure est réalisée en comparant le rapport des nombres de photons émis et absorbés par l'échantillon à un fluorophore de référence dont le rendement quantique est connu. Cette méthode nécessite d'avoir un spectre d'émission et d'absorbance pour le fluorophore de référence et pour l'échantillon à mesurer. Le rendement quantique est donné par [70] :

$$\boldsymbol{\Phi_{QDs} = \Phi_{ref} \frac{A_{Ref}}{A_{QDs}} \frac{F_{QDs}}{F_{REF}} \frac{n_{QDs}{}^2}{n_{REF}{}^2}} \qquad \text{(I .5)}$$

Où les indices $R_{ef}$ et QDs indiquent l'espèce considérée, le fluorophore de référence (dans notre étude ; Rhodamine 6G) et les quantums dots respectivement, $A_i$est l'absorbance de l'échantillon à la longueur d'onde d'excitation, $F_i$ est l'aire sous la courbe de fluorescence, $n_i$est l'indice du

solvant utilisé pour faire les spectres et $\Phi_{ref}$ est le rendement quantique du fluorophore de référence.

## III. Applications des nanocristaux de semi-conducteurs de ZnS

Aujourd'hui, les nanocristaux semi-conducteurs de ZnS jouent un rôle crucial dans des domaines distincts comme les cellules photovoltaïques [71], les capteurs [72], les modulateurs [73], l'optoélectronique [74], les LEDs [75], et la photocatalyse [76] (***Figures I.13***).

Au fil de cette thèse, nous découvrirons comment les nanocristaux de semi-conducteurs luminescents ouvrent la voie à de nouvelles possibilités technologiques et scientifiques. Leur potentiel est immense, et ils continuent d'être étudiés et explorés dans de nombreux domaines. Les applications présentées ici ne représentent qu'une fraction de ce que les nanocristaux de semi-conducteurs luminescents peuvent accomplir. Leur capacité à manipuler la lumière à l'échelle nanométrique ouvre la porte à des avancées passionnantes et prometteuses, qui pourraient transformer notre manière d'afficher, de capter, de stocker et d'interagir avec la lumière.

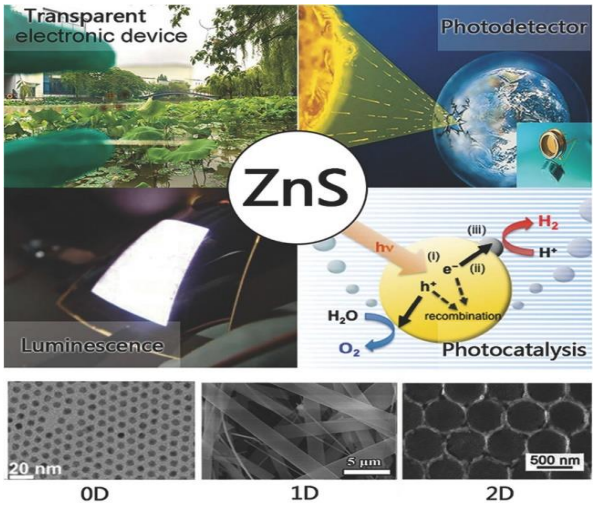


***Figure I.13*** : Applications des nanocristaux semi-conducteurs de ZnS

### III.1 Optoélectronique

Les nanocristaux semi-conducteurs de sulfure de zinc (ZnS) ont suscité un grand intérêt dans les applications optoélectroniques en raison de leurs propriétés optiques et électroniques uniques. Ces NCs peuvent être utilisés comme matériaux émissifs dans les LED [77]. En contrôlant la taille des nanocristaux, leur longueur d'onde d'émission peut être réglée, ce qui permet de produire des LED qui émettent de la lumière dans une large gamme de couleurs. Ces LED à base de nanocristaux ont des applications potentielles dans les domaines de l'affichage,

de l'éclairage et de la signalisation [78]. Ces nouveaux nanomatériaux peuvent être exploités comme matériaux actifs dans les photodétecteurs pour la détection de la lumière dans tout le spectre électromagnétique [79]. Leurs propriétés optiques uniques, telles qu'une sensibilité élevée et un temps de réponse rapide, les rendent appropriés pour des applications telles que l'imagerie, les communications optiques et la détection. Aussi, ils peuvent être incorporés dans les cellules solaires afin d'améliorer leur absorption de la lumière et leur efficacité de conversion de l'énergie [80]. En combinant les nanocristaux de ZnS avec d'autres matériaux semi-conducteurs, tels que des absorbeurs organiques ou inorganiques, il est possible de fabriquer des cellules solaires hybrides plus performantes. L'imagerie biomédicale représente une application pertinente à travers les agents de contraste dans les techniques d'imagerie biomédicale, notamment l'imagerie par fluorescence et la bioimagerie [81]. Leurs propriétés fluorescentes puissantes et accordables, associées à des revêtements biocompatibles, permettent l'imagerie à haute résolution et le suivi de structures et de processus biologiques.

## III.2 Photodégradation des polluants organiques

### III.2.1 Adsorption

Les nanocristaux de ZnS sont couramment utilisés pour l'adsorption de polluants organiques en raison de leur stabilité chimique dans les environnements aqueux, de leur affinité pour de nombreux polluants organiques et de leurs propriétés spécifiques [82].

L'adsorption est un processus par lequel des molécules ou des particules sont retenues à la surface d'un matériau solide ou liquide. L'adsorption peut se produire par divers mécanismes, tels que des forces de van der Waals, des liaisons chimiques ou des interactions électrostatiques. Ce phénomène résulte de l'existence, des forces à la surface du solide, qui sont de nature physique ou chimique. Ces forces conduisent respectivement à deux types d'adsorption : la chimisorption et la physisorption [83]. Ce processus est largement utilisé dans de nombreuses applications, notamment dans le domaine environnemental, pour la dépollution, la purification de l'eau, la capture de gaz, la séparation des composés chimiques, et dans l'industrie chimique et pharmaceutique [84]. Les matériaux utilisés pour l'adsorption sont souvent des matériaux poreux à grande surface spécifique, tels que les charbons actifs, les zéolithes, les argiles ou les nanoparticules [85–89]. Ces matériaux offrent une surface étendue pour l'adsorption des substances ciblées. L'adsorption est une méthode couramment utilisée dans le domaine de la purification de l'eau pour éliminer les contaminants organiques, les métaux lourds et d'autres substances indésirables. Elle est également utilisée dans les processus de filtration, la séparation des gaz, la chromatographie et la purification des produits chimiques. L'efficacité de

l'adsorption dépend de plusieurs facteurs, tels que la nature des molécules à adsorber, la surface et la porosité du matériau adsorbant, les conditions de température et de pression, ainsi que le temps de contact entre le matériau adsorbant et les molécules à adsorber. L'adsorption est un domaine de recherche actif, visant à développer de nouveaux matériaux adsorbants plus efficaces et sélectifs, ainsi qu'à optimiser les procédés d'adsorption pour une utilisation plus large dans diverses applications comme la photocatalyse.

### III.2.2 La photocatalyse des polluants organiques

Avec l'évolution des quantums dots (QDs) solubles dans l'eau au niveau de la synthèse et de la modification de surface, des photocatalyseurs à base des QDs sont largement utilisées dans les domaines industriels et biologiques [90]. Dans ce contexte, les nanocristaux ont acquis un grand intérêt dans le domaine de la photocatalyse et la dégradation des colorants organiques rejetés dans l'environnement par les sociétés industrielles [91]. Afin de minimiser cette pollution de l'environnement, des efforts doivent être pris dans l'ensemble des secteurs d'activité particulièrement le secteur industriel qui est la principale cause de pollution.

La photocatalyse est un processus dans lequel un catalyseur est activé par l'absorption des photons générant des agents oxydants capables de dégrader des molécules organiques. Cette technique est dite hétérogène si le photocatalyseur est dans un état physique différent de celui de colorant organique c'est-à-dire il ne doit être ni consommé ni altéré [92]. La photocatalyse permet d'éliminer nombreux composés organiques qui sont des sources de pollutions comme les colorants organiques. La photocatalyse exploite l'interaction entre la lumière et le matériau photocatalytique. Lorsque la lumière atteint la surface du matériau photocatalytique, les photons sont absorbés, ce qui excite les électrons du matériau. Les électrons excités peuvent réagir avec les molécules adsorbées à la surface du matériau, tandis que les trous laissés par les électrons peuvent réagir avec d'autres espèces présentes dans le système [93].

Les matériaux couramment utilisés en photocatalyse comprennent des oxydes métalliques tels que le dioxyde de titane (TiO2), le sulfure de zinc (ZnS), l'oxyde de zinc (ZnO) et le sulfure de cadmium (CdS) [94–96]. Ces matériaux présentent des bandes d'énergie appropriées qui leur permettent d'absorber efficacement la lumière et de générer des paires électron-trou. La photocatalyse a de nombreuses applications, en particulier dans le domaine environnemental. Elle est utilisée pour la dégradation des polluants organiques dans l'eau et l'air, contribuant ainsi à la dépollution et à la purification de l'environnement. La photocatalyse peut également être utilisée dans la production d'énergie, la synthèse de produits chimiques, la purification de l'eau potable, la stérilisation et bien d'autres domaines [97]. Cette technique présente plusieurs

avantages, notamment une utilisation de l'énergie solaire renouvelable, une efficacité élevée, une réduction des sous-produits indésirables, une large applicabilité à différents types de polluants et une faible consommation d'énergie.

### III.3 Capteurs des gaz

Les microcapteurs sont déjà une source cruciale d'innovation [98]. Ces dernières années, des améliorations significatives ont été apportées aux méthodes de conception et de fabrication des capteurs et des avancées significatives dans les technologies de microcapteurs utilisant des matériaux nouvellement conçus, résultent en des capteurs de gaz à haute sensibilité.
Les capteurs de gaz sont un type particulièrement efficace de dispositif de détection profonde, avec un large éventail d'applications dans le domaine des soins de santé suscitant un énorme intérêt dans le monde entier [99].Plusieurs caractéristiques, telles que la sensibilité de l'appareil, la sélectivité, la précision, la limite de détection (LOD), la résolution, la précision, la réversibilité, le temps de récupération et le temps de réponse, sont utilisés pour évaluer la capacité de détection [100]. De plus, la miniaturisation des appareils et la puissance la consommation, les matériaux coûteux et les durées de vie prolongées sont des variables essentielles dans le développement capteurs dans diverses applications. Nous avons mis en évidence dans le sous-chapitre suivant les apports de la chromatographie, des capteurs électrochimiques (semi-conducteur à oxyde métallique et à base organique capteurs de gaz chimirésistifs), capteurs à nanotubes de carbone, capteurs de gaz acoustiques (acoustique de surface onde, capteur de gaz capacitif micromachine), capteurs optiques et capteurs de gaz à cristal photonique [101].
Les capteurs de gaz à base de nanoparticules sont des dispositifs qui utilisent des nanoparticules pour détecter et mesurer la présence de différents gaz dans l'environnement [72]. Ces capteurs sont basés sur les propriétés uniques des nanoparticules qui peuvent réagir de manière spécifique aux gaz ciblés, ce qui permet de détecter leur présence et de quantifier leur concentration.
Les nanoparticules utilisées dans les capteurs de gaz peuvent être de différents types, tels que des nanoparticules métalliques, des oxydes métalliques ou des nanoparticules de carbone. Chaque type de nanoparticule présente des propriétés chimiques et physiques spécifiques qui peuvent être exploitées pour la détection de gaz.
Lorsque les nanoparticules sont exposées à un gaz spécifique, une réaction se produit entre les molécules de gaz et la surface des nanoparticules. Cette réaction peut entraîner des changements dans les propriétés électriques, optiques ou chimiques des nanoparticules, ce qui peut être mesuré et quantifié par le capteur. Par exemple, la présence d'un gaz peut modifier la

conductivité électrique des nanoparticules, la résistance électrique d'un film contenant les nanoparticules ou même provoquer des changements de couleur des nanoparticules [72].

La détection des changements induits par les gaz sur les nanoparticules peut se faire de différentes manières. Les capteurs de gaz à base de nanoparticules peuvent utiliser des techniques telles que la mesure de la conductivité électrique, la spectroscopie optique, la résonance plasmonique de surface ou la variation des propriétés électrochimiques [102].

Ces capteurs offrent plusieurs avantages, tels qu'une sensibilité élevée, une faible consommation d'énergie, une réponse rapide et une taille réduite. Ils peuvent être utilisés dans de nombreux domaines, tels que la surveillance de la qualité de l'air, le contrôle des émissions industrielles, la sécurité alimentaire ou la détection de gaz toxiques.

## IV. Conclusion

Dans cette partie bibliographique, nous avons présenté les principales propriétés physiques des nanocristaux semi-conducteurs II-VI. Ces propriétés sont beaucoup affectées par l'effet de confinement quantique, et deviennent modulables selon la forme et la taille des nanocristaux. La grande réactivité de surface permet aussi de fonctionnaliser ses nanocristaux, obtenus des solutions colloïdales, par des ligands organiques pouvant servir pour plusieurs applications dans divers domaines technologiques. Ensuite nous avons présenté les propriétés des nanocristaux mettant en évidence les voies de synthèse organique et verte.

Notre travail porte principalement sur la préparation des NCs ternaires ZnS par deux méthodes de synthèse organique et verte dans le but de les exploiter dans la photocatalyse des polluants organiques et les capteurs de gaz.

# V. References


[1] G. Suchaneck, E. Artiukh, G. Gerlach, Resistivity and Tunnel Magnetoresistance in Double-Perovskite Strontium Ferromolybdate Ceramics, Physica Status Solidi (b). 259 (2022) 2200012. https://doi.org/10.1002/pssb.202200012.

[2] S. Kumar, K.P. Tiwary, Cadmium Selenide Thin Film Deposition and Characterization for Photovoltaic Applications, in: Z.H. Khan (Ed.), Nanomaterials for Innovative Energy Systems and Devices, Springer Nature, Singapore, 2022: pp. 333–367. https://doi.org/10.1007/978-981-19-0553-7_9.

[3] P. Mondal, S. Chakraborty, G.K. Grandhi, R. Viswanatha, Copper Doping in II–VI Semiconductor Nanocrystals: Single-Particle Fluorescence Study, J. Phys. Chem. Lett. 11 (2020) 5367–5372. https://doi.org/10.1021/acs.jpclett.0c01570.

[4] Physique de l'état solide, 2023. https://www.dunod.com/sciences-techniques/physique-etat-solide-cours-et-problemes-0 (accessed October 2, 2023).

[5] Y. Lukan, A. Hotynchan, Y. Andriichuk, S. Vojtovych, Y. Seti, Y. Khalavka, II–VI Semiconductor-Based Nanomaterials, in: G. Korotcenkov (Ed.), Handbook of II-VI Semiconductor-Based Sensors and Radiation Detectors: Volume 1, Materials and Technology, Springer International Publishing, Cham, 2023: pp. 325–357. https://doi.org/10.1007/978-3-031-19531-0_12.

[6] S. Mabrouk, Synthèse par voie colloïdale et étude des propriétés optiques et structurales de nanocristaux ternaires ZnSeS dopés, These de doctorat, Université de Lorraine, 2022. https://www.theses.fr/2022LORR0169 (accessed October 2, 2023).

[7] A. Bala, R. Sehrawat, A.K. Sharma, P. Soni, Luminescent properties of polyaniline capped Mn doped ZnS quantum dots, Journal of Metals, Materials and Minerals. 31 (2021) 151–157.

[8] M. Protiere, Synthèse de nanocristaux fluorescents de semi-conducteurs II-VI et III-V. Augmentation de l'échelle de synthèse, These de doctorat, Université Joseph Fourier (Grenoble ; 1971-2015), 2007. https://www.theses.fr/2007GRE10188 (accessed October 3, 2023).

[9] N. Bel Haj Mohamed, M. Bouzidi, N. Ben brahim, L. Sellaoui, M. Haouari, H. Ezzaouia, A. Bonilla-Petriciolet, Impact of the stacking fault and surface defects states of colloidal CdSe nanocrystals on the removal of reactive black 5, Materials Science and Engineering: B. 265 (2021) 115029. https://doi.org/10.1016/j.mseb.2020.115029.

[10] M. Khawla, H. Zouhour, C. Yves, H. Souhaira, M. Rym, ZnS quantum dots as fluorescence sensor for quantitative detection of tetracycline, Optical Materials. 125 (2022) 112103. https://doi.org/10.1016/j.optmat.2022.112103.

[11] S. Mabrouk, H. Rinnert, L. Balan, J. Jasniewski, S. Blanchard, G. Medjahdi, R. Ben Chaabane, R. Schneider, Highly Luminescent and Photostable Core/Shell/Shell ZnSeS/Cu:ZnS/ZnS Quantum Dots Prepared via a Mild Aqueous Route, Nanomaterials. 12 (2022) 3254. https://doi.org/10.3390/nano12183254.

[12] N. Mohamed, M. Bouzidi, S. Ouni, A. Alshammari, Z. Khan, M. Gandouzi, M. Mohamed, N. Chaaben, A. Bonilla-Petriciolet, M. Haouari, Statistical physics analysis of adsorp-

tion isotherms and photocatalysis activity of MPA coated $CuInS_2$/ZnS nanocrystals for the removal of methyl blue from wastewaters, Inorganic Chemistry Communications. 144 (2022) 109933. https://doi.org/10.1016/j.inoche.2022.109933.

[13] C.B. Murray, D.J. Norris, M.G. Bawendi, Synthesis and characterization of nearly monodisperse CdE (E = sulfur, selenium, tellurium) semiconductor nanocrystallites, ACS Publications. (2002). https://doi.org/10.1021/ja00072a025.

[14] J.J. Calvin, A.S. Brewer, A.P. Alivisatos, The role of organic ligand shell structures in colloidal nanocrystal synthesis, Nat Synth. 1 (2022) 127–137. https://doi.org/10.1038/s44160-022-00025-4.

[15] A. Guha, T.K. Paira, S. Sarkar, Transparent Conducting Oxide Nanocrystals: Synthesis, Challenges, and Future Prospects for Optoelectronic Devices, Physica Status Solidi (a). 220 (2023) 2300351. https://doi.org/10.1002/pssa.202300351.

[16] M. Wolska-Pietkiewicz, M. Jędrzejewska, K. Tokarska, J. Wielgórska, M. Chudy, J. Grzonka, J. Lewiński, Towards bio-safe and easily redispersible bare ZnO quantum dots engineered via organometallic wet-chemical processing, Chemical Engineering Journal. 455 (2023) 140497. https://doi.org/10.1016/j.cej.2022.140497.

[17] J. Oh, A. Beck, E.D. Goodman, L.T. Roling, A. Boucly, L. Artiglia, F. Abild-Pedersen, J.A. van Bokhoven, M. Cargnello, Colloidally Engineered Pd and Pt Catalysts Distinguish Surface- and Vapor-Mediated Deactivation Mechanisms, ACS Catal. 13 (2023) 1812–1822. https://doi.org/10.1021/acscatal.2c04683.

[18] L. Labrador-Páez, U. Kostiv, J. Widengren, H. Liu, Water: An Influential Agent for Lanthanide-Doped Luminescent Nanoparticles in Nanomedicine, Advanced Optical Materials. 11 (2023) 2200513. https://doi.org/10.1002/adom.202200513.

[19] A.I. Ekimov, Al.L. Efros, A.A. Onushchenko, Quantum size effect in semiconductor microcrystals, Solid State Communications. 56 (1985) 921–924. https://doi.org/10.1016/S0038-1098(85)80025-9.

[20] H. Lv, X. Zhang, L. Zhang, Y. Liu, C. Geng, S. Xu, A mixed-ligand strategy for size-controlled synthesis of hydrophobic ZnO nanocrystals by microfluidic reactor, Colloids and Surfaces A: Physicochemical and Engineering Aspects. 673 (2023) 131827. https://doi.org/10.1016/j.colsurfa.2023.131827.

[21] P. Wang, S. Bao, S. Qiao, C. Li, Z. Jiang, H. Song, Y. Wang, Q. Zhan, L. Huang, Luminescent nanoparticle-arrays synthesized via polymer pen lithography, Nano Res. 16 (2023) 3125–3129. https://doi.org/10.1007/s12274-022-4968-0.

[22] P. Jastrzebska-Perfect, W. Zhu, M. Saravanapavanantham, Z. Li, S.O. Spector, R. Brenes, P.F. Satterthwaite, R.J. Ram, F. Niroui, On-site growth of perovskite nanocrystal arrays for integrated nanodevices, Nat Commun. 14 (2023) 3883. https://doi.org/10.1038/s41467-023-39488-0.

[23] L. Pang, M. Wu, Z. Chai, H. Liu, Y. Chen, B. Jin, X. Cao, Preparation and dye separation performance of ZIF-67/mesoporous silica ceramic nanofiltration membrane by liquid phase epitaxy (LPE) growth method, Separation and Purification Technology. 322 (2023) 124339. https://doi.org/10.1016/j.seppur.2023.124339.

[24] M. Hakami, C.-C. Tseng, K. Nanjo, V. Tung, J.-H. Fu, Wafer-scale epitaxy of transition-metal dichalcogenides with continuous single-crystallinity and engineered defect density, MRS Bulletin. (2023). https://doi.org/10.1557/s43577-023-00598-1.

[25] V. Venkatachalam, S. Ganapathy, I. Perumal, M. Anandhan, Crystal shape and size of CdTe colloidal quantum dots controlled by silver doping for enhanced quantum dots sensitized solar cells performance, Colloids and Surfaces A: Physicochemical and Engineering Aspects. 656 (2023) 130296. https://doi.org/10.1016/j.colsurfa.2022.130296.

[26] W. Zhou, H. Huang, X. Liu, J. Gao, S. Hao, Y. Yang, J. Qiu, Perspective on the Preparation Methods of Single Crystalline High Nickel Oxide Cathode Materials, Advanced Energy Materials. 13 (2023) 2300378. https://doi.org/10.1002/aenm.202300378.

[27] F. Gao, Y. Tang, J. Liu, K. Pan, M. Zhou, G. Qian, M. Liu, F. Yu, J. Dan, B. Dai, Nickel foam supported CuCe mixed metal oxide as monolith catalyst for NO removal, Chemical Engineering Journal. 474 (2023) 145713. https://doi.org/10.1016/j.cej.2023.145713.

[28] M. Abdollahy, H. Peyman, H. Roshanfekr, A.O. Idris, S. Azizi, L.L. Sibali, Synthesis and characterization of a smart polymer-coated core–shell MnFe2O4@ organometallic framework for targeted drug delivery, Chem. Pap. 77 (2023) 3897–3909. https://doi.org/10.1007/s11696-023-02750-2.

[29] E. Bellan, F. Maleki, M. Jakoobi, P. Fau, K. Fajerwerg, D. Lagarde, A. Balocchi, P. Lecante, J. Trébosc, Y. Xu, Z. Gan, L. Pautrot-d'Alençon, T. Le Mercier, H. Nagashima, G. Pacchioni, O. Lafon, Y. Coppel, M.L. Kahn, Ultra-High-Field 67Zn and 33S NMR Studies Coupled with DFT Calculations Reveal the Structure of ZnS Nanoplatelets Prepared by an Organometallic Approach, J. Phys. Chem. C. 127 (2023) 17809–17819. https://doi.org/10.1021/acs.jpcc.3c02754.

[30] T.B. Mbuyazi, P.A. Ajibade, Influence of Different Capping Agents on the Structural, Optical, and Photocatalytic Degradation Efficiency of Magnetite ($Fe_3O_4$) Nanoparticles, Nanomaterials. 13 (2023) 2067. https://doi.org/10.3390/nano13142067.

[31] B.H. Kiani, Q. Ajmal, N. Akhtar, I. Haq, M.A. Abdel-Maksoud, A. Malik, M. Aufy, N. Ullah, Biogenic Synthesis of Zinc Oxide Nanoparticles Using Citrullus colocynthis for Potential Biomedical Applications, Plants. 12 (2023) 362. https://doi.org/10.3390/plants12020362.

[32] P.N.P. Ghoderao, C.-W. Lee, H.-S. Byun, Phase behavior investigation of the vinyl toluene and poly (vinyl toluene) + co-solvents in supercritical $CO_2$, Journal of Industrial and Engineering Chemistry. 121 (2023) 92–99. https://doi.org/10.1016/j.jiec.2023.01.010.

[33] P. Gabriel, J. Liu, F. Staab, R. Streubel, M. Miertz, K. Durst, O. Gutfleisch, S. Barcikowski, A.R. Ziefuß, Upscaled laser synthesis of copper nanoparticles in acetone to correlate the surface modification of Nd-Fe-B feedstock properties with part properties after full melting and rapid solidification, (2023). https://doi.org/10.26434/chemrxiv-2023-g56vc.

[34] N. Brahim, M. Poggi, J.-C. Lambry, N. Mohamed, R. Chaabane, M. Negrerie, Density of Grafted Chains in Thioglycerol-Capped CdS Quantum Dots Determines Their Interaction with Aluminum(III) in Water, Inorganic Chemistry. 57 (2018). https://doi.org/10.1021/acs.inorgchem.7b03254.

[35] N. Bel Haj Mohamed, S. Ouni, M. Bouzid, M. Bouzidi, A. Bonilla-Petriciolet, M. Haouari, Synthesis and preparation of acid capped CdSe nanocrystals as successful adsorbent

and photocatalyst for the removal of dyes from water and its statistical physics analysis, Environ Sci Pollut Res. 29 (2022) 72747–72763. https://doi.org/10.1007/s11356-022-20990-9.

[36] C.B. Whitehead, S. Özkar, R.G. Finke, LaMer's 1950 model of particle formation: a review and critical analysis of its classical nucleation and fluctuation theory basis, of competing models and mechanisms for phase-changes and particle formation, and then of its application to silver halide, semiconductor, metal, and metal-oxide nanoparticles, Mater. Adv. 2 (2021) 186–235. https://doi.org/10.1039/D0MA00439A.

[37] W. Xu, Y. Ning, M. Wang, S. Zhang, H. Sun, Y. Yin, N. Li, P. Li, D. Luo, Construction of astaxanthin loaded Pickering emulsions gel stabilized by xanthan gum/lysozyme nanoparticles with konjac glucomannan from structure, protection and gastrointestinal digestion perspective, International Journal of Biological Macromolecules. 252 (2023) 126421. https://doi.org/10.1016/j.ijbiomac.2023.126421.

[38] W. Yin, J. Yang, K. Zhao, A. Cui, J. Zhou, W. Tian, W. Li, Z. Hu, J. Chu, High Responsivity and External Quantum Efficiency Photodetectors Based on Solution-Processed Ni-Doped CuO Films, ACS Appl. Mater. Interfaces. 12 (2020) 11797–11805. https://doi.org/10.1021/acsami.9b18663.

[39] Y. Fu, Y. Li, G. Xing, D. Cao, Surface passivation of perovskite with organic hole transport materials for highly efficient and stable perovskite solar cells, Materials Today Advances. 16 (2022) 100300. https://doi.org/10.1016/j.mtadv.2022.100300.

[40] R.V. Bordiwala, Green synthesis and Applications of Metal Nanoparticles.- A Review Article, Results in Chemistry. 5 (2023) 100832. https://doi.org/10.1016/j.rechem.2023.100832.

[41] P. Lozano, E. García-Verdugo, from green to circular chemistry paved by biocatalysis, Green Chem. 25 (2023) 7041–7057. https://doi.org/10.1039/D3GC01878D.

[42] H. Alsaeedi, H. Ahmad, M.F. Altowairqi, A.A. Alhamed, A. Alsalme, Covalently Functionalized Cellulose Nanoparticles for Simultaneous Enrichment of Pb(II), Cd(II) and Cu(II) Ions, Polymers. 15 (2023) 532. https://doi.org/10.3390/polym15030532.

[43] A.A.H. Abdellatif, A. Abdelfattah, M.A. Younis, S.M. Aldalaan, H.M. Tawfeek, Chitosan-capped silver nanoparticles with potent and selective intrinsic activity against the breast cancer cells, Nanotechnology Reviews. 12 (2023). https://doi.org/10.1515/ntrev-2022-0546.

[44] Z. Zhang, W. Yan, Y. Ji, A novel manganese dioxide-based drug delivery strategy via in situ coating γ-polyglutamic acid/cisplatin for intelligent anticancer therapy, J. Mater. Chem. B. 11 (2023) 667–674. https://doi.org/10.1039/D2TB01659A.

[45] S. Rakshit, P.C. Jana, T. Kamilya, Green Synthesis of Copper Nanoparticles by Using Plant Extracts and their Biomedical Applications – An Extensive Review, Current Nanomaterials. 8 (2023) 110–125. https://doi.org/10.2174/2405461507666220516092814.

[46] A.E. Alprol, A.T. Mansour, H.S. El-Beltagi, M. Ashour, Algal Extracts for Green Synthesis of Zinc Oxide Nanoparticles: Promising Approach for Algae Bioremediation, Materials. 16 (2023) 2819. https://doi.org/10.3390/ma16072819.

[47] Shahid-ul-Islam, S. Bairagi, M.R. Kamali, Review on green biomass-synthesized metallic nanoparticles and composites and their photocatalytic water purification applications:

Progress and perspectives, Chemical Engineering Journal Advances. 14 (2023) 100460. https://doi.org/10.1016/j.ceja.2023.100460.

[48] M. Thatyana, N.P. Dube, D. Kemboi, A.-L.E. Manicum, N.S. Mokgalaka-Fleischmann, J.V. Tembu, Advances in Phytonanotechnology: A Plant-Mediated Green Synthesis of Metal Nanoparticles Using Phyllanthus Plant Extracts and Their Antimicrobial and Anticancer Applications, Nanomaterials. 13 (2023) 2616. https://doi.org/10.3390/nano13192616.

[49] R. Rashid, S. Mohd Wani, S. Manzoor, F.A. Masoodi, M. Masarat Dar, Green extraction of bioactive compounds from apple pomace by ultrasound assisted natural deep eutectic solvent extraction: Optimisation, comparison and bioactivity, Food Chemistry. 398 (2023) 133871. https://doi.org/10.1016/j.foodchem.2022.133871.

[50] S. Shi, J. Cheng, N. Ahmad, W. Zhao, M. Tian, Z. Yuan, C. Li, C. Zhao, Effects of potential allelochemicals in a water extract of Abutilon theophrasti Medik. on germination and growth of Glycine max L., Triticum aestivum L., and Zea mays L, Journal of the Science of Food and Agriculture. 103 (2023) 2155–2165. https://doi.org/10.1002/jsfa.12315.

[51] N.T.T. Nguyen, L.M. Nguyen, T.T.T. Nguyen, T.T. Nguyen, D.T.C. Nguyen, T.V. Tran, Formation, antimicrobial activity, and biomedical performance of plant-based nanoparticles: a review, Environ Chem Lett. 20 (2022) 2531–2571. https://doi.org/10.1007/s10311-022-01425-w.

[52] R. Dobrucka, Synthesis of Titanium Dioxide Nanoparticles Using Echinacea purpurea Herba, Iranian Journal of Pharmaceutical Research : IJPR. 16 (2017) 756.

[53] R. Kotcherlakota, S. Nimushakavi, A. Roy, H.C. Yadavalli, S. Mukherjee, S. Haque, C.R. Patra, Biosynthesized Gold Nanoparticles: In Vivo Study of Near-Infrared Fluorescence (NIR)-Based Bio-imaging and Cell Labeling Applications, ACS Biomater. Sci. Eng. 5 (2019) 5439–5452. https://doi.org/10.1021/acsbiomaterials.9b00721.

[54] S. Muthamil Selvan, K. Vijai Anand, K. Govindaraju, S. Tamilselvan, V.G. Kumar, K.S. Subramanian, M. Kannan, K. Raja, Green synthesis of copper oxide nanoparticles and mosquito larvicidal activity against dengue, zika and chikungunya causing vector Aedes aegypti, IET Nanobiotechnology. 12 (2018) 1042–1046. https://doi.org/10.1049/iet-nbt.2018.5083.

[55] M. Rajapriya, S.A. Sharmili, R. Baskar, R. Balaji, N.S. Alharbi, S. Kadaikunnan, J.M. Khaled, K.F. Alanzi, B. Vaseeharan, Synthesis and Characterization of Zinc Oxide Nanoparticles Using Cynara scolymus Leaves: Enhanced Hemolytic, Antimicrobial, Antiproliferative, and Photocatalytic Activity, J Clust Sci. 31 (2020) 791–801. https://doi.org/10.1007/s10876-019-01686-6.

[56] M.M.S. Abdullah, A.M. Atta, H.A. Allohedan, H.Z. Alkhathlan, M. Khan, A.O. Ezzat, Green Synthesis of Hydrophobic Magnetite Nanoparticles Coated with Plant Extract and Their Application as Petroleum Oil Spill Collectors, Nanomaterials. 8 (2018) 855. https://doi.org/10.3390/nano8100855.

[57] M. Souri, V. Hoseinpour, A. Shakeri, N. Ghaemi, Optimisation of green synthesis of MnO nanoparticles via utilising response surface methodology, IET Nanobiotechnology. 12 (2018) 822–827. https://doi.org/10.1049/iet-nbt.2017.0145.

[58] S. Kannan, N.P. Subiramaniyam, M. Sathishkumar, A novel green synthesis approach for improved photocatalytic activity and antibacterial properties of zinc sulfide nanoparticles

using plant extract of Acalypha indica and Tridax procumbens, J Mater Sci: Mater Electron. 31 (2020) 9846–9859. https://doi.org/10.1007/s10854-020-03529-x.

[59] I. Parkhomenko, L. Vlasukova, F. Komarov, M. Makhavikou, O. Milchanin, A. Mudryi, E. Wendler, Radiative recombination in zinc blende ZnSe nanocrystals ion-beam synthesized in silica, J. Phys. D: Appl. Phys. 55 (2022) 205101. https://doi.org/10.1088/1361-6463/ac526c.

[60] S. Barman, J. Kumar, A.K. Das, S. Sikdar, A. Biswas, A. Srinivasan, R. Das, Comparative Study of ZnO Nanomaterials Synthesized by Green and Electrospinning Methods, Journal of Nano Research. 72 (2022) 81–93. https://doi.org/10.4028/p-vv17a6.

[61] S. Kumar, F. Fossard, G. Amiri, J.-M. Chauveau, V. Sallet, Induced structural modifications in ZnS nanowires via physical state of catalyst: Highlights of 15R crystal phase, Nano Res. 15 (2022) 377–385. https://doi.org/10.1007/s12274-021-3487-8.

[62] N. Brahim, N. Mohamed, M. Poggi, R. Chaabane, M. Haouari, H. Ben Ouada, M. Negrerie, Interaction of L-cysteine functionalized CdSe quantum dots with metallic cations and selective binding of cobalt in water probed by fluorescence, Sensors and Actuators B: Chemical. 243 (2016). https://doi.org/10.1016/j.snb.2016.12.003.

[63] S. Richard, Modélisation physique de la structure électronique, du transport et de l'ionisation par choc dans les matériaux IV-IV massifs, contraints et dans les puits quantiques, (n.d.).

[64] L. Brus, Electronic wave functions in semiconductor clusters: experiment and theory, J. Phys. Chem. 90 (1986) 2555–2560. https://doi.org/10.1021/j100403a003.

[65] A.I. Ekimov, A.A. Onushchenko, Quantum size effect in three-dimensional microscopic semiconductor crystals, Soviet Journal of Experimental and Theoretical Physics Letters. 34 (1981) 345.

[66] A. Efros, A. Efros, Interband absorption of light in a semiconductor sphere, SPIE Milestone Series. (2005). https://www.semanticscholar.org/paper/Interband-absorption-of-light-in-a-semiconductor-Efros-Efros/f9c15cd95fca148d0c0488fd0fe45476725e1cfa (accessed October 4, 2023).

[67] X. Lan, M. Chen, M.H. Hudson, V. Kamysbayev, Y. Wang, P. Guyot-Sionnest, D.V. Talapin, Quantum dot solids showing state-resolved band-like transport, Nat. Mater. 19 (2020) 323–329. https://doi.org/10.1038/s41563-019-0582-2.

[68] H. Zhao, G. Liu, S. You, F.V. A. Camargo, M. Zavelani-Rossi, X. Wang, C. Sun, B. Liu, Y. Zhang, G. Han, A. Vomiero, X. Gong, Gram-scale synthesis of carbon quantum dots with a large Stokes shift for the fabrication of eco-friendly and high-efficiency luminescent solar concentrators, Energy & Environmental Science. 14 (2021) 396–406. https://doi.org/10.1039/D0EE02235G.

[69] J. Wang, B. Zhou, J. Ma, X. Hu, Y. Xu, P. Huang, E. Song, L. Wang, W. Jiang, Enhanced Photoluminescence in CdxZn1–xS Solid Solution by Suppressing Non-Radiative Recombination for White Light-Emitting Diodes, ACS Appl. Nano Mater. 6 (2023) 61–75. https://doi.org/10.1021/acsanm.2c03632.

[70] K.-L. Wong, J.-C.G. Bünzli, P.A. Tanner, Quantum yield and brightness, Journal of Luminescence. 224 (2020) 117256. https://doi.org/10.1016/j.jlumin.2020.117256.

[71] S. Abel, J. Leta Tesfaye, R. Kiran, T. Deepak, A.U. Ruby, S. Venkatesh, R. Krishnaraj, Studying the Effect of Metallic Precursor Concentration on the Structural, Optical, and Morphological Properties of Zinc Sulfide Thin Films in Photovoltaic Cell Applications, Advances in Materials Science and Engineering. 2021 (2021) e7443664. https://doi.org/10.1155/2021/7443664.

[72] S. Ouni, A. Madaci, M. Haouari, N.B.H. Mohamed, F. Bessueille, A. Elaissari, A. Errachid, N. Jaffrezic-Renault, A Novel Conductometric Micro-sensor for Methanol Detection Based on Chitosan/Zinc Sulfide-Nanoparticles Composite Obtained by Green Synthesis, J Inorg Organomet Polym. (2023). https://doi.org/10.1007/s10904-023-02696-8.

[73] J. Liu, X. Li, J. Feng, C. Zheng, Y. Wang, A. Wang, X. Liu, ZnS Nanospheres for Optical Modulator in an Erbium-Doped Fiber Laser, Annalen Der Physik. 532 (2020) 1900454. https://doi.org/10.1002/andp.201900454.

[74] N.A. Vitshima, B. Silwana, N. Tsolekile, M.C. Matoetoe, Effect of ZnS coating on the optoelectronic properties of aqueous glutathione capped AgInS quantum dots, Journal of Alloys and Compounds. 900 (2022) 163386. https://doi.org/10.1016/j.jallcom.2021.163386.

[75] Y.-H. Won, O. Cho, T. Kim, D.-Y. Chung, T. Kim, H. Chung, H. Jang, J. Lee, D. Kim, E. Jang, Highly efficient and stable InP/ZnSe/ZnS quantum dot light-emitting diodes, Nature. 575 (2019) 634–638. https://doi.org/10.1038/s41586-019-1771-5.

[76] S. Ouni, N.B.H. Mohamed, M. Haouari, A. Elaissari, A. Errachid, N. Jaffrezic-Renault, A Novel Green Synthesis of Zinc Sulfide Nano-Adsorbents Using Artemisia Herba Alba Plant Extract for Adsorption and Photocatalysis of Methylene Blue Dye, Chemistry Africa. (2023). https://doi.org/10.1007/s42250-023-00667-7.

[77] D. Su, L. Wang, M. Li, S. Mei, X. Wei, H. Dai, Z. Hu, F. Xie, R. Guo, Highly luminescent water-soluble AgInS2/ZnS quantum dots-hydrogel composites for warm white LEDs, Journal of Alloys and Compounds. 824 (2020) 153896. https://doi.org/10.1016/j.jallcom.2020.153896.

[78] A. Kumar, M. Kumar, V. Bhatt, D. Kim, S. Mukherjee, J.-H. Yun, R.K. Choubey, ZnS microspheres-based photoconductor for UV light-sensing applications, Chemical Physics Letters. 763 (2021) 138162. https://doi.org/10.1016/j.cplett.2020.138162.

[79] H. Entezari, M. Almasi-Kashi, S. Alikhanzadeh-Arani, Comparative Study of the Electromagnetic Wave Absorption Properties in (FeNi, CoNi, and FeCo)/ZnS Nanocomposites, J Clust Sci. 33 (2022) 2689–2696. https://doi.org/10.1007/s10876-021-02186-2.

[80] D. Peng, Y. Jiang, B. Huang, Y. Du, J. Zhao, X. Zhang, R. Ma, S. Golovynskyi, B. Chen, F. Wang, A ZnS/CaZnOS Heterojunction for Efficient Mechanical-to-Optical Energy Conversion by Conduction Band Offset, Advanced Materials. 32 (2020) 1907747. https://doi.org/10.1002/adma.201907747.

[81] Q. Yu, J. Li, X. Zhang, S. Yang, P. Zhou, J. Xia, T. Deng, C. Yu, Dual-Emission ZAISe/ZnS quantum dots for Multi-level Bio-Imaging: Foam cells and atherosclerotic plaque imaging, Journal of Colloid and Interface Science. 629 (2023) 399–408. https://doi.org/10.1016/j.jcis.2022.08.134.

[82] A.R. Amani-Ghadim, F. Khodam, M.S.S. Dorraji, ZnS quantum dot intercalated layered double hydroxide semiconductors for solar water splitting and organic pollutant degradation, J. Mater. Chem. A. 7 (2019) 11408–11422. https://doi.org/10.1039/C9TA01412H.

[83] D. Borodin, I. Rahinov, P.R. Shirhatti, M. Huang, A. Kandratsenka, D.J. Auerbach, T. Zhong, H. Guo, D. Schwarzer, T.N. Kitsopoulos, A.M. Wodtke, Following the microscopic pathway to adsorption through chemisorption and physisorption wells, Science. 369 (2020) 1461–1465. https://doi.org/10.1126/science.abc9581.

[84] B.S. Rathi, P.S. Kumar, Application of adsorption process for effective removal of emerging contaminants from water and wastewater, Environmental Pollution. 280 (2021) 116995. https://doi.org/10.1016/j.envpol.2021.116995.

[85] V. Sodha, S. Shahabuddin, R. Gaur, I. Ahmad, R. Bandyopadhyay, N. Sridewi, Comprehensive Review on Zeolite-Based Nanocomposites for Treatment of Effluents from Wastewater, Nanomaterials. 12 (2022) 3199. https://doi.org/10.3390/nano12183199.

[86] J. Gopalan, A. Buthiyappan, A.A. Abdul Raman, Insight into metal-impregnated biomass based activated carbon for enhanced carbon dioxide adsorption: A review, Journal of Industrial and Engineering Chemistry. 113 (2022) 72–95. https://doi.org/10.1016/j.jiec.2022.06.026.

[87] L. Velarde, M.S. Nabavi, E. Escalera, M.-L. Antti, F. Akhtar, Adsorption of heavy metals on natural zeolites: A review, Chemosphere. 328 (2023) 138508. https://doi.org/10.1016/j.chemosphere.2023.138508.

[88] A.S. Alsaman, E.M.M. Ibrahim, A.A. Askalany, A.M. Farid, E.S. Ali, M.S. Ahmed, Composite material-based a clay for adsorption desalination and cooling applications, Chemical Engineering Research and Design. 188 (2022) 417–432. https://doi.org/10.1016/j.cherd.2022.09.017.

[89] A. Alagarsamy, S. Chandrasekaran, A. Manikandan, Green synthesis and characterization studies of biogenic zirconium oxide ($ZrO_2$) nanoparticles for adsorptive removal of methylene blue dye, Journal of Molecular Structure. 1247 (2022) 131275. https://doi.org/10.1016/j.molstruc.2021.131275.

[90] A.A.H. Abdellatif, M.A. Younis, M. Alsharidah, O. Al Rugaie, H.M. Tawfeek, Biomedical Applications of Quantum Dots: Overview, Challenges, and Clinical Potential, International Journal of Nanomedicine. 17 (2022) 1951–1970. https://doi.org/10.2147/IJN.S357980.

[91] N.C. Joshi, P. Gururani, Metal Oxide Nanoparticles and their Nanocomposite- based Materials as Photocatalysts in the Degradation of Dyes, Biointerface Research in Applied Chemistry. 12 (2022). https://doi.org/10.33263/BRIAC125.65576579.

[92] Y. Zhang, B. Zhou, H. Chen, R. Yuan, Heterogeneous photocatalytic oxidation for the removal of organophosphorus pollutants from aqueous solutions: A review, Science of The Total Environment. 856 (2023) 159048. https://doi.org/10.1016/j.scitotenv.2022.159048.

[93] S. He, Y. Chen, X. Li, L. Zeng, M. Zhu, Heterogeneous Photocatalytic Activation of Persulfate for the Removal of Organic Contaminants in Water: A Critical Review, ACS EST Eng. 2 (2022) 527–546. https://doi.org/10.1021/acsestengg.1c00330.

[94] V. Verma, M. Al-Dossari, J. Singh, M. Rawat, M.G.M. Kordy, M. Shaban, A Review on Green Synthesis of $TiO_2$ NPs: Photocatalysis and Antimicrobial Applications, Polymers. 14 (2022) 1444. https://doi.org/10.3390/polym14071444.

[95] M. Manny Porto Barros, K.J. Costa Almeida, M. Vinicius Sousa Conceição, D. Henrique Pereira, G. Botelho, Photodegradation of bisphenol A by ZnS combined with H2O2: Evaluation of photocatalytic activity, reaction parameters, and DFT calculations, Journal of Molecular Liquids. 371 (2023) 121096. https://doi.org/10.1016/j.molliq.2022.121096.

[96] Y. Sun, W. Zhang, Q. Li, H. Liu, X. Wang, Preparations and applications of zinc oxide based photocatalytic materials, Advanced Sensor and Energy Materials. 2 (2023) 100069. https://doi.org/10.1016/j.asems.2023.100069.

[97] Z. Chen, D. Yao, C. Chu, S. Mao, Photocatalytic $H_2O_2$ production Systems: Design strategies and environmental applications, Chemical Engineering Journal. 451 (2023) 138489. https://doi.org/10.1016/j.cej.2022.138489.

[98] T. Dodevska, D. Hadzhiev, I. Shterev, A Review on Electrochemical Microsensors for Ascorbic Acid Detection: Clinical, Pharmaceutical, and Food Safety Applications, Micromachines. 14 (2023) 41. https://doi.org/10.3390/mi14010041.

[99] K.G. Krishna, S. Parne, N. Pothukanuri, V. Kathirvelu, S. Gandi, D. Joshi, Nanostructured metal oxide semiconductor-based gas sensors: A comprehensive review, Sensors and Actuators A: Physical. 341 (2022) 113578. https://doi.org/10.1016/j.sna.2022.113578.

[100] S.-X.L. Luo, T.M. Swager, Chemiresistive sensing with functionalized carbon nanotubes, Nat Rev Methods Primers. 3 (2023) 1–20. https://doi.org/10.1038/s43586-023-00255-6.

[101] A. Madaci, G. Raffin, M. Hangouet, C. Pages, C. Jose, M. Martin, H. Ferkous, A. Bouzid, J. Bausells, A. Alcacer, A. Errachid, N. Jaffrezic-Renault, A microconductometric ethanol sensor prepared through encapsulation of alcohol dehydrogenase in chitosan: application to the determination of alcoholic content in headspace above beverages, J Mater Sci: Mater Electron. 32 (2021) 17752–17763. https://doi.org/10.1007/s10854-021-06311-9.

[102] I. Musa, G. Raffin, M. Hangouet, M. Martin, A. Alcacer, N. Zine, F. Bellagambi, N. Jaffrezic-Renault, A. Errachid, Development of a Chitosan/Nickel Phthalocyanine Composite based Conductometric Micro-sensor for Methanol Detection, Electroanalysis. n/a (n.d.). https://doi.org/10.1002/elan.202100707.

# *Chapitre II*

## *High impact of thiol capped ZnS nanocrystals on the degradation of single and binary aqueous solutions of industrial azo dyes under sunlight*

## Résumé

Des nanocristaux de sulfure de zinc (ZnS) ont été préparés en utilisant une voie colloïdale aqueuse avec l'acide thioglycolique (TGA) comme stabilisateur. Ces nanocristaux de ZnS-TGA ont été utilisés comme alternative peu coûteuse et respectueuse de l'environnement pour la photodégradation du bleu de méthylène (MB) et de orange de méthylène (MO) à partir de solutions aqueuses utilisant l'irradiation solaire. Les propriétés structurales et optiques des nanocristaux ont été déterminées par diffraction des rayons X, spectroscopie infrarouge de transformation de Fourier, microscopie électronique de transmission, spectroscopie UV-visible et photoluminescence. Les résultats ont montré un décalage bleu de la bande d'absorbance et des valeurs d'écart de bande d'énergie plus élevées que celle du ZnS massif, ce qui était en accord avec l'effet de confinement quantique. La diffraction des rayons X a confirmé la formation d'une phase cubique de ZnS-TGA contenant également une phase hexagonale légère. La taille moyenne calculée des nanocristaux de ZnS par la relation de Debye Scherrer était de 3,5 nm. Les résultats de caractérisation ont montré la fixation du TGA sur les nanocristaux de ZnS via des fonctionnalités soufrées et carboxyliques sur la surface du nanocatalyseur. Les spectres de photoluminescence obtenus sous la longueur d'onde d'excitation à 325 nm ont montré trois bandes d'émission (416, 441 et 484 nm), qui étaient principalement liées au bord de la bande et aux émissions activées par défaut. L'activité photocatalytique des nanocristaux de ZnS-TGA sous irradiation solaire pour dégrader les colorants MB et MO testés et leur mélange dans des solutions aqueuses a été évaluée. L'efficacité élevée de dégradation du colorant a été obtenue à très court terme (27 min) et cette performance a été attribuée à la charge de surface négative, à la surface, aux défauts de surface et à la dispersion élevée des nanocristaux ZnS-TGA sur le milieu aquatique. Dans l'ensemble, cette étude démontre que ces nanocristaux pourraient être utilisés comme nanocatalyseurs à faible coût pour la dégradation des colorants organiques dans le traitement des eaux usées.

# *High impact of thiol capped ZnS nanocrystals on the degradation of single and binary aqueous solutions of industrial azo dyes under sunlight*


## Abstract

Sulfur zinc (ZnS) nanocrystals were prepared using an aqueous colloidal route with thioglycolic acid (TGA) as a stabilizer. These ZnS-TGA nanocrystals were used as a low-cost and environmental friendly alternative for the photodegradation of methylene blue (MB) and methyl orange (MO) from aqueous solutions using sunlight irradiation. Structural and optical properties of nanocrystals were determined via X-ray diffraction, Fourier transform infrared spectroscopy, Transmission electron microscopic, UV–Visible and photoluminescence spectroscopy. Results showed a blue shift of absorbance band and higher energy band gap values than bulk ZnS materials, which was in agreement with the quantum confinement effect. X-ray diffraction confirmed the formation of cubic phase of ZnS-TGA containing also a slight wurtzite phase. Calculated average size of ZnS nanocrystals by the Debye Scherrer relation was 3.5 nm. Characterization results showed the fixation of TGA on ZnS-NCs via sulphur and carboxylic functionalities on catalyst surface. Photoluminescence spectra obtained under excitation wavelength at 325 nm showed three emission bands (416, 441 and 484 nm), which were mainly related to band edge and defect-activated emissions. The photocatalytic activity of ZnS-TGA nanocrystals under sunlight irradiation to degrade tested MB and MO dyes and their mixture in aqueous solutions was evaluated. High dye degradation efficiency was achieved at a very short time (27 min) and this performance was attributed to the negative surface charge, surface area, surface defects and high dispersion of ZnS-TGA nanocrystals on the aquatic medium. Overall, this study demonstrates that these nanocrystals could be employed as low-cost nanocatalyst for the degradation of organic dyes in wastewater treatment.



**Keywords**: ZnS-TGA ; Nanocrystals ; Photocatalysis ; Binary dye ; Degradation.


## I. Introduction

The development of nanotechnology has been one of the main areas of research in recent decades. Various applications in different sectors are witnesses of these advances and they include medical imaging [1], lighting [2], sensors [3], biosensors [4], batteries [5], photovoltaic conversion [6] and photocatalysis [7] for the degradation of persistent pollutants. Note that these applications are supported by the development of new nanomaterials that are both scientifically and technologically interesting. In particular, II-VI semiconductor nanocrystals (also known as

quantum dots) are an outstanding example. They are colloidal nanoparticles formed from a few hundred to thousand atoms that emit fluorescence after being excited by a visible or UV light source [8]. Some optical and electronic properties of these materials (e.g., fine emission spectra, good quantum photoluminescence yields) are exceptional and directly correlated with their size and/or composition [9,10]. Indeed, the reduced size of these nanostructures induces the spatial confinement of charge carriers leading to the discretization of energy levels as well as to the widening of the energy bandgap of the material, which is the effect of quantum confinement. For instance, cadmium selenide nanocrystals (CdSe) can emit across the entire visible spectrum (approximately 450–700 nm) when their size ranges from 2 to 10 nm [11]. These nanocrystals are stabilized by a layer of organic thiol ligands such as MPA [12] and GSH [13], which are adsorbed to their surface to ensure the colloidal stability and passivation of surface defects. Also, they are usually capped by polyvinyl alcohol (PVA) [14], chitosan [15]and Schiff base [16]. Other coating can be used such as the matrices as of silica [17]. Consequently, this organic layer can improve dramatically the quantum fluorescence efficiency of the inorganic core. However, it is important to synthesize nanocrystals with very low toxicity such as ZnO [18], ZnSe [19], TiO2 [20] and ZnS [21–24], which should have all the characteristics required for their integration in various applications and especially in photocatalytic activities. Environment pollution problems are relevant worldwide and require the development of effective treatment processes for removing/ degrading pollutants with a better performance than the current technologies especially for those applied in water treatment [25–27]. One of the main water pollution sources is the improper disposal of dyes utilized in textile fibers, metal coloring and painting. These chemicals are miscible in water even at low concentrations and they contribute to pollution problems related to the generation of a considerable amount of wastewater containing residual dye molecules [28]. These dyes can be toxic and carcinogenic and, hence, there is a need to find techniques to degrade/remove these hazardous pollutants. One of these new methods relies on the ecological process of advanced oxidation (PAO) that involves powerful oxidizing species to achieve the complete mineralization of organic pollutants into $CO_2$ and $H_2O$ or at least their transformation into biodegradable intermediates. Photocatalysis is the process of irradiating a semiconductor material either naturally or by a flux of photons. An electron is thus photo-released by making an energy transition from the valence band (BV) to the conduction band (BC). This transition generates a pair (e– /h+) in the material. Electron-hole pairs diffuse towards the catalyst surface where the interaction with water molecules would generate highly oxidizing species of peroxide ($O_2^{*-}$) and hydroxyl radical ($OH^*$), which are responsible for degrading organic molecules adsorbed on the photocatalyst surface. This

treatment method is effective and green for resolving the pollution caused by a variety of water pollutants including dye molecules [29]. However, the small size of these ultrafine nanoparticles restricts their application due to the difficulty of their recuperation from the fluid. One alternative to overcome this drawback is the use of a supporting porous material such as zeolites. Indeed, zeolites have been studied as support for metal nanoparticles [30–33]. However, this supporting structure could be non-convenient for semiconductor nanoparticles due to their small pores, which do not exceed 2 nm in diameter. Therefore, alternative supports should be studied and tested for this purpose. On the other hand, methylene orange (MO) and methylene blue (MB) are widely employed in several industrial applications [34–37]. MO is an anionic dye that belongs to the azo group and is characterized by an absorption band at 465 nm due to the group N=N that is responsible of the orange coloring [38]. MB is a cationic dye with a C-$S^{+}$=C functional group that is characterized by an absorption peak at 665 nm [39]. These dye molecules are highly soluble in water with a low vapor pressure and, therefore, they can be utilized as model compounds to test and evaluate the performance of new photocatalysts. Among the common nanoparticles used to degrade these toxic molecules, zinc sulfide (ZnS) NCs are an interesting alternative due to their high stability, non-toxicity and abundance in nature. In this work, TGA-capped ZnS nanocrystals were synthetized using a simple method at room temperature and their photocatalytic activity was analyzed via the MO and MB degradation. These nanocrystals were characterized by Fourier transform infrared spectroscopy (FTIR), X-ray diffraction (XRD), Transmission electron microscopic (TEM), UV–visible and photoluminescence spectroscopy (PL). MO and MB degradation with ZnS-TGA nanocrystals was assessed at different operating conditions under sunlight irradiation.

# II. Experimental section

## II.1 Materials

All chemicals were analytical grade and obtained from commercial sources. Zinc acetate dihydrate (Zn[CH3COO]2·2H2O), thioglycolic acid (HSCH2COOH), sodium hydroxide (NaOH) and sodium sulfide (Na2S) were purchased from Sigma-Aldrich. These chemicals were used without any purification. High-purity water was employed in colloidal synthesis.

## II.2 Preparation of TGA-capped ZnS nanocrystals

The synthesis of NCs was done by colloidal wet chemical route as reported in [40] and this procedure is illustrated in ***Figure II.1***. Thioglycolic acid (TGA) was used as stabilizer for preparing the ZnS aqueous solution. $Zn^{2+}$/$S^{2-}$/TGA molar ratio of 1/0.4/2.5 was utilized due to

the stoichiometric requirement, which generated proper coverage and total saturation of the dangling bonds at NCs surface with thiol group. The experimental synthesis protocol is briefly described as follows. A solution containing 2 mmol of $Zn[OOCCH_3]_2{\cdot}2H_2O$ and 5 mmol of the capping agent (TGA) was prepared with 100 mL of distilled water in a three necked flask and NaOH (1 M) was added dropwise to this solution to adjust the pH to 11. The mixture was then agitated and degassed in the presence of $N_2$ for 30 min. In a second step, 35 mL of $Na_2S$ (0.8 mmol) were added to the solution containing Zn-TGA complexes at room temperature under stirring. This temperature was optimized through previous experiments. The mixture was then heated under $N_2$ reflux at 100°C for 3 h to obtain TGA-capped ZnS NCs. This temperature was optimized after previous experiments. Finally, the mixture was cooled in order to stop the growth of NCs. The final solution was concentrated down using an evaporator and then purified by precipitation and washing with ethanol, and the samples were stored in vacuum at room temperature.

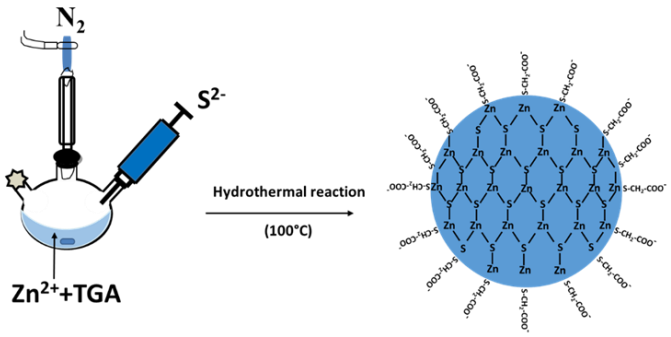


***Figure II.1***: Synthesis of TGA-capped ZnS nanocrystals

## II.3 Photocatalyst characterization

Several techniques were applied for the structural and optical characterization of nanophotocatalyst: XRD, FTIR, UV–visible absorption and PL.XRD measurements were performed using a Philips X′ Pert PRO MPD diffractometer equipped with a CuKα radiation source (λ = 1542 Å). TEM images were obtained using a FEI Tecnai G2 electron microscope operating at an accelerating voltage of 200 kV and equipped with Energy Dispersive X-ray (EDX) system for element chemical analysis. NCs size and size-distribution data were obtained from TEM images by measuring at least 100 randomly selected NCs using image processing program (Image J, version 1.50). Samples were studied by placing a drop of aqueous suspension of particles onto a carbon film supported copper grid. FTIR spectra were recorded using a Perkin Elmer version 5.3 spectrophotometer at room temperature in the spectral range of 400–

4000 cm− 1 using KBr pellet disks. The absorption spectra were registered in the wavelength range of 200–800 nm at room temperature using a SPECORD 210 Plus spectrophotometer with a quartz cuvette. PL spectroscopy was applied to analyze the emission properties of the ZnS using a helium-cadmium laser operating at 325 nm as the exciting source. The sample was placed inside a close-cycled He cryostat where the temperature can be controlled between 80 and 300 K.

### II.4 Evaluation of photocatalytic activity

The photocatalytic activity of TGA-capped ZnS NCs was assessed via the photodegradation of MO and MB molecules with different initial dye concentrations. The photocatalytic experiments were carried out at 300 K and pH 7. Prior to the photocatalytic experiments, the adsorption of MO, MB and MO/MB on TGA-capped ZnS NCs was carried out by mixing 20 mL of aqueous solutions of dyes with 20 mg of the photocatalyst. Before sunlight irradiation, the suspensions were magnetically stirred for 120 min to allow adsorption-desorption equilibrium between dyes molecules and NCs. Then, the mixture was submitted to sunlight irradiation between 11 am and 2 pm to evaluate the dye degradation. According to Beer–Lambert law, the degradation efficiency was evaluated by measuring the optical absorption at the maximum absorption wavelengths of MB and MO at 664 and 465 nm, respectively [12]. The degradation percentage and rate were calculated using the following equations [41,42]:

$$\eta\ (\%) = \frac{(A_0 - A_t)}{A_0} x100 = \frac{(C_0 - C_t)}{C_0} x100 \quad (1)$$

$$kt = \mathrm{Ln}\frac{A_0}{A_t} = Ln\frac{C_0}{C_t} \leftrightarrow A_t = A_0 e^{-kt} \quad (2)$$

where $A_0$ is the initial absorbance of the initial dye concentration $C_0$ and $A_t$ is the absorbance for the final dye concentration $C_t$ after irradiation for an interval of time t. Note that K ($min^{-1}$) is the calculated first-order rate constant of the photodegradation reaction.

## III. Results and discussion

### III.1 Photocatalyst characterization

FTIR spectra of TGA-capped ZnS NCs are shown in ***Figure II.2***. It was observed the disappearance of thiol group band that is generally observed between 2560 and 2590 $cm^{-1}$, which indicated the break of SH bond and the fixation of thiol molecules on NCs surface. The fixation of TGA on ZnS NCs was due to the strong interaction between the sulfur electron pair and zinc atoms on the NCs surface [40]. The absorption spectrum of ZnS-TGA given in Fig. 2 shows an absorption band at 563 $cm^{-1}$ that was attributed to the Zn–S stretching vibrations

[43]. Also, this spectrum contained absorption bands at 780,850,1429 and 1508 $cm^{-1}$ corresponding to strain vibration of the bonds C–S, C–H, $COO^-$ and C=O, respectively. A wide band around 3340 $cm^{-1}$ was identified and associated to the O–H elongation vibration of TGA ligand functional group [44]. These results indicated that TGA molecules were chemisorbed on the surface of TGA capped ZnS NCs.

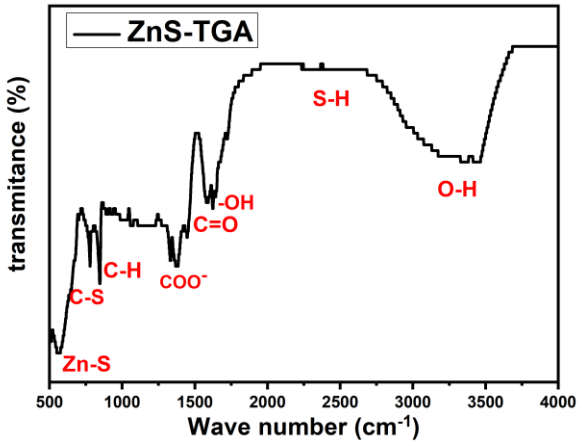


***Figure II.2***: Fourier transformed infrared spectra of TGA-capped ZnS NCs

The crystalline structure and average size of ZnS-TGA NCs were analyzed via XRD results. ***Figure II.3*** shows the XRD diffraction pattern of NCs obtained as powder. For the phase identification, the baseline data were obtained from the powder diffraction pattern JCPDS (80-0020 and 80-0007) for ZnS, which corresponded to the two structures of zinc blende (ZB) and wurtzite (WZ), respectively. XRD pattern of ZnS-TGA exhibited diffraction peaks at 2θ = 28.95◦, 33.76◦, 47.58 and 55.27◦, which were attributed respectively to diffraction planes (111), (200), (220) and (311) of ZB phase. However, the diffraction peak at 31.08◦ corresponded to the (101) crystalline plane of wurtzite ZnS. Hence, a hexagonal phase in the final sample may be present although its contribution was not significant. This structural anomaly make the distinction between the cubic and hexagonal structure very difficult. Besides, the synthetized TGA-capped ZnS contained most cubic crystalline phases and a small portion of hexagonal crystalline phase. Even so, it is important to note that the intensity of the peak (111) suggested that this direction was the most preferred and confirmed that the structure of ZnS-TGA NCs was almost cubic. The diffractogram was adjusted by a Gaussian profile to calculate FWHM and to estimate NCs size using the Debye-Scherrer formula [45].

$$\mathbf{D} = \frac{K\lambda}{\beta \cos(\theta)} \qquad (3)$$

where D is the average crystallite size (nm), K is the shape factor (0.9),λ is the wavelength of X-ray (1.5402 Å) Cu Kα radiation, β is the measured full width at half maximum for each peak diffraction and θ is the Bragg diffraction angle, respectively. The calculated average size of ZnS-TGA NCs with different crystallographic planes was D = 7.15 ± 0.1nm and the lattice parameters were a = 5.4˚A (cubic) and a = 3.8˚A, c = 6.9˚A (hexagonal). These values confirmed that the size of ZnS-TGA NCs was in the nanometric domain. Since Scherrer formula takes into account only the size effects coming from the diffraction planes, it provided a lower limit for the NCs size [46]. This is due to the fact that the size calculation using Scherrer formula neglects the lattice strain [47]. In other words, the slight shift in XRD pattern positions was an evidence for the existence of strain along the most intense peak corresponding to (111) plane. Generally, the strain may be generated by the lattice imperfection and the presence of defects and vacancies and the size confinement when the size of the particle is very small [11].

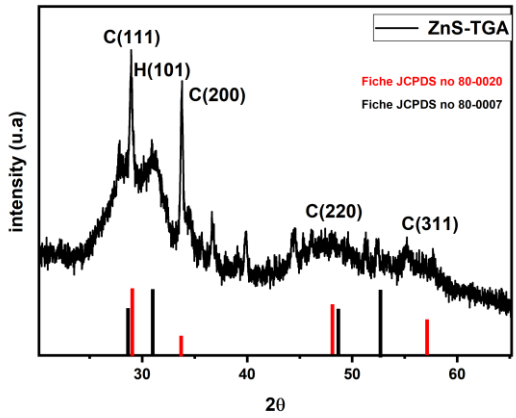


***Figure II.3***: *X-ray diffraction (XRD) pattern of TGA-capped ZnS NCs*

***Figure II.4a*** shows the TEM images of the sample and the corresponding size distribution histogram. TGA-capped ZnS NCs exhibited a spherical shape and they were agglomerated due to the insufficient of ligand amount to cover all ZnS NCs. These aggregates could be due to high QD concentrations (most likely during the solvent evaporation process at TEM analysis). The histogram of NCs size distribution showed that the average crystal size was 5.91 ± 0.5nm. This result was consistent with DRX measurements. The d-spacing determined from digital micrograph for ZnS was 0.36 nm, which was close to the spacing of (111) diffraction plane of ZB-ZnS. Comparing the values calculated by Bragg's law, it was evident that the growth of ZnS-TGA occurred preferentially along the direction [111]. NCs elemental composition was determined by EDX and the results are shown in ***Figure II.4b*** and indicated that Zn and S were

the major elemental components. The presence of Si was related to the signal from the detector. Copper, oxygen and carbon were associated to TEM grid and TGA stabilizer. These results confirmed that ZnS NCs were almost stabilized by TGA, which was in agreement with the binding between TGA and ZnS NCs identified in FTIR analysis.

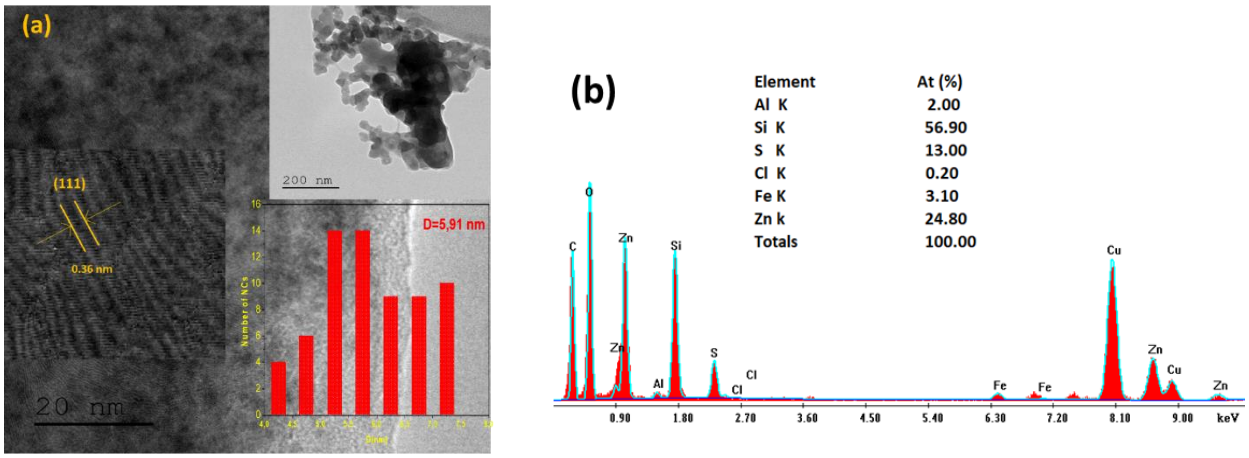


***Figure II.4***: (a) TEM images of ZnS-TGA nanocrystals with an inset showing the 0.36 nm lattice spacing that corresponded to the (111) plane and (b) EDX results.

UV–Visible absorption spectra of the dispersed TGA-capped ZnS QDs solution (***Figure II.5a***) revealed an absorption band at 307 nm, which was associated to the first electronic transition $1S_e$-$1S_h$.The band gap energy depends on the NCs size [48] and can be estimated as an additional confirmation of the size measured by TEM. In comparison with bulk ZnS (344 nm), there was a blue shift, which was due to the quantum confinement of charge carriers. Optical absorption measurements allowed to determinate the band gap energy (Eg) of ZnS NCs by using the TAUC relation [49]:

$$\alpha h\nu = A\,(h\nu - Eg)^n \qquad (4)$$

where α is the absorption coefficient, A is a constant, hν is the photon energy, Eg is the optical gap of NCs and n is a constant (n = 1/2 for direct semiconductors). The optical gap of ZnS-TGA NCs was determined by extrapolating the function graph $(\alpha h\nu)^2$ to the value α = 0. The intersection with the x-axis provided the value of optical gap energy (***Figure II.5b***). The estimated

value of band gap energy was 3.75 eV. It was clear that the gap energy of these nanocrystals shifted towards the blue as compared to the bulk ZnS (Eg = 3.6 eV). This increment of gap

energy was due to the very small size of NCs, which induced a quantum confinement effect (QCE) [49]. To estimate the ZnS-NCs size, the simplified equation of Brus was employed [50]:

$$\mathbf{r}\,(E_g^{NC}) = \frac{0.32-2.9\sqrt{E-3.49}}{2(3.50-E_g^{NC})} \qquad (5)$$

where $E_g^{NC}$ and r are the energy band gap of nanocrystals and the nanocrystals radius (nm), respectively. The results confirmed that the increment in the value of optical gap in relation with the bulk leaded to a quantum confinement and a very small size of NCs (r = 2.30 nm). The difference between the sizes found by absorption spectroscopy and XRD can be explained by considering that this value was based on the effective mass approximation under the assumption that the NCs geometry was spherical. However, XRD measurements in polydisperse systems were controlled by the contribution of the largest particles [51]. It can also be noted that this difference could be due to the fact that XRD spectra were obtained for powdered NCs, while the absorption measurements were done for NCs in solution.

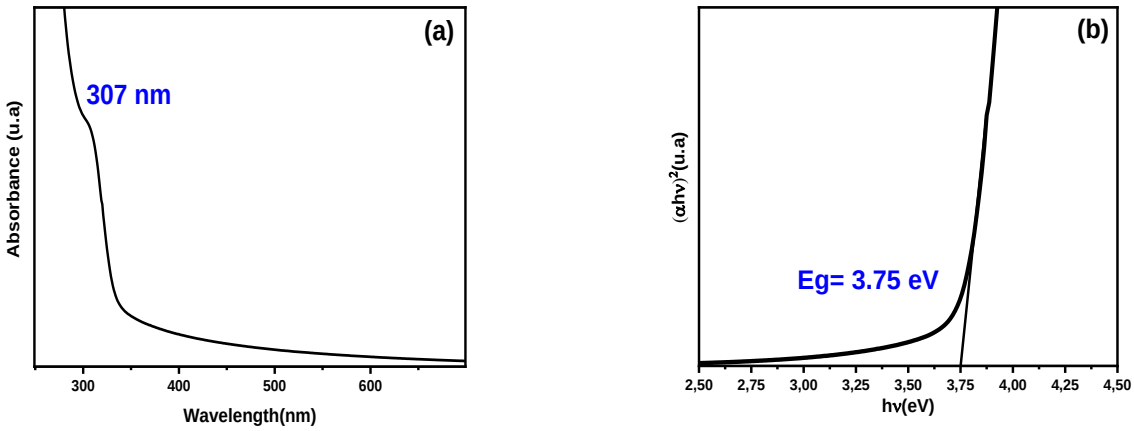


***Figure II.5***: (a) Optical absorption spectrum of ZnS-TGA nanocrystals and (b) graphical method for the calculation of their optical gap energy

***Figure II.6*** shows the PL spectra of the ZnS-TGA NCs in aqueous solution sing TGA as the ligand and excited with the 325 nm line of a helium cadmium laser at temperatures from 80 to 300 K. ***Figure II.7*** displays the energy position of PL peak as a function of the measurement temperature. At all temperatures, the emission spectra of ZnS NCs contained a large band located at 416 nm (2.98 eV) (band edge "BE") and two low energy broad bands located at 2.81 eV (441 nm) (Defect 1) and 2.56 eV (484 nm) (Defect 2). The PL spectra of these NCs were similar at low temperature to those observed at room temperature. It was clear that the excitonic

state of ZnS-TGA showed significant blue shifts due to temperature decrement, and the PL bands became narrower whereas their intensity increased. Indeed, the full width at half maximum (FWHM) of the band edge and defects emission increased with the temperature but with a slight change of their maximum position. By using Varshni model [52], the very weak blue shifts of PL peak position were estimated to be 0.4 meV as the temperature decreased from 300 to 10 K. This trend was also observed in the range of 10–300 K for various semiconductors and reflected the shrink of energy band gap with temperature increments due to the thermal expansion of the lattice and exciton-phonon coupling [53]. Both effects resulted in the broadening of the band gap and in turn a blue shift of the excitonic emission, while the energy position of the (Defect 1)D1 and (Defect 2) D2 bands changed slightly when temperature increased. This temperature dependence of these bands described a thermal process probably due to the NCs size distribution and that the impurity levels (traps state or surface defects) into the forbidden band gap were strongly attached to the ZnS-TGA lattice [54]. On the other hand, the intensities of both trapping and excitonic emission increased especially at lower temperature and this effect was attributed to the suppression of phonon-coupled thermal quenching and different sensitivities to temperature between trapping and excitonic state in NCs [55,56]. At higher temperatures, the phonon coupling was stronger. Therefore, phonon absorption started to play a role in assisting the non-radiative recombination probability of electrons and holes as shown in the decrease of PL intensity [57].

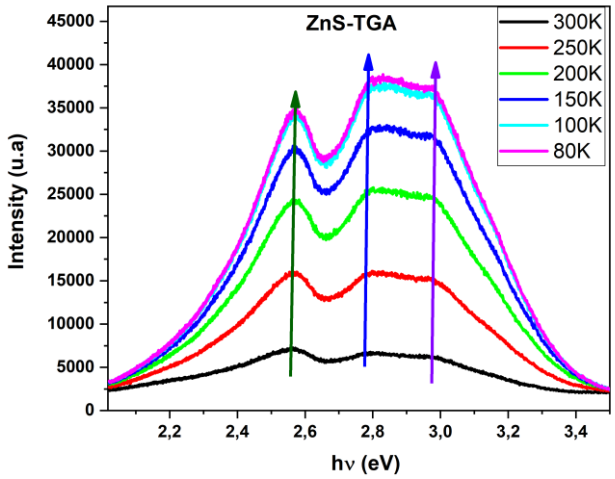


***Figure II.6***: PL spectra as a function of temperature for ZnS-TGA nanocrystals.

In order to explain the temperature behavior of excitonic emission of ZnS-TGA NCs, ***Figure II.8*** shows a proposal of an emission mechanism for the possible radiative and non-radiative transitions of the charge carriers. The blue emissions arise from the band edge emission and/or

exciton recombination. Based on a previous study on defects in ZnS NCs, the sulfur vacancies and interstitial zinc atoms were equivalent to localized donor states, while zinc vacancies and interstitial sulfur atoms lead to acceptor states [54]. In the present study, the synthesized NCs contained an excess of zinc or sulfur deficiency following a molar ratio to Zn/S ≥ 2. Indeed, the defect-related emissions were attributed to a transition from either interstitial zinc atom ($I_{Zn}$) or sulfur vacancy (Vs) to the valence band [54,58]. The emission between 500 and 700 nm was assigned to defects trapped on the NCs surface, which arise from surface non-stoichiometry and unsaturated bonds [54,59]. These results indicated that the photoluminescence properties of ZnS-TGA strongly depended on the preparation method.

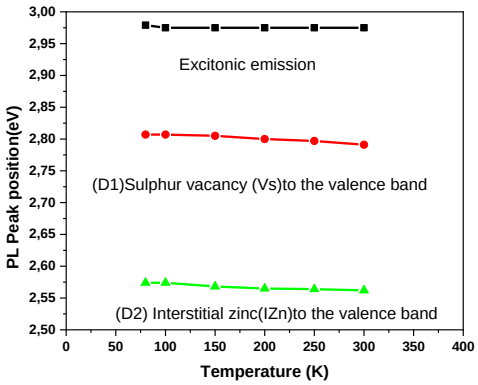


***Figure II.7***: PL peak position as a function of temperature for both D1 and D2 defects.

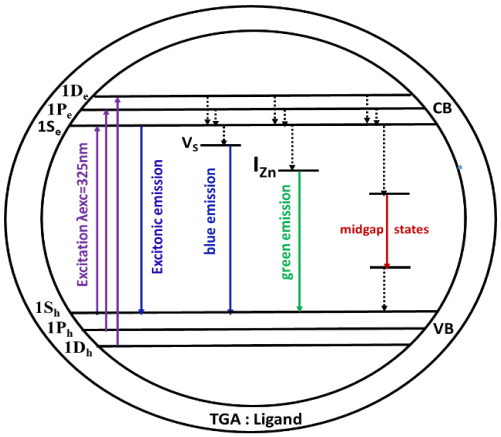


***Figure II.8***: Emission mechanism of TGA-capped ZnS nanocrystals.

The fluorescence quantum yield (RQ) of ZnS-TGA was estimated with respect to the organic dye Rhodamine 6G (RG6) with a known quantum yield (RQ = 0.94 in water) using the Eq. (6) proposed by Würth [60]:

$$\Phi_{QDs} = \Phi_{ref} \frac{A_{Ref}}{A_{QDs}} \frac{F_{QDs}}{F_{REF}} \frac{\boldsymbol{n_{QDs}}^2}{\boldsymbol{n_{REF}}^2} \quad (6)$$

where the indices $R_{ef}$ and $\Phi_{QDs}$ indicate the reference fluorophore (R6G for this study) and quantum's dots, respectively, $A_{QDs}$ is the absorbance of the sample at the excitation wavelength, $F_{QDs}$ is the area under the fluorescence curve, $n_{QDs}$ is the solvent index used to obtain the spectra and $\Phi_{ref}$ is the quantum yield of the reference fluorophore. UV absorption and fluorescence spectra of RG6 and ZnS-TGA QDs in water were recorded using the same conditions (***Figure II.9***). The quantum yield of ZnS-TGA QDs was 13.96%. This RQ decrement was usually associated to the presence of defects on the NCs surface because the trapping of charge carriers behaves as luminescence quenchers and tends to favor the nonradiative decay [61].

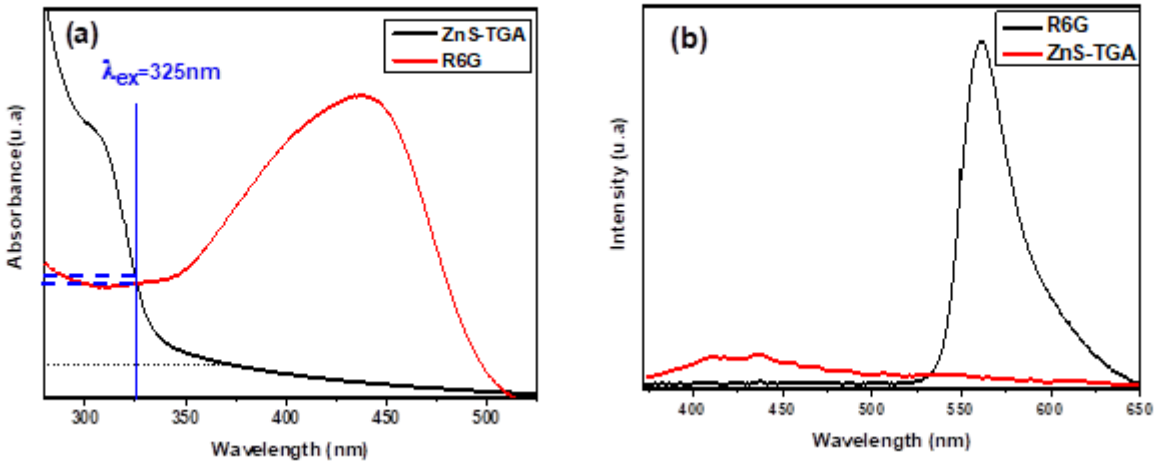


***Figure II.9***: (a) Absorption spectra and (b) emission spectra of ZnS-TGA nanocrystals and RG6.

### III.2 Photocatalytic activity in single and binary aqueous solutions of dye molecules

Because of ecological problems, industries seek the most efficient solutions with the lowest costs. Photocatalysis using natural sunlight irradiation is an alternative to meet this necessity. The application of solar power can be a viable method for textile wastewater treatment due to its eco-friendly and cost-effective performance where 96% of textile industrial wastewater can be photodegraded during April–June (which is the annual peak of summer period) [62]. According to the World Meteorological Organization, the outer atmosphere of the planet receives approximately 1367 W/m2 of insolation thus causing that sunlight can be considered as a renewable, free and clean energy source [62]. Sunlight can be exploited for the irradiation of semiconductors with the aim of performing the photodegradation of pollutants thus

contributing to reduce the cost of water treatment methods and the environmental pollution in comparison to UV lamps.

On the other hand, the available photocatalysts cannot be effective to degrade all types of dye molecules, which can also be mixed in wastewaters. This is because the textile sector and other industries can utilize different dyes in their processes. Therefore, it is important to test the performance of photocatalysts for different dye molecules and mixtures of them. MB and MO were selected in this study because they are representative molecules of acidic (anionic) and basic (cationic) dyes. The study of these molecules offered a better understanding of ionic interaction and its influence on photocatalytic degradation efficiency. In addition, the primary colors are red, blue and yellow. Therefore, MB dye (blue color) and MO dye (yellow color) are representative of these conditions. Note that if the prepared materials were able to degrade a mixture of these dyes, then it can be expected that this material will be suitable for the degradation of other dye molecules. The photocatalytic performance of TGA-capped ZnS NCs was evaluated by decolorizing aqueous solutions of MO and MB with different initials concentrations under sunlight irradiation at the same experimental conditions. Also, further investigation of photocatalytic degradation activity was conducted using a MB/MO mixture. In the absence of these NCs, a marginal degradation was observed (approximately 10%) due to the OH* radicals initiated from water or due to self-sensitization light of dye molecules [63]. This result indicated that the dye degradation was practically negligible without photocatalyst under sunlight irradiation.

***Figure II.10*** illustrates the absorption spectra of MO as a function of the irradiation time using ZnS-TGA NCs. Four different dye concentrations were utilized to evaluate the degradation performance of ZnS-TGA NCs. It was observed a high reduction in the absorption of the dye(s) solution due to the break of the (–N=N–) bond thus indicating that the aromatic compounds were attacked by hydroxyl radicals and formed intermediate compounds [64]. As a result, MO dye concentration decreased in the presence of ZnS-TGA NCs and sunlight irradiation until the full decolorization of the initial solution revealing that MO molecules were completely degraded.

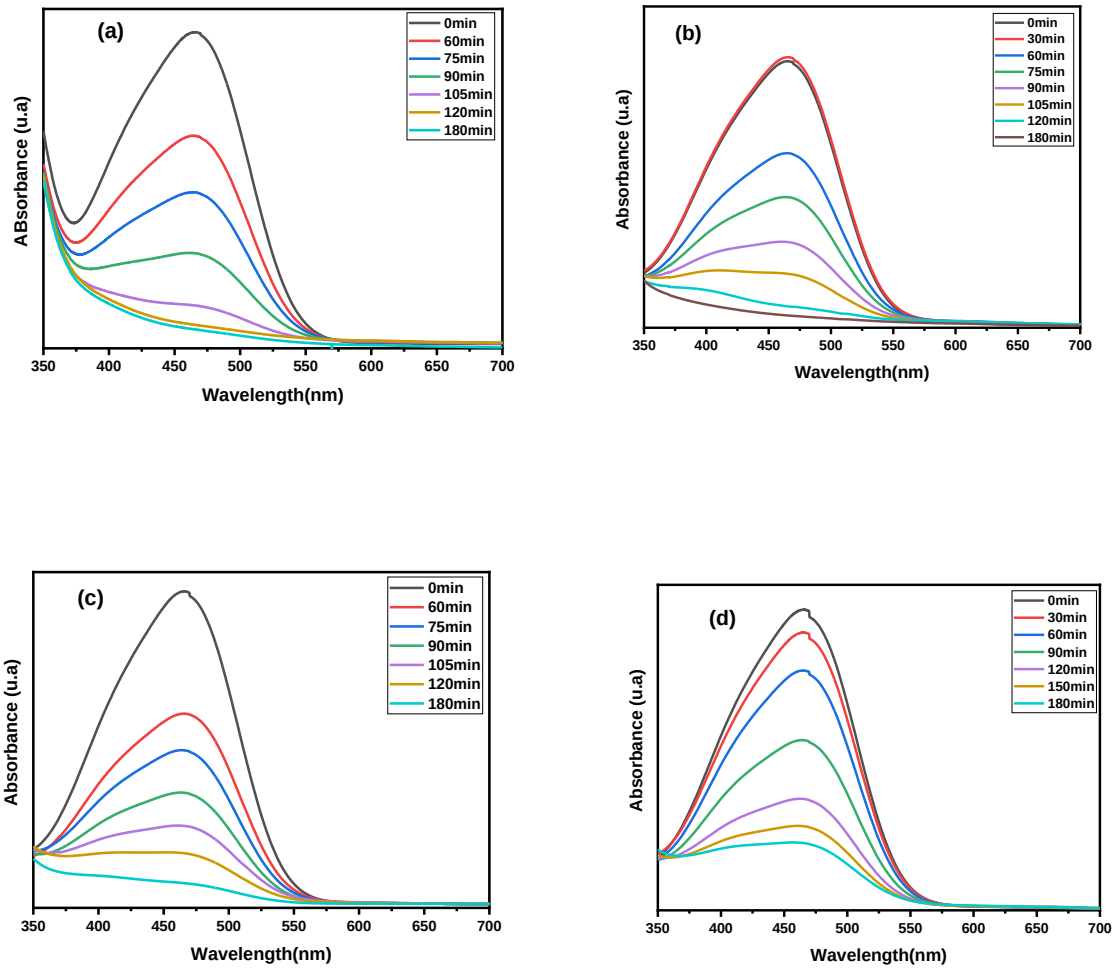


***Figure II.10***: UV–visible absorption spectra for the MO decolorization using ZnS-TGA nanocrystals under sunlight irradiation. Initial MO concentration: (a) 10 mg/L, (b) 15, (c) 20 and (d) 25 mg/L.

The effect of the initial MO concentration on the degradation efficiency is reported in ***Table II.1***. Decolorization efficiencies greater than 94% were obtained for all concentrations except for the dye concentration equal to 25 mg/L (79.85%). These efficiencies can be associated to the small size of TGA molecules used as a stabilizer in addition to the specific surface of NCs that contributed with more adsorption sites. Therefore, ZnS-TGA NCs exhibited strong photocatalytic activity for the removal of MO dye. This result could be explained by the large band gap energy of ZnS, which caused a higher redox potential of e-h pairs and, consequently, a higher photocatalytic performance [65]. As expected, the dye degradation decreased with the increment of initial MO concentration. The principal reason for this behavior was that the generation of $O_2^{*-}$ and $OH^*$ radicals on the photocatalyst surface was reduced because active sites were covered by dye molecules at high dye concentrations. Another possible explanation was the screening of sunlight by the dye itself leading to a reduction in the light absorption

ability of the catalyst [66]. Indeed, a significant amount of sunlight can be absorbed by dye molecules at high concentrations rather than ZnS-TGA, which reduced the efficiency of the catalytic reaction as the concentrations of $OH^*$ and $O_2^{*-}$ species decreased [67]. The degradation rate constant of MO dye was calculated using Langmuir-Hinshelwood (L-H) kinetics model.

***Table II.1***: Efficiencies for the degradation of MO using ZnS-TGA nanocrystals under sunlight irradiation.

| MO concentration (mg/L) | Degradation efficiency (%) |
|---|---|
| 10 | 99.04 |
| 15 | 98.18 |
| 20 | 94.32 |
| 25 | 79.85 |

Photodegradation plots of ln (A0/A) vs. the time t for MO are shown in Fig. 11(a) where K is the apparent reaction rate constant. ***Figure II.11(b)*** shows that the use of low MO concentration (e.g., 10 mg/L) generated the best degradation constant K (0.025 $min^{-1}$). Increments of dye concentration reduced the degradation efficiency where a degradation rate of 0.009 $min^{-1}$ was estimated for the highest concentration. It can be concluded that the initial MO concentration had a significant effect on the degradation rates. These results confirmed that TGA-capped ZnS NCs exhibited strong photocatalytic activity for the removal of MO dye.

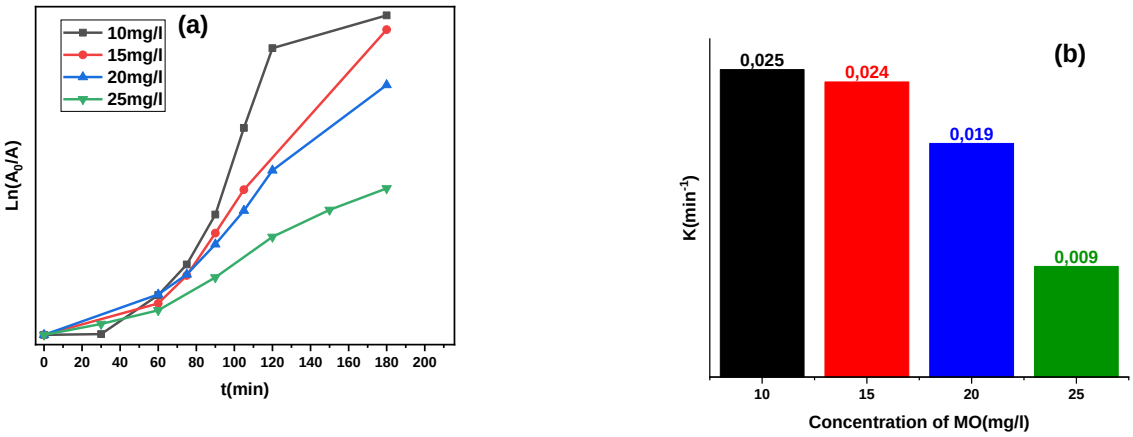


***Figure II.11***: (a) Photocatalytic curves and (b) rate constants for the degradation of MO molecules.

***Figure II.12*** shows the corresponding degradation results for MB molecules. The same trends were observed for MO but with different photocatalytic efficiencies and degradation rates. The effects of initial MB concentration on the degradation efficiency are presented in ***Table II.2***

where the best degradation (91.10%) was observed for 10 mg/L whereas the lowest photocatalytic efficiency of 72.22% was obtained for the highest MB concentration after 180 min of sunlight irradiation. This finding confirmed that ZnS-TGA NCs showed a significant decolorization performance causing the destruction of homo and hetro-poly aromatic rings contained in these dye molecules [45].

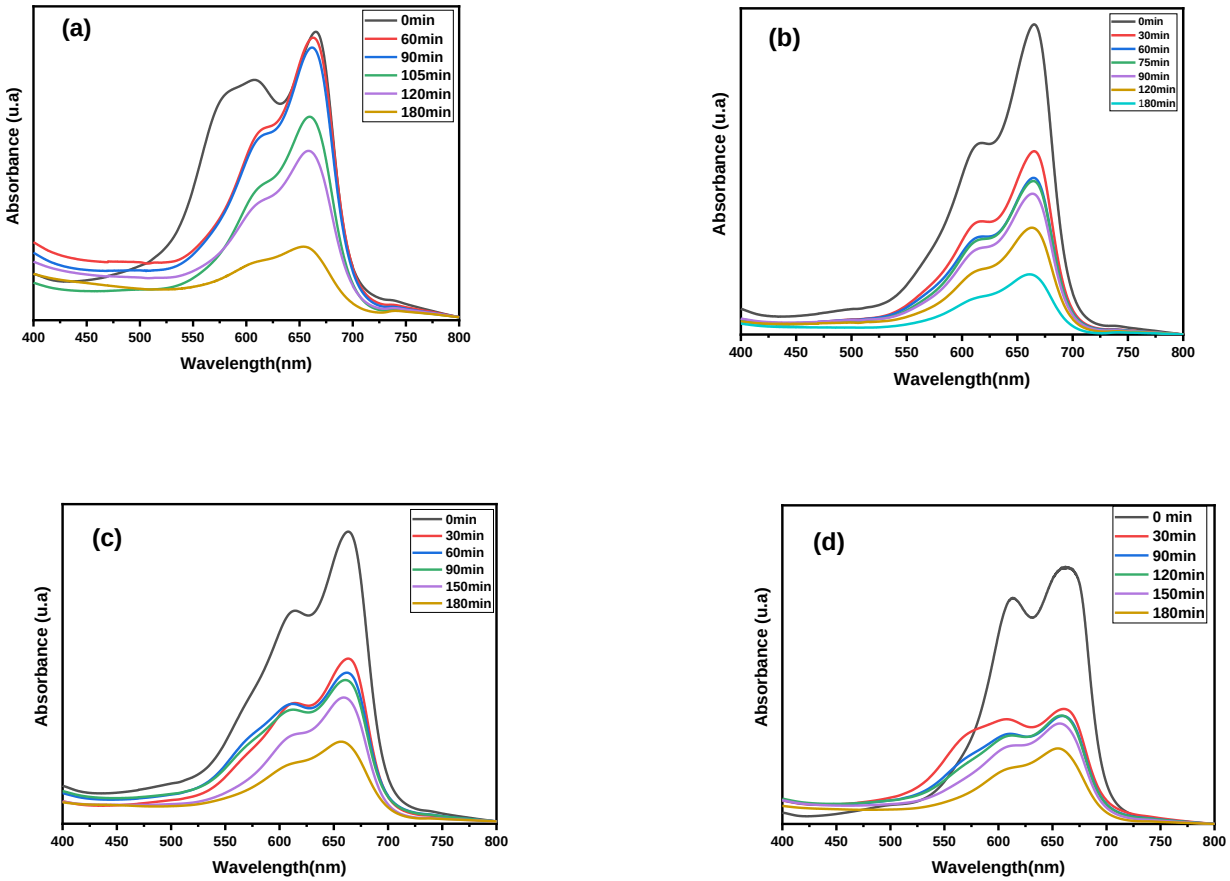


***Figure II.12*:** UV–visible absorption spectra for the MB decolorization using ZnS-TGA nanocrystals under sunlight irradiation. Initial MB concentration: (a) 10, (b) 15, (c) 20 and (d)25 mg/L.

***Table II.2***: Efficiencies for the degradation of MB using ZnS-TGA nanocrystals under sunlight irradiation.

| MB concentration (mg/L) | Degradation efficiency (%) |
|---|---|
| 10 | 91.10 |
| 15 | 84.12 |
| 20 | 73.95 |
| 25 | 72.22 |

***Figure II.13(a)*** and ***(b)*** report the calculation of the degradation rates for this dye. Overall, 99.04% and 91.10% degradation were observed for MO and MB molecules, respectively, due to the photo-generated electron hole in ZnS-TGA. This difference can be explained by the fact that ZnS-TGA NCs can easily destroy the N=N bonds under sunlight irradiation, which were present in MO molecule and not in MB molecule [68]. Consequently, the photocatalytic performance of these NCs was related to the charge separation, specific surface area and crystallinity [69]. The dye degradation efficiency may be also due to its molecular structure and charge state, which controlled the capacity of its attraction and adsorption on the NCs surface.

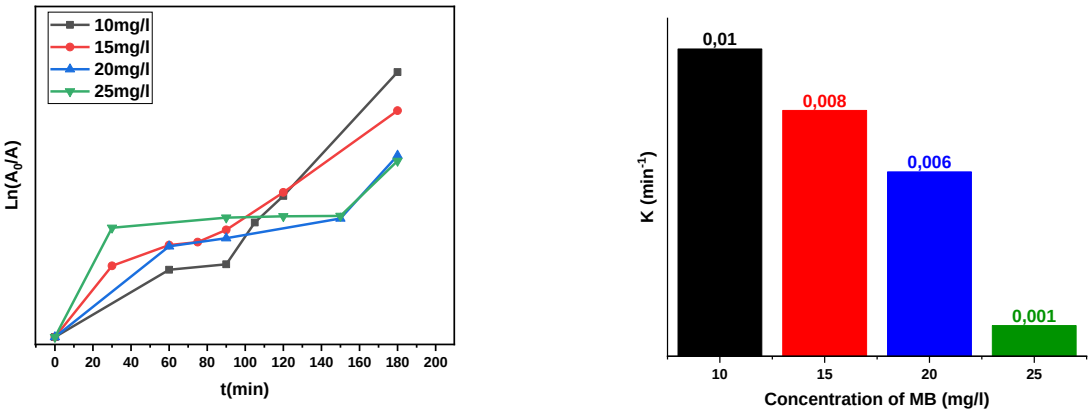


***Figure II.13***: (a) Photocatalytic curves and (b) rate constants for the degradation of MB molecules.

The photocatalytic performance of ZnS-TGA NCs was tested for MO/ MB dye mixtures. This study aimed to determine the capabilities of this nanocatalyst for the simultaneous degradation of these dyes. Fig. 14 shows the time-dependent photocatalytic degradation of these two dyes with different initial concentrations. Firstly, no other new peaks were observed in these spectra thus indicating that no new compounds occurred during the experiments with dye mixtures. This binary dye mixture generated two characteristic peaks at 465 and 665 nm that corresponded to the molecules MO and MB, respectively. Starting the photocatalytic activity by adding ZnS-TGA NCs under sunlight irradiation, a decrement in these two peaks was observed with increments of the irradiation time (***Table II.3***). This finding demonstrated that the codegradation of these dyes was performed using ZnS-TGA NCs. At concentration of 10 mg/L of both dyes, a total decolorization of the solution was observed with degradation efficiencies of 99.43% for MB and 95.73% for MO. At low dye concentrations, the photons easily reached the catalyst surface thus favoring the formation of $OH^*$ radicals. It was observed

a decrement in the degradation efficiency when the concentration increased up to 20 mg/L where similar results were observed for single dye solutions. However, the difference in terms of degradation efficiencies was very noticeable. In particular, the MB degradation was almost total (89.55%), while the MO degradation was very low (44.47%). Active sites of catalyst surface could be covered with dye molecules at high dye concentration thus reducing the generation of $OH^*$ radicals and, hence, affecting the photocatalytic activity. Moreover, the dye molecules were in competition for the adsorption on the NCs surface especially at high concentrations. In fact, the degradation efficiency of MB was higher than that of MO in the binary MO/MB mixture. The lower degradation of MO (44.47%) in the MO/MB mixture in comparison to MO solution (94.32%) can be associated with the competitive adsorption between MO and MB molecules in the mixture [70]. As indicated, MB is a cationic dye with $C\text{-}S^+\text{=}C$ functional group, while MO is an anionic dye with $SO_3^-$ group [38]. ZnS-TGA NCs can adsorb more MB molecules than MO in neutral media thus reflecting the negatively charged surface of this nanocatalyst [71]. Indeed, the increase of electrostatic attraction between positively charged dye cations and negatively charged adsorption sites resulted in an increment in MB dye degradation. Therefore, MB dye molecules were more likely to be degraded in the photocatalytic process for the mixture MO/MB, which explained the selectivity for MB than MO in the binary dye solution. 99.43–89.55% of MB was degraded after 180 min of sunlight irradiation in the MO/MB mixture. However, the MB degradation was just 91.10–73.95% in the single dye solution. This result indicated that MB was removed quickly in the presence of MO compared to single MB degradation. This could be explained by the presence of MO molecules in the solution, which could play the role of a second catalyst. Therefore, the adsorption of MB was higher than that of MO thus causing the presence of a significant amount of MO molecules not adsorbed in the solution [71]. These molecules could absorb sunlight irradiation, allowing MO excitation, which acted as a photocatalyst for MB degradation [71].

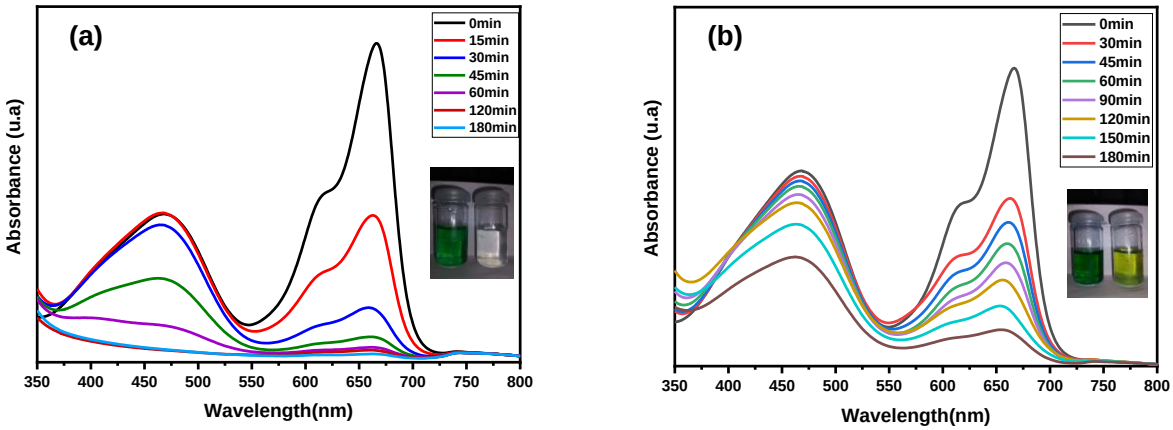


***Figure II.14***: UV–Visible absorption spectra of the simultaneous degradation of MB and MO molecules in binary solutions. Initial concentrations: (a) CMO=CMB=10 mg/L, (b) CMO=CMB=20 mg/L.

***Table II.3***: Efficiencies for the simultaneous degradation of MO and MB in binary mixtures using ZnS-TGA nanocrystals under sunlight irradiation.

| **Initial concentrations (mg/L)** | **Degradation efficiency of MO (%)** | **Degradation efficiency of MB (%)** |
|---|---|---|
| $C_{MO}=C_{MB}=10$ | 95.73 | 99.43 |
| $C_{MO}=C_{MB}=20$ | 44.47 | 89.55 |

The degradation rates of these dyes in the mixture were calculated and results are reported in ***Figure II.15(a)*** and ***(b)***. The highest degradation rate was obtained for both MB and MO with a concentration of 10 mg/L for each dye. On the other hand, K (0.0258 $min^{-1}$) of MB increased and K (0.0208 $min^{-1}$) of MO decreased in comparison to the results of single dye solutions. It can be concluded that mixing two dyes accelerated the degradation of MB. ***Table II.4*** compares the photocatalytic performance of ZnS-TGA NCs with other nanocatalysts reported in the literature. In general, ZnS-TGA NCs can be considered as a low-cost material prepared with non-toxic products that can operate under sunlight irradiation thus offering additional advantages with respect to other catalysts [72–83].

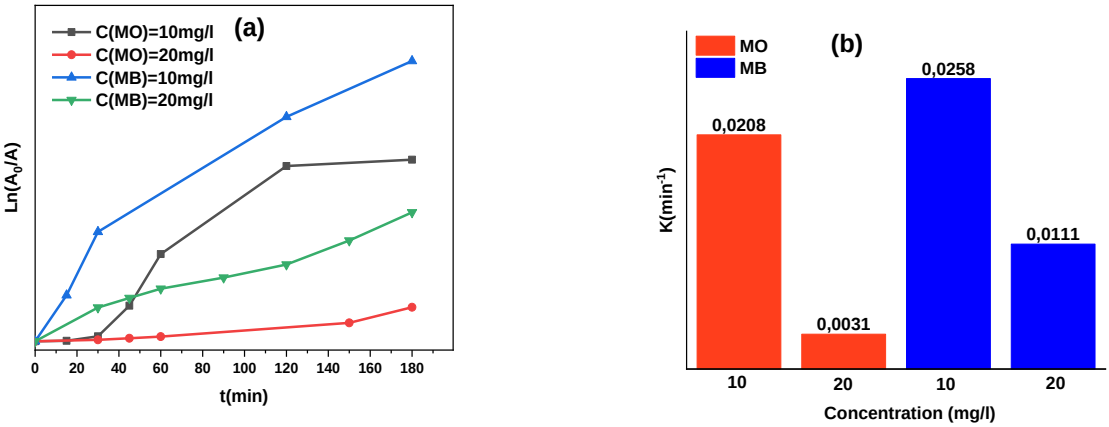


***Figure II.15***: (a) Plot of Ln ($A_0$/A) vs. irradiation time for MO and MB in MO/MB mixture; (b) Columns of co-dyes with different concentrations.

***Table II.4***: Comparison between literature results and our results.

| Sr No | Sample | Dye | Irradiation source | Time (min) | Degradation efficiency (%) | Ref. no. |
|---|---|---|---|---|---|---|
| **1** | Cr-doped ZnS | MO | UV light | 300 | 65.22 | [72] |
| **2** | g-poly /ZnS | MO | Sunlight | 240 | 69.00 | [73] |
| **3** | ZnS | MB | Visible light | 120 | 78.00 | [74] |
| **4** | ZnS | MO | Sunlight | 120 | 69.18 | [75] |
| **5** | ZnS | MO | Sunlight | 180 | 99.04 | This work |
| **6** | ZnS | MO | Sunlight | 150 | 77.00 | [76] |
| **7** | Chitosan-ZnS | MB | UV light | 120 | 87.00 | [12] |
| **8** | ZnS/RGO | MB | Visible light | 240 | 89.43 | [77] |
| **9** | ZnS | MB | Sunlight | 180 | 49.00 | [78] |
| **10** | ZnS | MB | Sunlight | 180 | 72.13 | [41] |
| **11** | TiO2/ZnO | MB | Visible light | 120 | 73.20 | [79] |
| **12** | ZnS | MB | Sunlight | 180 | 91.10 | This work |
| **13** | Pristine ZnS | MO/MB | Sunlight | 280 | 39.63 | [80] |
| **14** | 4% Cr/ZnS | MO/MB | Sunlight | 240 | 75.11 | [80] |
| **15** | ZnS | MO/MB | Sunlight | 180 | 95.73/99.43 | This work |
| **16** | Ag@AgI/ZnS | MO/MB | Sunlight | 80 | 41.37/ 95.29 | [81] |

| | | | | | | |
|---|---|---|---|---|---|---|
| **17** | ZnONR | MO/MB | UV light | 90 | 61.00/41.00 | [82] |
| **18** | ZnONR-RGO | MO/MB | UV light | 90 | 83.00/94.00 | [82] |
| **19** | CuO/NX | MO/MB | UV light | 120 | 60.00/27.00 | [83] |

### III.3 Mechanism of the photocatalytic process of MB/MO dye mixture

***Figure II.16*** describes the proposal of photocatalytic activity mechanism for the degradation of these dyes using ZnS-TGA NCs. After the addition of ZnS-TGA nanocatalysts to the dye solution, the dye molecules will be adsorbed on the NCs surface where the adsorption of MB molecules will be greater than that of MO molecules. Under sunlight irradiation, there will be a creation of (e-h) pairs and the electrons e– will transfer from valence band (VB) to the conduction band (CB) and the holes will be located in VB. These charge carriers will migrate to the nanocatalysts surface and the photo-induced electrons will be easily trapped by electronic acceptors, such as adsorbed $O_2$, to produce a super oxide anion radical ($O_2^{*-}$). The positive hole in the NCs will react with a water molecule to produce hydrogen gas and the free hydroxyl radical ($OH^*$), which is the most important and powerful oxidizing radical for the mineralization of adsorbed or free MO/MB molecules on the catalyst surface. Also, free MO molecules will absorb the solar irradiation that allows their excitation, which also acts as a catalyst for the degradation of MB molecules. The active species, $MO^*$, $OH^*$ and $O_2^{*-}$ radicals, can effectively degrade dye molecules to form intermediates and the final products ($CO_2$ and $H_2O$). The possible photocatalytic reactions can be summarized as follows:

$$\text{ZnS-TGA} + h\nu \rightarrow e_{BC}^- + h_{BV}^+ \quad (7)$$

$$e^- + O_2 \rightarrow O_2^{*-} \quad (8)$$

$$H_2O + h^+ \rightarrow OH^* + H^+ \quad (9)$$

$$h^+ + OH^- \rightarrow OH^* \quad (10)$$

$$MO + h\nu \rightarrow MO^* \quad (11)$$

$$MO^* + MB \rightarrow \text{Degradation products} + CO_2 + H_2O \quad (12)$$

$$O_2^{*-} + MO/MB \rightarrow \text{Degradation products} + CO_2 + H_2O \quad (13)$$

$$OH^* + MO/MB \rightarrow \text{Degradation products} + CO_2 + H_2O \quad (14)$$

Based on recent studies [11,76], the high photocatalytic performance of ZnS-TGA NCs can be explained by the formation of NCs enriched with sulfur vacancies (VS) and zinc interstitials (IZn) caused by stacking faults in core of the NCs. Some structural defects (e.g., dislocation density, microstrain and stacking faults) affected the particle size and the surface area, which enhanced the photocatalytic efficiency. These defects may cause the reduction of probability

for the recombination of chargers that diffused to the NCs surface where their interaction with water molecules and atmospheric oxygen would produce highly reactive species responsible for the degradation of adsorbed organic molecules.

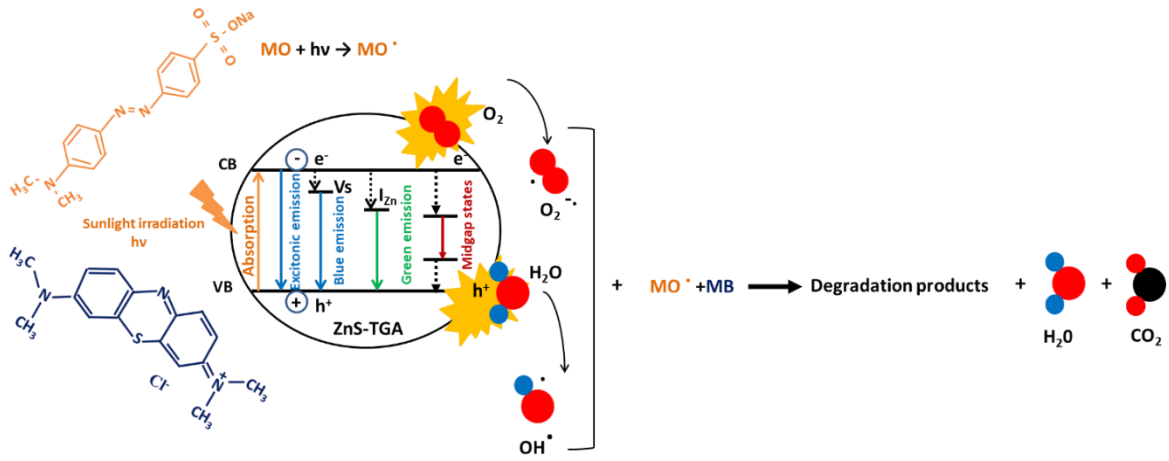


***Figure II.16***: Proposed dye co-degradation mechanism using ZnS-TGA nanocrystals.

## IV. Conclusion

Herein, we report a simple colloidal chemical route for the synthesis of ZnS-TGA nanocrystals using thioglycolic acid as a stabilizing agent. This synthesis route offered a high purity, low cost, simple implementation and low energy consumption where these nanocrystals can be used to obtain an effective material for dye removal from wastewaters. This study showed for the first time that the efficiency of ZnS-TGA nanocrystals was up to 99.43% to degrade MB and MO dye molecules under sunlight irradiation in a very short time of 27 min. Results of this study indicated that these nanocrystals are suitable for the treatment of wastewaters at industrial scale.

# V. References


[1] Y. Yu, L. Xu, J. Chen, H. Gao, S. Wang, J. Fang, S. Xu, Hydrothermal synthesis of GSH–TGA co-capped CdTe quantum dots and their application in labeling colorectal cancer cells, Colloids Surf. B Biointerfaces 95 (2012) 247–253.

[2] B. Chen, N. Pradhan, H. Zhong, From large-scale synthesis to lighting device applications of ternary I–III–VI semiconductor nanocrystals: inspiring greener material emitters, J. Phys. Chem. Lett. 9 (2018) 435–445.

[3] M. Sturaro, E.D. Gaspera, N. Michieli, C. Cantalini, S.M. Emamjomeh, M. Guglielmi, A. Martucci, Degenerately doped metal oxide nanocrystals as plasmonic and chemoresistive gas sensors, ACS Appl. Mater. Interfaces 8 (2016) 30440–30448.

[4] I. Ahmad, Nanocrystalline cellulose decorated quantum dots based tyrosinasebiosensor for phenol determination, Mater. Sci. Eng. C 99 (2019) 37–46.

[5] S. Huang, Y.V. Lim, X. Zhang, Y. Wang, Y. Zheng, D. Kong, M. Ding, S.A. Yang, H. Y. Yang, Regulating the polysulfide redox conversion by iron phosphide nanocrystals for high-rate and ultrastable lithium-sulfur battery, Nano Energy 51 (2018) 340–348.

[6] N. Tsvetkov, B.C. Moon, J.Y. Lee, J.K. Kang, Controlled synthesis of nanocrystalline Nb:SrTiO3 electron transport layers for robust interfaces and stable high photovoltaic energy conversion efficiency in perovskite halide solar cells, ACS Appl. Energy Mater. 3 (2020) 344–351.

[7] R.V. Djokic, D.A. Marinkovi, D.R. Petrovic, O. Ersen, S. Zafeiratos, M. Mitric, C. Ophus, R.V. Radmilovic, D. Janackovic, Highly active rutile $TiO_2$ nanocrystalline photocatalysts, ACS Appl. Mater. Interfaces 12 (2020) 33058–33068.

[8] H. Zhao, F. Rosei, Colloidal quantum dots for solar technologies, Chem 3 (2017) 229–258.

[9] S. Mathew, D.A. Saran, B.S. Bhardwaj, S.A. Joseph, P. Radhakrishnan, V.P. N. Nampoori, C.P.G. Vallabhan, R.J. Bellare, Size dependent optical properties of the CdSe-CdS core-shell quantum dots in the strong confinement regime, Int. J. Appl. Phys. 111 (2012) 074312–074320.

[10] V.I. Martynenko, S.A. Baimuratov, F. Weigert, X.J. Soares, L. Dhamo, P. Nickl, I. Doerfel, J. Pauli, D.I. Rukhlenko, V.A. Baranov, Photoluminescence of Ag–In–S/ ZnSquantum dots: excitation energy dependence and low-energy electronic structure, Nano Res. 12 (2019) 1595–1603.

[11] N.B.H. Mohamed, M. Bouzidi, N.B. Brahim, L. Sellaoui, M. Haouari, H. Ezzaouia, A. B. Petriciolet, Impact of the stacking fault and surface defects states of colloidal CdSe nanocrystals on the removal of reactive black 5, Mater. Sci. Eng. C 265 (2021) 115029–115046.

[12] G. Hosseinzadeh, A. Maghari, S.M.F. Farniya, A.H. Keihan, A.A.M. Movahedi, Interaction of insulin with colloidal ZnS quantum dots functionalized by various surface capping agents, Mater. Sci. Eng. C. 77 (2017) 836–845.

[13] Y. Yu, L. Xu, J. Chen, H. Gao, S. Wang, J. Fang, S. Xu, Hydrothermal synthesis of GSH–TGA co-capped CdTe quantum dots and their application in labeling colorectal cancer cells, Colloids Surf. B Biointerfaces 95 (2012) 247–253.

[14] C.D. Deka, A. Kalita, S. Bardaloi, P.C.M. Kalita, Influence of capping agent on structural, optical and photocatalytic properties of ZnS nanocrystals, J. Lumin. 210 (2019) 269–275.

[15] A.P.A. Mansur, S.H. Mansur, P.F. Ramanery, L.C. Oliveira, P.P. Souza, "Green" colloidal ZnS quantum dots/chitosan nano-photocatalysts for advanced oxidation processes: study of the photodegradation of organic dye pollutants, Appl. Catal. B 158–159 (2014) 269–279.

[16] D. Ayodhya, G. Veerabhadram, Fabrication of Schiff base coordinated ZnS nanoparticles for enhanced photocatalytic degradation of chlorpyrifos pesticide and detection of heavy metal ions, J. Mater. 5 (2019) 446–454.

[17] E.H. Ang, J. Zeng, G.S. Subramanian, V. Chellappan, T. Sudhaharan, P. Padmanabhan, B. Gulyás, S.T. Selvan, Silica-coated Mn-doped ZnS nanocrystals for cancer theranostics, ACS Appl. Nano Mater. 3 (2020) 3088–3096.

[18] A. Tabib, W. Bouslama, B. Sieber, A. Addad, H. Elhouichet, M. F´erid, R. Boukherroub, Structural and optical properties of Na doped ZnO nanocrystals: application to solar photocatalysis, Appl. Surf. Sci. 396 (2017) 1528–1538.

[19] N. Radhika, S.S.P. Selvin, J.A.I. Joice, T. Sivakumar, P. Merlin, I.S. Lydia, Fluorescent biomolecules capped ZnSe quantum dots and their photocatalytic activities, J. Nanosci. Nanotechnol. 18 (2018) 4634–4642.

[20] K. Qi, S. Liu, M. Qiu, Photocatalytic performance of $TiO_2$ nanocrystals with/ without oxygen defects, Chin. J. Catal. 39 (2018) 867–875.

[21] P.A. Ajibade, A.E. Oluwalana, B.M. Sikakane, M. Singh, Structural, photocatalytic and anticancer studies of hexadecylamine capped ZnSnanoparticles, Chem. Phys. Lett. 755 (2020), 137813.

[22] Z. Bujnˇ´ akov´ a, E. Dutkov´ a, M. Kello, J. Mojˇziˇs, M. Bal´ aˇz, P. Bal´ aˇz, O. Shpotyuk, Mechanochemistry of chitosan-coated zinc sulfide (ZnS) nanocrystals for bioimaging applications, Nanoscale Res. Lett. 12 (2017) 328–336.

[23] L. Chang, X. He, L. Chen, Y. Zhang, Mercaptophenylboronic acid-capped Mn-doped ZnS quantum dots for highly selective and sensitive fluorescence detection of glycol proteins, Sens. Actuators B Chem. 243 (2017) 72–77.

[24] D.D. Diestra, B. Thapa, J.B. Huarac, B.R. Weiner, G. Morell, L-cysteine capped ZnS: Mn quantum dots for room-temperature detection of dopamine with high sensitivity and selectivity, Biosens. Bioelectron. 87 (2017) 693–700.

[25] A.N. Rao, B. Sivasankar, V. Sadasivam, Kinetic studies on the photocatalytic degradation of direct yellow 12 in the presence of ZnOCatalyst, J. Mol. Catal. A. Chem. 306 (2009) 77–81.

[26] Z.S. Seddigi, Removal of Alizarin Yellow dye from water using zinc doped $WO_3$ catalyst, Bull. Environ. Contam. Toxicol. 84 (2010) 564–567.

[27] M.A. Rauf, S.S. Ashraf, Radiation induced degradation of dyes – an overview, J. Hazard. Mater. 166 (2009) 6–16.

[28] D.A. Yaseen, M. Scholz, Textile dye wastewater characteristics and constituents of synthetic efuents: a critical review, Int. J. Environ. Sci. Technol. 16 (2019) 1193–1226.

[29] D. Mishra, M. Srivastava, Low-dimensional nanomaterials for the photocatalytic degradation of organic pollutants. Nano-Materials as Photocatalysts for Degradation of Environmental Pollutants Elsevier Science, Elsevier Science, Varanasi, India, 2020, https://doi.org/10.1016/B978-0-12-818598-8.00002-X.

[30] A. Garmroudi, M. Kheirollahi, S.A. Mousavi, M. Fattahi, E.H. Mahvelati, Effects of graphene oxide/TiO2 nanocomposite, graphene oxide nanosheets and Cedr extraction solution on IFT reduction and ultimate oil recovery from a carbonate rock, Petroleum (2020), https://doi.org/10.1016/j.petlm.2020.10.002.

[31] F.B. Shareh, M. Kazemeini, M. Asadi, M. Fattahi, Metal promoted mordenite catalyst for methanol conversion into light Olefins, Pet. Sci. Technol. 32 (2014) 1349–1356.

[32] M.Z. Pedram, M. Kazemeini, M. Fattahi, A. Amjadian, A physicochemical evaluation of modified HZSM-5 catalyst utilized for production of dimethyl ether from methanol, Pet. Sci. Technol. 32 (2014) 904–911.

[33] M.N. Chonga, Z.Y. Tneu, P.E. Poha, B. Jinc, R. Aryal, Synthesis, characterisation and application of TiO2–zeolite nanocomposites for the advanced treatment of industrial dye wastewater, Taiwan. Inst. Chem. Eng. 50 (2015) 288–296.

[34] E.V. Stelmashook, E.E. Genrikhs, E.V. Mukhaleva, M.R. Kapkaeva, R. V. Kondratenko, V.G. Skrebitsky, N.K. Isaev, Neuroprotective effects of methylene blue in vivo and in vitro, Bull. Exp. Biol. Med 167 (2019) 455–459.

[35] M.T. Islam, R.S. Arana, C. Hernandez, T. Guinto, M.A. Ahsan, D.T. Bragg, H. Wang, B.A. Tenorio, Conversion of waste tire rubber into a high-capacity adsorbent for the removal of methylene blue, methyl orange, and tetracycline from water, J. Environ. Chem. Eng. 6 (2018) 3070–3082.

[36] T. Tatarchuka, N. Paliychuk, R.B. Bitra, A. Shyichuk, M. Naushad, I. Mironyuk, D. Zio´łkowska, Adsorptive removal of toxic Methylene Blue and Acid Orange 7 dyes from aqueous medium using cobalt-zinc ferrite nanoadsorbents, Desalin. Water Treat. 150 (2019) 374–385.

[37] P.K. Jaseela, J. Garvasis, A. Joseph, Selective adsorption of methylene blue (MB) dye from aqueous mixture of MB and methyl orange (MO) using mesoporous titania ($TiO_2$) – polyvinyl alcohol (PVA) nanocomposite, J. Mol. Liq. 286 (2019) 110908–110917.

[38] E. Bazrafshan, A.A. Zarei, H. Nadi, M.A. Zazouli, Adsorptive removal of Methyl Orange and Reative Red 198 dyes by Moringa peregrine ash, Indian. J. Chem. Technol. 21 (2014) 105–113 (+).

[39] L.V. Trandafilovi´c, D.J. Jovanovi´c, X. Zhang, S. Ptasi´nska, M.D. Drami´canin, Enhanced photocatalytic degradation of methylene blue and methylorange by ZnO: Eu nanoparticles, Appl. Catal. B 203 (2017) 740–752.

[40] N.B.H. Mohamed, M. Haouari, Z. Zaaboub, F. Hassen, H. Maaref, H.B. Ouada, Effect of surface on the optical structure and thermal properties of organically capped CdSnanoparticles, J. Phys. Chem. Solids 75 (2014) 936–944.

[41] C. PijushDey, R. Das, Enhanced photocatalytic degradation of methyl orange dye on interaction with synthesized ligand free CdS nanocrystals under visible light illumination, Spectrochim. Acta A Mol. Biomol. Spectrosc. 231 (2020) 118122–118130.

[42] R. Chauhan, A. Kumar, R. Chaudhary, Photocatalytic degradation of methylene blue with Cu doped ZnS nanoparticles, J. Lumin 145 (2014) 6–12.

[43] D.A. Reddya, C. Liua, R.P. Vijayalakshmid, B.K. Reddya, Effect of Al doping on the structural, optical and photoluminescence properties of ZnS nanoparticles, J. Alloy. Compd. 582 (2014) 257–264.

[44] F. Dehghan, M. Molaei, F. Amirian, M. Karimipour, A.R. Bahador, Improvement of the optical and photocatalytic properties of ZnSe QDs by growth of ZnS shell using a new approach, Mater. Chem. Phys. 206 (2018) 76–84.

[45] M. Jothibas, C. Manoharanb, S.J. Jeyakumara, P. Praveenc, I.K. Punithavathya, J. P. Richard, Synthesis and enhanced photocatalytic property of Ni doped ZnS nanoparticles, J. Sol. Energy 159 (2018) 434–443.

[46] B. Poornaprakasha, U. Chalapathia, Y. Suha, S.V.P. Vattikutib, M.S.P. Reddyc, S. Parka, Terbium-doped ZnS quantum dots: Structural, morphological, optical, photoluminescence, and photocatalytic properties, Ceram. Int. 44 (2018) 11724–11729.

[47] G.S. Pandya, P.J. Corbett, M.W. Jadwisienczak, E.M. Kordesch, Structural characterization and X-ray analysis by Williamson-Hall method for erbium doped aluminum nitride nanoparticles, synthesized using inert gas condensation technique, Phys. E Low. Dimens. Syst. Nanostruct. 79 (2016) 98–104.

[48] L.J. Meng, A. Maçarico, R. Martins, Study of annealed indium tin oxide films prepared by rf reactive magnetron sputtering, Vacuum 46 (1995) 673–680.

[49] N.B. Brahim, M. Poggi, N.B.H. Mohamed, R.B. Chaabane, M. Haouari, M. Negrerie, H.B. Ouada, Synthesis, characterization and spectral temperature-dependence of thioglycerol-CdSe nanocrystals, J. Lumin 177 (2016) 402–408.

[50] J.F. Suyver, S.F. Wuister, J.J. Kelly, A. Meijerink, Synthesis and photoluminescence of nanocrystalline ZnS:$Mn^{2+}$, Nano Lett. 1 (2001) 429–433.

[51] H.S. Mansur, A.A.P. Mansur, CdSe quantum dots stabilized by carboxylicfunctionalized PVA: synthesis and UV–vis spectroscopy characterization, Mater. Chem. Phys. 125 (2011) 709–717.

[52] Y.P. Varshni, Temperature dependence of the energy gap in semiconductors, Physica 34 (1967) 149–154.

[53] N.B.H. Mohamed, M. Haouari, Z. Zaaboub, M. Nafoutti, F. Hassen, H. Maaref, H. B. Ouada, Time resolved and temperature dependence of the radiative properties of thiol-capped CdS nanoparticles films, J. Nanopart. Res. 16 (2014) 2242–2258.

[54] X. Wang, J. Shi, Z. Feng, M. Lia, C. Li, Visible emission characteristics from different defects of ZnSnanocrystals, Phys. Chem. Phys. 13 (2011) 4715–4723.

[55] S.F. Wuister, C.D.M. Donega, A. Meijerink, Luminescence temperature antiquenching of water-soluble CdTe quantum dots: role of the solvent, J. Am. Chem. Soc. 126 (2004) 10397–10402.

[56] Y. Nonoguchi, T. Nakashima, T. Kawai, Size-and temperature-dependent emission properties of zinc-blende CdTe Nanocrystals in Ionic Liquid, J. Phys. Chem. C 111 (2007) 11811–11815.

[57] X. Xu, Y. Zhao, E. Sie, Y. Lu, B. Liu, S. Ekahana, J. Xiao, Q. Jiang, J. Wang, H. Sun, T. Sum, C. Huan, Y. Feng, Q. Xiong, Dynamics of bound exciton complexes in CdS nanobelts, ACS Nano 5 (2011) 3660–3669.

[58] N.B.H. Mohamed, N.B. Brahim, R. Mrad, M. Haouari, R.B. Chaˆ abane, M. Negrerie, Use of MPA-capped CdS quantum dots for sensitive detection and quantification of $Co^{2+}$ ions in aqueous solution, Anal. Chim. Acta 1028 (2018) 50–58.

[59] M. Sharma, T. Jain, S. Singh, O.P. Pandey, Photocatalytic degradation of organic dyes under UV–visible light using capped ZnS nanoparticles, Sol. Energy 86 (2012) 626–633.

[60] C. Würth, M. Grabolle, J. Pauli, M. Spieles, U.R. Genger, Comparison of methods and achievable uncertainties for the relative and absolute measurement of photoluminescence quantum yields, Anal. Chem. 83 (2011) 3431–3439.

[61] M.A. Munro, S.D. Ginger, Photoluminescence quenching of single CdSe nanocrystals by ligand adsorption, Nano Lett. 8 (2008) 2585–2590.

[62] J.A. Duffie, W.A. Beckman, Solar Engineering of Thermal Processes, fourth ed., John Wiley & Sons, Inc, Hoboken, New Jersey, 2013.

[63] H. Ghodbane, O. Hamdaoui, Decolorization of antraquinonic dye, C.I. Acid Blue 25, in aqueous solution by direct UV irradiation, UV/$H_2O_2$ and UV/Fe(II) processes, Chem. Eng. J. 160 (2010) 226–231.

[64] Y. Zong, Z. Li, X. Wang, J. Ma, Y. Men, Synthesis and high photocatalytic activity of Eu-doped ZnO nanoparticles, Ceram. Int. 40 (2014) 10375–10382.

[65] X. Fang, L. Wu, L. Hu, ZnS nanostructure arrays: a developing material star, Adv. Mater. 23 (2011) 585–598.

[66] J. Grzechulska, A.W. Morawski, Photocatalytic decomposition of azo-dye acid black 1 in water over modified titanium dioxid, Appl. Catal. B 36 (2002) 45–51.

[67] N. Daneshvar, D. Salari, A.R. Khataee, Photocatalytic degradation of azo dye acid red 14 in water: investigation of the effect of operational parameters, J. Photochem. Photobiol. A 157 (2003) 111–116.

[68] Z. Ye, L. Kong, F. Chen, Z. Chen, Y. Lin, C. Liu, A comparative study of photocatalytic activity of ZnS photocatalyst for degradation of various dyes, Optik 164 (2018) 345–354.

[69] Q.P. Zhang, X.N. Xu, Y.T. Liu, M. Xu, S.H. Deng, Y. Chen, H. Yuan, F. Yu, Y. Huang, K. Zhao, S. Xu, G. Xiong, A feasible strategy to balance the crystallinity and specific surface area of metal oxide nanocrystals, Sci. Rep. 7 (2017) 46424–46435.

[70] C. Wang, Y. Zhang, T. Zhu, P. Wang, S.J. Gao, Photocatalytic degradation of methylene blue and methyl orange in a Zn(II)-based metal–organic framework, Desalin. Water Treat. 57 (2016) 17844–17851.

[71] C.H. Nguyen, C.C. Fu, R.S. Juang, Degradation of methylene blue and methyl orange by palladium-doped $TiO_2$ photocatalysis for water reuse: efficiency and degradation pathways, J. Clean. Prod. 202 (2018) 413–427.

[72] A. Eyasu, O. Yadav, R. Bachheti, Photocatalytic degradation of methyl orange dye using Cr-doped ZnS Nanoparticles under visible radiation, Int. J. ChemTech Res. 5 (2013) 1452–1461.

[73] D. Pathania, D. Gupta, A. Al-Muhtaseb, G. Sharma, A. Kumar, M. Naushad, T. Ahamad, S. Alshehri, Photocatalytic degradation of highly toxic dyes using chitosan-g-poly(acrylamide)/ZnS in presence of solar irradiation, J. Photochem. Photobiol. A. 329 (2016) 61–68.

[74] Z. Ye, L. Kong, F. Chen, Z. Chen, Y. Lin, C. Liu, A comparative study of photocatalytic activity of ZnS photocatalyst for degradation of various dyes, Optik 164 (2018) 345–354.

[75] A. Phuruangrat, K. Karthik, B. Kuntalue, P. Dumrongrojthanath, S. Thongtem, T. Thongtem, Refuxing synthesis and characterization of ZnS nanoparticles and their photocatalytic properties, J. Chalcogenide Lett. 16 (2019) 387–393.

[76] S. Pradeep, S. Raghuram, M.G. Chaudhury, S. Mazumder, Synthesis and characterization of Fe3+ and Mn2+ doped ZnS quantum dots for photocatalytic applications: effect of 2-mercaptoethanol and chitosan as capping agents, J. Nanosci. 17 (2017) 1125–1132.

[77] X. Chen, H. Li, M. Chen, W. Li, Z. Yuan, R. Snyders, Visible-light-driven photocatalytic activities of monodisperse ZnS-coated reduced graphene oxide nanocomposites, Mater. Chem. Phys. 227 (2019) 368–374.

[78] K. Ramki, A.R. Priya, P. Sakthivel, G. Murugadoss, R. Thangamuthu, M.R. Kumar, Rapid degradation of organic dyes under sunlight using tin-doped ZnS nanoparticles, J. Mater. Sci. Mater. Electron. 31 (2020) 8750–8760.

[79] M.R.D. Khaki, M.S. Shafeeyan, A.A.A. Raman, W.M.A.W. Daud, Evaluating the efficiency of nanosized Cu doped TiO2/ZnO photocatalyst under visible light irradiation, J. Mol. Liq. 258 (2017) 354–365.

[80] D.V. Dake, N.D. Raskar, V.A. Mane, R.B. Sonpir, E. Stathatos, K. Asokan, P.D. Babu, B. Dole, Exploring the role of defects on diverse properties of Cr-substituted ZnS nanostructures for photocatalytic applications, Appl. Phys. A. 126 (2020) 640–654.

[81] D.A. Reddy, J. Choi, S. Lee, T.K. Kim, Controlled synthesis of heterostructuredAg@ AgI/ZnS microspheres with enhanced photocatalytic activity and selective separation of methylene blue from mixture dyes, J. Taiwan. Inst. Chem. Eng. (2016) 1–10.

[82] S.V. Nipane, P.V. Korake, G.S. Gokavi, Graphene-zinc oxide nanorod nanocomposite as photocatalyst for enhanced degradation of dyes under UV light irradiation, Ceram. Int 43 (2014) 4549–4557.

[83] A.N. Ejhieh, M.K. Shamsabadi, Comparison of photocatalytic efficiency of supported CuO onto micro and nano particles of zeolite X in photodecolorization of methylene blue and methyl orange aqueous mixture, Appl. Catal. A. Gen. 477 (2014) 83–92.

# *Chapitre III*

## *A Novel Green Synthesis of Zinc Sulfide Nano-Adsorbents Using Artemisia Herba Alba Plant Extract for Adsorption and Photocatalysis of Methylene Blue Dye*

## Résumé

Nous rapportons une voie facile et verte pour une nouvelle synthèse de nanoparticules de sulfure de zinc (ZnS), pour la première fois, en utilisant l'extrait de plante d'Artemisia Herba Alba (AHA) pour une adsorption/photodégradation efficace du colorant bleu de méthylène (MB). Les résultats du FTIR ont confirmé la fonctionnalisation de la surface des nano-adsorbants par les molécules d'AHA. L'analyse XRD a indiqué la formation de nanocristaux avec une phase cubique presque pure. La taille moyenne des nanocristaux de ZnS stabilisés d'AHA calculée en utilisant la formule de Debye-Scherrer et observée par HR-TEM était de 4 nm. Les spectres d'absorption optique représentent l'apparition d'un bord d'absorption décalé vers des longueurs d'onde courtes par rapport à celui du semi-conducteur à l'état massif ZnS. La spectroscopie PL a indiqué qu'aucune intensité d'émission significative n'a été observée, ce qui a clairement révélé que les ligands AHA pouvaient jouer le même rôle que les ligands organiques pour une utilisation dans des applications de luminescence. Ces nanoparticules ont été utilisées pour l'élimination de MB sous source d'irradiation solaire à partir d'une solution colloïdale aqueuse pour étudier la synergie adsorption-photocatalyse. Les résultats ont démontré une adsorption exothermique spontanée avec une capacité d'adsorption allant jusqu'à 29,92 mg/g. Des isothermes d'adsorption et des calculs de physique statistique ont été utilisés pour analyser les paramètres stériques et énergétiques associés à l'adsorption MB à la surface des nano-adsorbants. Les nanoparticules vertes de ZnS ont montré une activité photocatalytique remarquable en utilisant la lumière solaire pour la degradation du MB avec un taux de conversion de 89,18 % dans la première heure. Les nanoparticules de ZnS-AHA ont prouvé une adsorption élevée et une capacité photocatalytique élevée, ce qui indique que les nouveaux extraits de plantes sont un agent de capsulage prometteur pour des applications écologiques et environnementales potentielles.

# *A Novel Green Synthesis of Zinc Sulfide Nano-Adsorbents Using Artemisia Herba Alba Plant Extract for Adsorption and Photocatalysis of Methylene Blue Dye*


## Abstract

We report a facile and green route for a new synthesis of sulfide nanoparticles (ZnS NPs) using Artemisia Herba Alba (AHA) plant extract for efficient adsorption/photodegradation of methylene blue dye (MB). Results exhibited a blue shift in the absorbance band and higher energy band gap values than bulk ZnS materials, which was due to the quantum confinement effects. X-ray diffraction confirmed the formation of the cubic phase of ZnS-AHA nanocrystals with a calculated average size of 4 nm. Green synthesized ZnS NPs show enhanced adsorption efficiency toward MB from contaminated water. ZnS-AHA NPs showed a specific surface area of 36.82 cm2 $g^{-1}$ and an adsorption capacity of 31.17 mg $g^{-1}$ for MB. The Langmuir–Freundlich model modeled adsorption data. The photocatalytic degradation performance of the green nanoparticles under sunlight irradiation showed a remarkable dye degradation rate of 94.09% in 180 min. In summary, this eco-friendly NPs is a highly promising material to be used in wastewater treatment for the removal of organic compounds.



***Keywords***: Green synthesis; *Artemisia Herba Alba*; Nanoparticles; Adsorption; Statistical physics modeling; Photocatalysis; Methylene blue


## I. Introduction

Finding a way to treat wastewater that is safe for living things, cheap, and effective remains a challenge for humanity. Due to the widespread industrialization of the world, the situation is much worse than it used to be. This has caused many serious problems for our environment, such as the pollution of water by dumping pollutants like organic dyes into rivers, lakes, streams, and ponds without first cleaning them [1]. These toxic chemicals are difficult to biodegrade, and they remain in soil and water for years, which causes serious health dangers to living organisms and also reduces soil fertility as the photosynthetic activity of aquatic plants results in the development of anoxic conditions for aquatic flora [2,3]. To protect the environment, it is important to limit these toxic wastes as much as possible by coming up with an effective way to treat wastewater before it is released. In recent decades, numerous chemical, physical and biological methods were proposed for wastewater treatment, including membrane-based processes, ultrafiltration, and reverse osmosis [4]. Nevertheless, dyes reveal high

solubility in water, which makes them difficult to eliminate by such traditional procedures [5, 6]. Among the current techniques, the so-called advanced oxidation processes (AOP) have emerged as one of the most powerful means for dye degradation. Some AOPs methods such as ozonation have reached a level of development at an industrial scale, while others are in full development in the research field [7]. These processes allow the elimination of organic pollutants at atmospheric pressure and ambient temperature using extremely oxidizing and reactive radical species able Heterogeneous solar photocatalysis is one of the most studied, environmentally compatible, and efficient processes for degrading many non-biodegradable pollutants using solar resources [8]. A photocatalyst is used in this process to start a chemical reaction when it is exposed to sunlight. In this process, the photocatalyst is typically a semiconductor material, which absorbs light and generates electron–hole pairs that can react with water and other organic molecules. Among the different semiconductors, zinc sulfide (ZnS) has been the focus of much attention in view of its low cost, abundance, good stability, non-toxicity, and high optical absorption in the visible and ultraviolet ranges [9]. Indeed, ZnS nanoparticles (NPs) are synthesized through various methods, including chemical precipitation, solvothermal synthesis, and hydrothermal synthesis [10]. These methods allow for precise control over the size, shape, and properties of the nanoparticles. ZnS NPs have potential applications in various fields, including as a material for optoelectronic devices, such as solar cells and light-emitting diodes (LEDs), and as a photocatalyst for water splitting and pollutant degradation [11]. They have also been studied for their potential in biomedical applications, such as imaging and drug delivery. Traditional ways of making NPs, on the other hand, often involve using toxic chemicals and solvents, which can be bad for the environment. Therefore, there is a growing interest in developing environmentally friendly methods for the biosynthesis of NPs. One such approach is the use of biological agents, such as microorganisms, plants, and enzymes, for the synthesis of NPs. These agents can reduce metal ions and generate NPs through a process known as bio-reduction. For example, nanoparticles can be synthesized using biological substances such as plants, algae [12], bacteria [13], fungi, and viruses [14], which is defined as a novel, simple, fast, economic and ecological alternative. Currently, there is an increasing interest in the green chemistry method for synthesizing zinc sulfide [15, 16]. Rajabi et al. used the leaf extract of *F. Johannis*, and they obtained spherical and semi-spherical nanoparticles of ZnS [17]. On the other side, Kannan et al. reported on the synthesis of ZnS nanoparticles with a spherical form and an average size between 5 and 20 nm using *Acalypha indica* and *Tridax procumbens* [18]. Plant extracts have several benefits, such as safe handling and non-toxicity. Also, they can act as both reducing and stabilizing agents for nanoparticles,

allowing the simple fabrication of large amounts of nanoparticles [19]. To our knowledge, the use of an aqueous extract of *Artemisia Herba Alba* (AHA) for the green synthesis of ZnS nanoparticles has not been reported. In this context, *Artemisia Herba Alba* is a species of aromatic plant that belongs to the family Asteraceae. It is commonly known as desert wormwood, or also known in Tunisia as 'Chih', and is native to degrade a wide variety of molecules, and they may eventually lead to the complete mineralization of the pollutants. to North Africa and the Middle East [20]. This plant has a woody stem and grows up to 60 cm tall. The leaves are silver-gray in color, hairy, and divided into small lobes. The plant produces small, yellow flowers in the summer. The AHA plant has been used in traditional medicine for a variety of purposes, including the treatment of digestive disorders, respiratory problems, and skin conditions. It is also used as a natural insect repellent [20]. Recent studies have shown that the plant contains compounds with potential therapeutic properties, including antioxidant, anti-inflammatory, and antimicrobial effects. However, more research is needed to fully understand the plant's potential benefits [21]. This desert wormwood has more than 160 individual components, including many essential oils, terpenoids, flavonoids, luteolin and flavones [22]. These phyto-bioactive constituents, which are present in the aqueous extract of AHA, play an essential role in capping and stabilizing the biosynthesized nanoparticles. In the present study, the authors attention is focused on preparing a new green synthesis of ZnS colloidal nanoparticles using *Artemisia Herba Aba* (ZnS-AHA) plant extract by chemical route and subjecting them to several experimental techniques to explore their applications in the adsorption/ photodegradation of a cationic thiazine dye, methylene blue (MB). MB is a cationic dye commonly used in industries such as textiles, paper, and printing [23]. The adsorption of MB on green-capped ZnS NPs was studied at different operating conditions. The effect of temperature on the adsorption process was analyzed. MB degradation with ZnS-AHA nanocatalysts was assessed at operating conditions under sunlight irradiation.

# II. Experimental

Details regarding experimental and Artemisia Herba Alba extraction should be found in the supplementary information (***Figure III.S1)***.

# III. Results and Discussion

## III.1 ZnS-AHA Nanoparticules Characterization

The compositions of biologically active compounds in *A. annua* extract utilized for ZnS-AHA NPs preparation were determined by FTIR analysis. The FTIR spectrum is presented in ***Figure***

***III.S2***. The FTIR analysis exhibited a major vibrational band at 540 $cm^{-1}$, which is associated with the Zn–S stretching vibrations [24, 25]. The absorption peak was observed at 3319 $cm^{-1}$ which is due to the alcohol/ phenol group (–OH) stretching vibration [26]. The peak at 2978 $cm^{-1}$ is probably ascribed to C-H alkane stretching, while the band at 2893 $cm^{-1}$ could be assigned to the C-H stretching of branched alkenes, particularly from AHA extract [27, 28]. The peaks of FT-IR analysis were evidence that the ZnS-AHA NPs were alleviated with the major phytoconstituents of *Artemisia Herba Alba* extract utilized for ZnS NPs fabrication.

The crystal structures of the as-synthesized ZnS nanoparticles prepared using AHA were determined by X-ray diffraction analysis; see ***Figure III.S3***. XRD confirmed the formation of the cubic phase of ZnS-AHA nanocrystals with a calculated average size of 4 nm. The sharp and narrow peaks implied that the ZnS-AHA NPs were highly crystallized [29]. The smaller size of the ZnS crystallites encapsulated by AHA extract is most likely due to the strong interaction of AHA molecules with ZnS nanocrystals [30].

The size distribution and morphology of the synthesized ZnS-AHA NPs were imaged using HR-TEM. The ZnS-AHA NPs microscopic analysis with TEM was presented in ***Figure III.S4a***. In general, the TEM images have revealed the sphere's spherical shape, with diameters in the range of 4 nm. These results are in good agreement with the XRD results. The d-spacing determined from the digital micrograph for ZnS is 0.30 nm, which is close to the spacing of the (111) diffraction plane of the cubic phase [8]. NPs elemental composition was determined by EDX (***Figure III.S4b***). Zn and S are the major elemental components. The presence of C is related to the TEM grid, and other peaks, Si and P, are probably due to residues coming from the synthesis and the grid.

***Figure III.S5*** shows the optical absorption spectra of the ZnS NPs that were spread out in water. A broad, strong absorption band located at 325 nm confirms the single-dispersed nature of ZnS-AHA NPs distribution [31]. The estimated band gap energy for the green ZnS using the Tauc relation [32] is 3.70 eV, which indicates that the gap energy of ZnS-AHA NPs shifts towards the blue compared to that of bulk ZnS (Eg = 3.6 eV).

The photoluminescence spectra of the synthetized nanoparticles dispersed in water were recorded in (***Figure III.S6***). An intense and wide band centered at 450 nm dominates the spectrum, which was attributed to recombination between electrons and holes at the edges of the conduction and valence bands, respectively [33, 34]. The FWHM of the main emission band is equal to 62 nm, which is related to the size dispersion of the ZnS-AHA NPs. In the extra information, you can find more information about how our samples are described.

## III.2 Adsorption Study of MB on AHA Capped ZnS Nanoparticles

In general, studies show that the amount of dye that can be removed increases significantly as the adsorbent's efficiency goes up [35]. The effect of the mass of the AHA-capped ZnS NPs on the MB adsorption is revealed in ***Figure III.1***. The amount of the nano-adsorbents is varied from 0.1 to 2 g, the concentration of dye being 10 mg/l at pH = 7, the temperature being 298 K, and the contact time being 120 min. This figure exhibits that the removal of dye increases as the amount of the adsorbent increases. This is easily understandable, as the increase in adsorbent mass increases the available surface area and therefore the number of adsorption sites available [36] and consequently increases the amount of dye adsorbed. The dye removal reached approximately 95.91% using 1 g of green AHA-capped NPs, which is related to a large number of adsorption sites. On further addition of adsorbents, a decrease in the adsorption efficiency of nano-adsorbents was observed. This is explained by the fact that the accessibility of adsorbent active sites with higher energy decreases, and only the active sites with lower energy are available to be occupied [37]. Therefore, the optimum amount for dye removal was chosen to be 1 g of ZnS-AHA NPs.

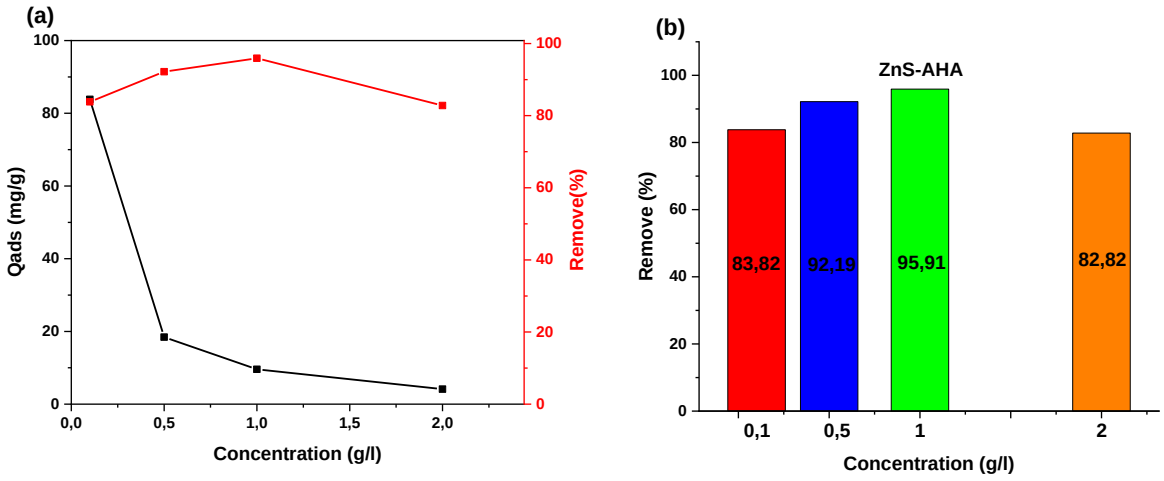


***Figure III.1***: (a) Effect of ZnS-AHA mass on the MB adsorption and (b) Efficiency of MB adsorption.

The pH of the solutions is also an important factor that influences the capacity of the adsorbent by influencing the surface charge of the nanoparticles [24]. The effect of the solution pH on the dye adsorption was studied from 5 to 9, when keeping the dye concentration equal to 10 mg/l, the adsorbent quantity equal to 1 g and the temperature at 300 K. As shown in ***Figure III.2***, the percentage of dye removal increased gradually from 70.55 to 95.91% when pH varies from 3

to 7; this is due to the electrostatic interactions between the positively charged dye molecules and the negatively charged adsorbents [24]. On the other hand, a decreasing trend in the dye removal efficiency was observed with a further increase in pH to 9. The pH value equal to 7 was fixed as the optimum pH for MB dye experiments.

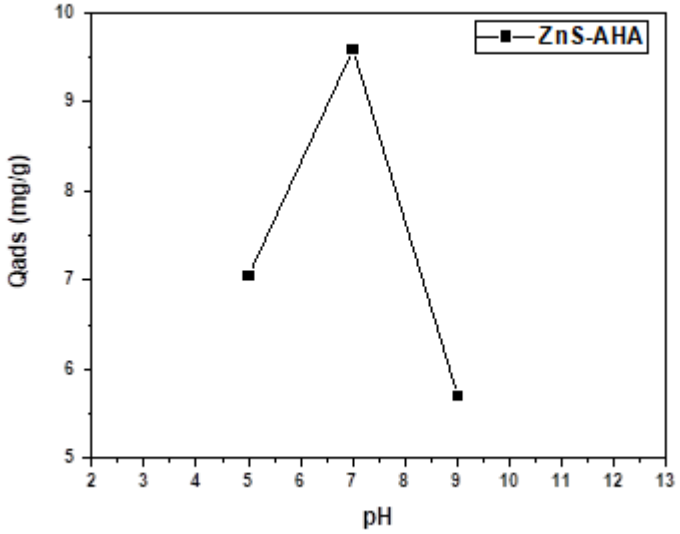


***Figure III.2***: Effect of pH on the adsorption of MB by AHA-capped ZnS NPs.

Over time, adsorption was studied to find out how much dye was taken up at different times. Equilibration time is also an important economic factor for the water treatment of polluted systems [38]. The results of the kinetic adsorption study of MB on green capped ZnS NPs are presented in ***Figure III.3***. The dye adsorption process on the AHA capped ZnS nanoparticles was fast for the first 5 min, then continued at a slower rate for 10–30 min, reaching equilibrium after approximately 45 min of the experiment. The experimental kinetics showed that using an AHA ligand increased the MB adsorption capacity. This can be explained by the small size of the robust adsorbents, which have a large surface-to-volume ratio and provide more sites on the surface. Hence, we could deduce that the new green synthesis has a progressive impact on the adsorption process with the improvement of the adsorption efficiency in addition to the eco-friendly criteria. The effect of the initial dye concentration depends on the immediate relation between the dye concentration and the available nano-adsorbent surface sites, as shown in ***Figure III.4***. The ability of the adsorbent goes up as the initial dye concentration goes up. This may be because the driving force for mass transfer is high when the initial dye concentration is high [39]. Experimental data exhibit an outstanding MB adsorption capacity on AHA-capped ZnS NPs, which varied from 9.54 to 29.92 mg/g when the dye concentration is raised from 10 to 50 mg/L, and it was assumed that *Artemisia Herba Alba* plant extract enhanced the adsorption process. However, another parameter is the temperature, which influences the adsorption

capacity of the adsorbent. A decrease in the adsorption process has been noted, and the results are given in ***Figure III.5***. A decline of adsorption capacity with an increase in temperature demonstrates that adsorption is an exothermic process. This may be attributed to the decline in the adsorptive forces between the dye species and the active sites on the adsorbent surface with a rise in temperature [40].

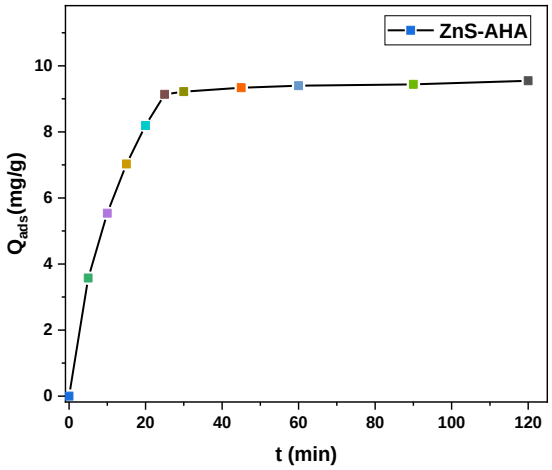


***Figure III.3***: Kinetic adsorption study of MB on green capped ZnS NPs.

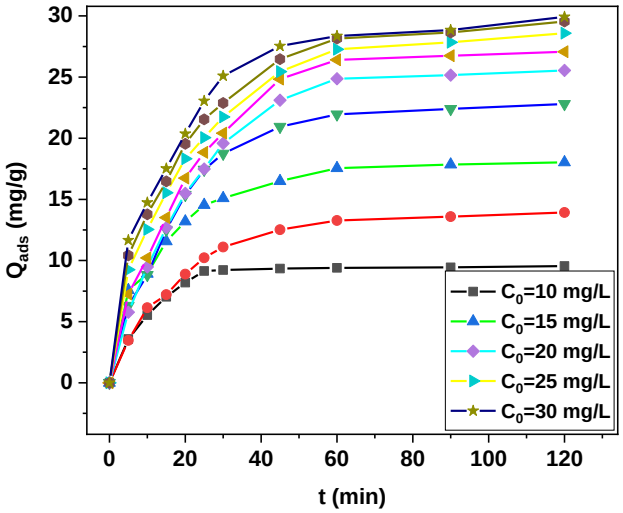


***Figure III.4***: Effect of initial dye concentration on the adsorption capacity AHA-capped ZnS NAs.

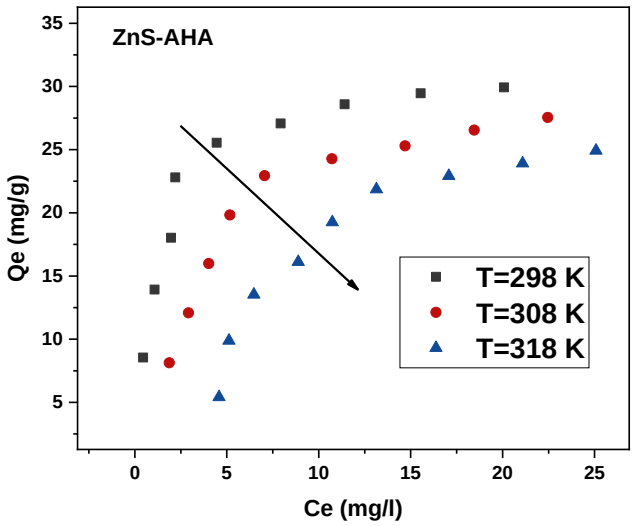


***Figure III.5***: Effect of Temperature on the adsorption of MB onto AHA-capped ZnS NPs.

### III.2.1 Adsorption kinetics

The kinetics studies on MB adsorption were conducted at 298 K. The pseudo-first-order (PFO) and the pseudo-second-order (PSO) models were applied to evaluate the MB adsorption kinetic data. The PFO kinetic model has been widely employed to predict the dye adsorption kinetics, which is given by the next formula [41]:

$$q\ (t) = q_e\ (1\text{-}exp(-K_1 t) \qquad (1)$$

Where q(t) and $q_e$ represent the amount of dye adsorbed (mg/g) at any time t and equilibrium, respectively, $K_1$ is the corresponding PFO adsorption rate constant ($min^{-1}$).

On the other side, the PSO kinetic model predicts that the rate-limiting step is chemisorption and this model is valid over the whole range of adsorption. The PSO kinetic rate equation is defined as follows [41] :

$$q(t) = \frac{q_e^2 k_2 t}{1+q_e K_2 t} \qquad (2)$$

Where $K_2$ (mg/g min) is the corresponding PSO rate adsorption constant. The best model for the adsorption kinetics study was chosen according to the $R^2$ value. The PFO model was the best alternative to describe the MB dye adsorption on ZnS-AHA NAs with $R^2$= (0.98-0.99) for all concentrations. The obtained results of adsorption kinetic modeling are reported in ***Figure III.6*** and ***Table III.1***. Adsorption rates ($K_1$) declined when the dye concentration raised because

of the competition of dye molecules with the available adsorption active sites [42]. ***Figure III. 6*** indicates that two different stages can be found in the kinetic profile. The first section of the curve corresponds to the diffusion of molecules on the NAs surface, which is generally the longest stage. The second stage corresponds to the adsorption equilibrium where the interaction between adsorbate and adsorbent surface takes place.

The adsorption capacity varied from 9.58 to 28.94 mg $g^{-1}$, when the dye concentration is increased from 10 to 50 mg/L, respectively. These values are close to the experimentally determined values from the adsorption isotherms. These high adsorption capacities are favored by the small particle size of ZnS-AHA NPs. The specific surface area of ZnS-AHA was found 36.82 $cm^2$ $g^{-1}$; this high specific surface area is a key factor to reach these adsorption capacities, which also contributes to a fast mass transfer gradient for the MB diffusion to the NPs surface [24].

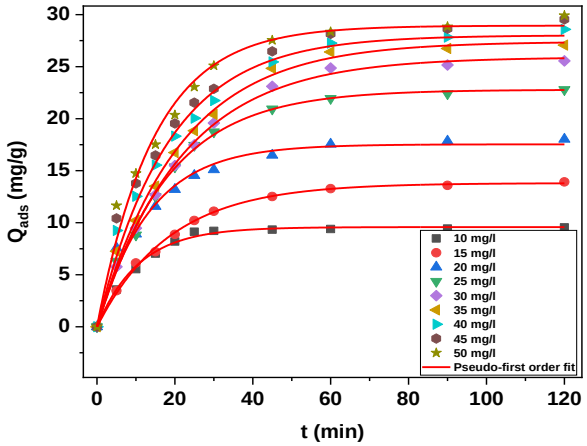


***Figure III.6***: Modeling of MB adsorption kinetic using the pseudo-first order.

***Table III.1*****:** Pseudo-first order kinetic parameters for the MB adsorption on ZnS-AHA NAs.

| Model | Pseudo-first order | | | | | | | | |
|---|---|---|---|---|---|---|---|---|---|
| C(mg/l) | 10 | 15 | 20 | 25 | 30 | 35 | 40 | 45 | 50 |
| K1 ($min^{-1}$) | 0.09 | 0.05 | 0.08 | 0.05 | 0.04 | 0.05 | 0.05 | 0.06 | 0.07 |
| qe (mg/g) | 9.58 | 13.81 | 17.47 | 22.77 | 25.97 | 27.40 | 28.01 | 28.69 | 28.94 |

### III.2.2 Dye adsorption isotherms

Adsorption isotherms are highly useful for understanding the mechanism of adsorption [43]. In general, adsorption isotherms provide information on the improvement of the adsorbents, a description of the affinity and the binding energy between adsorbate and adsorbent (whether or

not there are lateral interactions between molecules), and the adsorption capacity [44]. The isotherm also gives information on mode adsorption (monolayer or multilayer adsorption).

In this study, the effect of the initial concentration of MB on the amount adsorbed (mg/g) by ZnS-AHA NPs was studied in a range of initial concentrations (10-50 mg/L) for MB. The adsorption isotherms assessed at room temperature of 298 K are shown in ***Figure III.7***. According to Giles [45], The ZnS-AHA NPs adsorption isotherms show an L-form, indicating a relatively high affinity between adsorbate and adsorbent. The maximum equilibrium adsorption capacity value is 29.92 mg/g.

The equilibrium data of MB onto ZnS NPs was examinated using the most common Langmuir, Freundlich and Langmuir-Freundlich models to find out the suitable model that may be applied for the design and optimization of adsorption processes (see ***Figure III.7*** and ***Table III.2***). The best applicable model of those is chosen from the coefficient $R^2$ value ($0 < R^2 < 1$). The Langmuir isotherm states that adsorption takes place with the monolayer formation of adsorbate molecules on a homogeneous adsorbent surface with uniform adsorption energies [46]. This model is very useful for monomolecular adsorption of a solute by forming a single layer on the surface of an adsorbent; this model is used when the following conditions are completed: The adsorbed species is fixed on a single well-defined site, and each site can fix a single adsorbed species, the adsorption energy of all sites is identical and independent of other species already adsorbed at neighboring sites. The following equation represents this model [24]:

$$q_e = q_{max} \frac{K_L C_e}{1+K_L C_e} \quad (3)$$

where $q_e$ is the equilibrium adsorption capacity (mg/mg), *Ce* (mg/L) is the dye concentration in solution at adsorption equilibrium, $q_{max}$ (mg/g) is the maximum adsorption capacity of tested nano-adsorbents and $K_L$ (L/mg) is the Langmuir constant. On the other side, the Freundlich

model implies an heterogeneous adsorption surface having sites with different adsorption energies. It is mostly applied to the heterogeneous solid catalyst and is a mathematical relation used to describe multilayer adsorption. It is described as [24]:

$$q_e = k_f C_e^{1/n_F} \quad (4)$$

where $K_f$(mg/g) is the Freundlich adsorption constant and $n_F$ is the degree of nonlinearity between solution concentration and adsorption where, $1/n_F \in (0.1, 1)$ demonstrates favorable adsorption. In the end, the Langmuir -Freundlich (*L-F*) isotherm model is an equation based on the isotherms of Langmuir and Freundlich at the same time. It describes heterogeneous surfaces as well. The equation can be written as:

$$q_e = \frac{q_{max}(K_{LF}C_e)^{n_{LF}}}{1+(K_{LF}C_e)^{n_{LF}}} \quad (5)$$

where $q_{max}$(mg/g) is the maximum adsorption, the capacity of tested nano-adsorbents, $K_{LF}$ is the adsorption affinity constant and $n_{LF}$ is the heterogeneity index.

From the isothermal modeling results given in ***Table III.2***,

We find that Langmuir -Freundlich model describes better our experimental results, with $q_{max}$= 31.85 mg/g and $R^2$= 0.98. The Langmuir model shows that the surfaces of our samples are energy homogeneous and monomolecular adsorption of MB on our green NPs. On the other hand, Freundlich model $n_F$ values are greater than 1 ($n_F$ > 2.16) showing that adsorption is favorable and physical [42]. The maximum adsorption capacity calculated with the Langmuir-Freundlich model was 31.15 mg/g, which agreed with the experimental data of 29.92 mg/g and proves that the new robust green nano-adsorbents are good candidates for wastewater treatments.

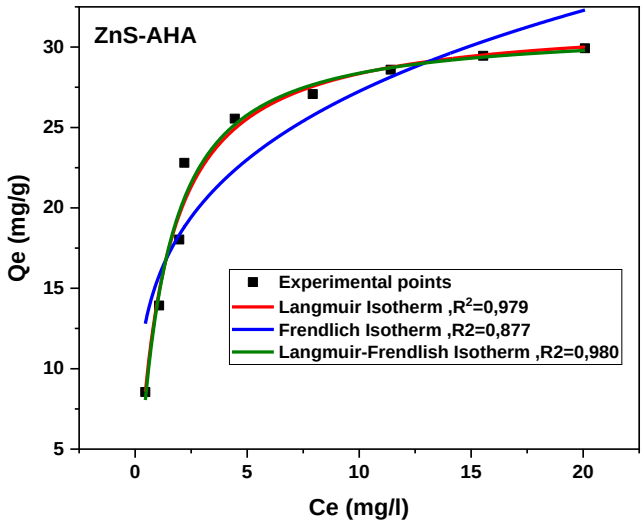


***Figure III.7***: The adsorption isotherms of MB dye using AHA-capped ZnS NPs.

***Table III.2*****:** Parameters of the isotherm models for the MB adsorption on ZnS-AHA NPs.

| | | |
|---|---|---|
| Langmuir isotherm ($R^2$ = 0.97) | | |
| $q_{max}$ (mg/g) | $K_L$ | |
| 31.8 | 0.80 | |
| Freundlich isotherm ($R^2$ = 0.86) | | |
| $K_f$ (mg/g) | $n_F$ | |
| 15.52 | 2.41 | |
| Langmuir-Freundlich ($R^2$ = 0.98) | | |
| $q_{max}$ (mg/g) | $K_{L-F}$ | m |
| 31.15 | 0.84 | 1.10 |

### III.2.3 Statistical physics modeling

A statistical physics model was applied for MB supplement adsorption analysis via the calculation of the following physicochemical parameters: the number of the adsorbed dye molecules per adsorption site ($n$), the density of adsorption sites ($D_M$) and the corresponding adsorption energies. A monolayer advanced model was used to clarify the adsorption isotherms of MB on the tested ZnS-AHA NPs. This model considered that MB dye molecule formed a monolayer on NPs surface. The formation of the layer of the adsorbed MB molecules resulted from the interactions between MB and NAs surface. This advanced model demonstrates that the main adsorption site in the green ZnS-AHA NPs could link a variable number of MB dye molecules (equal, inferior or superior to 1). This monolayer model is reported by equation 6 [24]:

$$q_e = \frac{nD_M}{1+\left(\frac{C_{\frac{1}{2}}}{C_e}\right)^n} \quad (6)$$

where $C_{1/2}$ is the concentration at half-saturation of MB on the ZnS-AHA NPs surface. Note that the calculation of adsorption energy via this model was performed with equation 6 [24]:

$$\Delta E^a_1 = R.T.\ln(\frac{C_s}{C_{1/2}}) \quad (7)$$

where $C_s$ is the MB dye molecule solubility (i.e., 40 g/L), $R$ is the universal ideal gas constant (8.314 x$10^{-3}$ kJ $K^{-1}$ $mol^{-1}$) and $T$ (K) is the absolute value of adsorption temperature. The estimated values for model parameters are summarized in ***Table III.3***, while the model fitting is given in ***Figure III.8***. It is noted that the parameter $n$ can be applied to describe the number of dye-adsorbed molecules per adsorption site and provides also details about the geometric adsorption position. Geometrically, the position of an adsorbate can be described according to the number of molecules per adsorption site of the tested material.

***Table III.3*** shows that $n$ = (1.08-2.25) indicates that MB dye molecules could be linked or adsorbed via a non-parallel orientation or inclined, with a multimolecular adsorption process [8]. MB molecules can interact with the adsorbent surface thus forming an aggregation process where the formation of MB dimmers in the solution and a multimolecular adsorption process ($n$ > 1) could be expected on the prepared nano-adsorbents. This multimolecular adsorption phenomenon usually occurs for dye molecules. The density of adsorption sites $D_M$ decreased with temperature 28.73 to 11.45 mg $g^{-1}$. Indeed, if the number of adsorbed MB dye molecules per adsorption site increased, the space in the ZnS-AHA nanoparticles surface reduced and, consequently, the number of adsorption sites available for dye removal became limited [24]. Note that a high $D_M$ value implies a high performance of the adsorbent because more adsorption

sites are available for the adsorption of the target pollutant [8]. The adsorption capacities at saturation ($Q_{sat}$) decreased as a function of the aqueous solution temperature from 31.17 mg $g^{-1}$ at 298 K to 25.49 mg $g^{-1}$ at 318 K, thus indicating exothermic adsorption.

The last parameter to be analyzed is the adsorption energy**.** This adsorption energy is expressed as a function of the concentration at half-saturation and the solubility of MB dye in water ($C_S$). All the adsorption energies that characterize the interactions between MB molecules and ZnS-AHA nano-adsorbent surface were estimated by modeling the experimental data through the Hill model, and they are summarized in ***Table III.3***. It is observed that the adsorption energies ranged from 25.82 to 21.58 kJ $mol^{-1}$, suggesting the presence of physical interactions between MB dye molecules and the ZnS-AHA nano-adsorbents surface. It could be expected that weak electrostatic forces and hydrogen-bond interactions were involved in the adsorption of MB molecules on the functional groups of the green ZnS-AHA nanoparticles. When comparing the capacity of adsorption of ZnS-AHA to that of other previously published ZnS nanoparticles (***Table III.4***), ZnS AHA present the higher capacity of adsorption, compared to naked ZnS NPs [47], to ZnS encapsulated with broccoli extract [48] and ZnS encapsulated with mercaptopropionic acid [24].

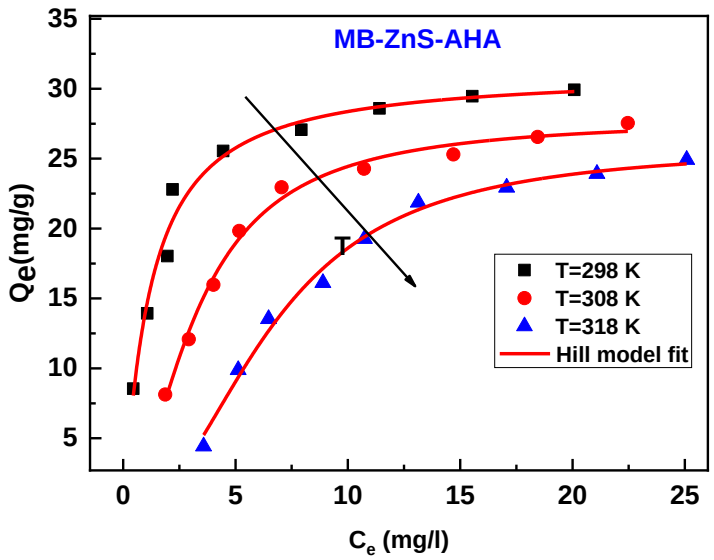


***Figure III.8***: Adsorption isotherm for statistical physics modeling of MB on ZnS-AHA

***Table III.3*****:** Parameters of the Hill model for the MB adsorption.

| T (K) | n | $D_M$ (mg/g) | $C_{1/2}$ (mg/L) | $Q_{sat}$ (mg/l) | $\Delta E_1^a$ (kJ/mol) |
|---|---|---|---|---|---|
| 298 | 1.08 | 28.73 | 1.19 | 31.17 | 25.82 |
| 308 | 1.75 | 15.94 | 3.25 | 27.85 | 23.33 |
| 318 | 2.25 | 11.45 | 6.58 | 25.49 | 21.58 |

***Table III.4***: Comparison of the adsorption capacity of various adsorbents with ZnS-AHA NPs towards MB dye.

| **Sr. No** | **Sample** | **Dye** | **Time (min)** | **$q_{max}$ (mg/g)** | **Ref. No** |
|---|---|---|---|---|---|
| 1 | ZnS-MPA | MB | 120 | 25.18 | [24] |
| 2 | ZnS | MB | 120 | 15.65 | [47] |
| 3 | ZnS-Broccoli | MB | 60 | 9.00 | [48] |
| 9 | ZnS-AHA | MB | 120 | 31.85 | Our work |

## III.3 Photocatalytic degradation of MB dye using ZnS-AHA NPs

### III.3.1 Degradation pathways

Photocatalytic degradation of MB dye using sunlight irradiation is a process that involves the use of ZnS nanocatalysts to initiate a chemical reaction in the presence of sunlight, which ultimately leads to the degradation of the dye molecule. Sunlight irradiation plays a crucial role in this process by providing the energy required for the photocatalytic reaction to occur. The energy from the sunlight excites the electrons in the photocatalyst material, which in turn react with the dye molecules to break them down. Preliminary experiments were carried out with MB solution in the absence of the ZnS nano-catalysts reveal that less than 10 % of dye were decomposed after 180 min of sunlight irradiation due to the $OH^*$ radicals coming from water or due to self-sensitization light of dye molecules, proving that MB molecules presents a good photostability. ***Figure III.9*** shows a series of UV-Vis absorption spectra for the methylene blue dye suspension in the presence of the AHA-capped ZnS NPs irradiated for 0, 10, 20, 30, 45, 60, 120 and 180 min. With increasing of the sunlight irradiation time, it was observed that a significant reduction in the absorption of the MB dye solution at the maximum peak at 664 nm due to the break of the azo groups ($C\text{-}S^+\text{=}C$) bond responsible for the blue color which indicates the decomposition of the MB chromophoric structure [10].

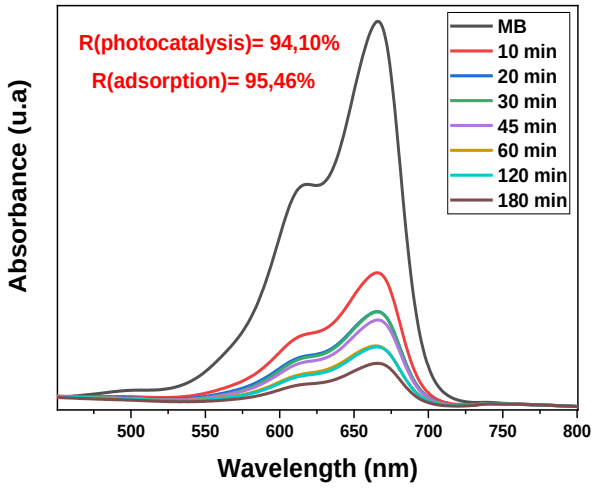


***Figure III.9***: Absorption spectral changes for the MB aqueous solution in the presence AHA capped ZnS NAs.

As a result, MB dye concentration decreased in the presence of the green ZnS-AHA NPs under sunlight irradiation until a full decolorization of the initial solution revealing that MB molecules were completely degraded. The degradation efficiency of AHA-capped ZnS NPs is given in ***Table III.5***. These results show a high degradation of MB dye using our synthesized NPs after 180 min of irradiation. We have recorded a rapid degradation of MB using the new plant extract-capped ZnS NPs leading to very effective decomposition in the first hour (89.18%). As a result, the new green nano-adsorbents demonstrated a fast and powerful degradation (94.09%) and which makes them a promising robust nanocatalysts for the dyes degradation. This high photodegradation activity can be explained by the reduction in electron-hole recombination [8]. In order to deduce kinetics from the degradation process, we calculated the effect of the irradiation time on the degradation using the normalized changes in the MB concentration (C/Co) and degradation efficiency (1- C/Co) for the nano-adsorbents represented in (***Figure III.10***). The intersection of these two curves indicated the half-life of the dye, which is the time reached to attend the MB half-concentration. The degradation performance is dependent on the high surface area of the crystal and morphology, which might enhance the number of photo-generated electron-hole pairs. Here, we suppose that *Artemisia Herba Alba* extract may influence the ZnS crystal growth with a high surface-to-volume ratio due to the small size of nanocrystals (4 nm) and subsequently high specific surface (36.82 $cm^2$ $g^{-1}$) which highly generate electron-hole pair at the conduction and valence band states under sunlight irradiation [30].In addition, another explanation is the ligand functional groups which is involved in the adsorption and the photocatalytic processes because *Artemisia Herba Alba* extract is plenty of

phenol, proteins and flavonoids groups which include reactive hydroxyl radicals. These highly reactive hydroxyls and superoxide radicals formed by interaction with the charge carrier to the surface of the nanoparticles can react with MB dye adsorbed on ZnS leading to its degradation [49]. As a result, the probability of adsorption of MB molecules on the surface of ZnS NAs will be increased with the use of AHA. In order to calculate the rate constant (k) and half time for MB degradation, we have used ***Eq.4*** and ***Figure III.10***; the summarized parameters are presented in ***Table III.5***.

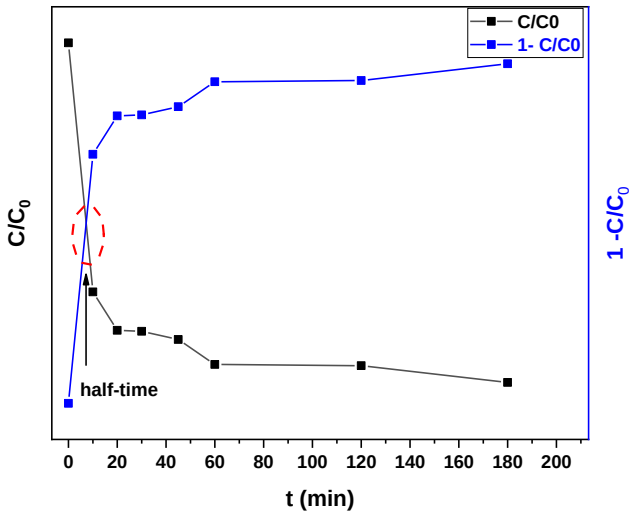


***Figure III.10***: C/Co curve and degradation efficiency (1-C/Co) for AHA capped ZnS NPs.

***Table III.5*****:** degradation efficiency of MB by ZnS-AHA NPs under sunlight irradiation.

| t (min) | 0 min | 10 min | 20 min | 30 min | 45 min | 60 min | 120 min | 180 min |
|---|---|---|---|---|---|---|---|---|
| % Degradation of MB | 0 | 69.27 | 79.81 | 79.90 | 82.27 | 89.18 | 89.63 | 94.09 |

The calculated rate constant (k) AHA-capped ZnS NPs were 0 0.012 $min^{-1}$. It is clear that the use of green ZnS-AHA nanocatalysts increases the photodegradation of the MB dye under sun-light which is confirmed by the small half-time value (7.41min). Finally, AHA-capped ZnS nanocatalysts showed a high photocatalytic performance due to the formation of NPs enriched with sulfur vacancies (Vs) and zinc interstitials ($I_{Zn}$) caused by stacking faults [24]. Therefore, as the plant extract-capped ZnS NPs present high defaults (dislocations, strain and stacking fault), this could facilitate the transfer of the photogenerated carriers by trapping the excited electrons and restraining the electron-hole recombination which increases the photocatalytic activity of these nano-adsorbents. This indicates that the ZnS capped with *Artemisia Herba*

*Alba* groups can be considered as a promising photocatalyst that can operate under sunlight for the environmental removal of organic pollutants. Moreover, the green molecules of the plant extract are eco-friendly that making AHA-capped ZnS a good candidate for further applications (antibacterial activity and gas sensor). Some values of maximum quantities found in the photodegradation of MB on some other ZnS nanoparticles are presented in ***Table III.7***. ZnS-AHA presents the higher degradation efficiency, nevertheless, its degradation rate constant is lower than that of ZnS NPs coated with Acalypha indica extract [18] and that of ZnS NPs with cubic phase [53].

***Table III.6***: Calculated parameters of photodegradation of MB in aqueous solution using ZnS-AHA NPs under sunlight irradiation.

| Nanocatalyst | Degradation rate constant $K$ ($min^{-1}$) | Half-time $t_{1/2}$ (min) | Degradation efficiency $\eta$ (%) |
|---|---|---|---|
| **ZnS-AHA** | 0.012 | 7.41 | 94.09 |

***Table III.7***: Comparison of the photocatalytic efficiency of various adsorbents with ZnS-AHA NPs towards MB dye.

| Sr. No | Sample | Dye | Irradiation | Time (min) | Degradation rate constant $K$ ($min^{-1}$) | Degradation efficiency (%) | Ref. No |
|---|---|---|---|---|---|---|---|
| 1 | ZnS-TGA | MB | Sunlight | 180 | 0.010 | 91.10 | [10] |
| 2 | ZnS-CHI | MB | UV light | 120 | ------- | 87.00 | [50] |
| 3 | ZnS-CC | MB | UV light | 120 | ------ | 96.00 | [51] |
| 4 | ZnS-S | MB | Visible light | 180 | ------ | 81.00 | [52] |
| 5 | ZnS-A | MB | UV light | 180 | 0.071 | 93.00 | [18] |
| 6 | ZnS | MB | Sunlight | 180 | 0.013 | 87.38 | [24] |
| 7 | ZnS | MB | Visible light | 120 | 0.020 | 78.41 | [53] |
| 9 | ZnS-AHA | MB | Sunlight | 180 | 0.012 | 94.09 | Our work |

To further explain the photocatalytic mechanism, a possible photocatalytic mechanism for degradation of MB dye by capped ZnS nanoparticles under sunlight irradiation has been proposed in ***Figure III.11***. The first step is summarized by the adsorption phase of the dye molecules on the NAs surface. When the ZnS semiconductor was irradiated by sunlight with energy higher than the band gap, an electron ($e^-$)/ hole ($h^+$) pair is generated where the electrons $e^-$ will transfer from the valence band (VB) to the conduction band (CB) and the holes $h^+$ will be located in VB. The formed $e^-$ and $h^+$ will migrate to the nano-adsorbents surface and react with electronic reactants such as adsorbed $O_2$ to produce a superoxide anion radical ($\mathbf{O_2^{*-}}$). The photo-induced holes can be trapped to produce hydroxyl radical species ($\mathbf{OH^*}$), which are assumed to be the

most essential and powerful oxidizing radical for dye degradation. In addition, intrinsic defects in the crystal structure (i.e., Vs, and $I_{Zn}$) act as intermediate energy states for the electrons inhibiting or delaying the rapid carrier recombination processes, which improves the separation of electron-hole pairs [54]. The active radical species ($OH^*$ and $O_2^{*-}$) can effectively degrade dye molecules to form intermediates like propionic acid and malonic acid with the final products ($CO_2$ and $H_2O$) [55]. An analogous effect may be expected from the charged functional groups of the plant extract and the organic-capping agent at the nano-interfaces with ZnS under irradiation. The main reactions that might be involved can be summarized as follows:

(a) Adsorption phase

$$ZnS\text{-}AHA + MB \rightarrow ZnS\text{-}AHA\text{-}MB \quad (8)$$

(a) $(e^-)$-$(h^+)$ pair generation

$$ZnS\text{-}AHA + h\nu \rightarrow e_{BC}^- + h_{BV}^+ \quad (9)$$

(b) Production of superoxide and hydroxyl radicals

$$e^- + O_2 \rightarrow O_2^{*-} \quad (10)$$

$$H_2O + h^+ \rightarrow OH^* + H^+ \quad (11)$$

$$h^+ + OH^- \rightarrow OH^* \quad (12)$$

(c) Degradation phase

$$O_2^{*-} + C_{16}H_{18}ClN_3S \rightarrow Intermediates + CO_2 + H_2O \quad (13)$$

$$OH^* + C_{16}H_{18}ClN_3S \rightarrow Intermediates + CO_2 + H_2O \quad (14)$$

It is noticeable that the hydroxyl radical plays a key role in the photocatalytic experiment for the degradation of MB dye. To prove the effect of these species on the degradation process photolysis experiments were carried out, which were based on sunlight irradiation without nanocatalysts. These preliminary experiments reveal that less than 10 % of dye were decomposed after 180 min of sunlight irradiation which demonstrates the importance of OH* and $O_2^{*-}$. These robust radicals found in high density in AHA-capped ZnS NPs arise from the phenols and flavonoids group of the extract plant. The hydroxyl radical starts to attack dye molecules from the C-S+=C bond and other bonds to degrade the MB dye. According to the photocatalytic experiment, the biological and organic-capped ZnS nanoparticles show enhanced photocatalytic activity for the degradation of MB dye.

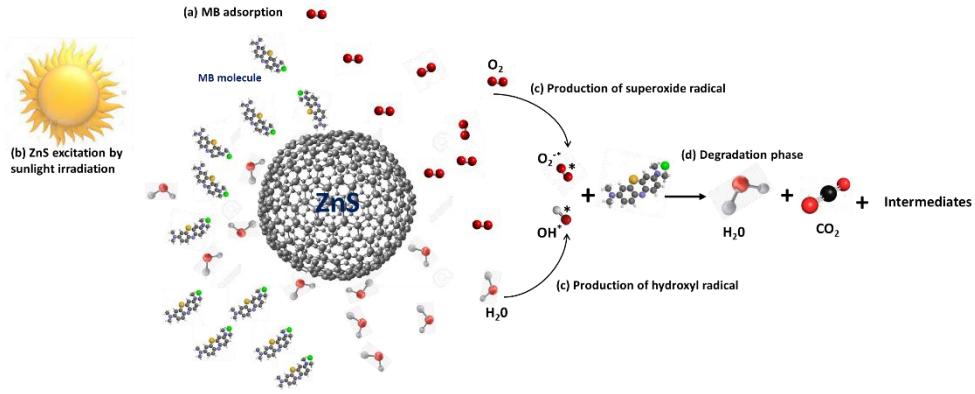


***Figure III.11***: Proposed MB dye degradation mechanism using capped-ZnS nano-adsorbents.

### III.3.2 Recycling of the ZnS-AHA photocatalysts

Reusability studies are an important tool for evaluating the long-term viability of materials and can help to take decisions about their use in a variety of applications. In this context, the photocatalytic stability of ZnS-AHA for MB degradation was thus studied. Repeatability experiments were conducted for 5 continuous cycles (***Figure III.12***). After each run, the catalysts were collected and rinsed a few times with deionized water and ethanol and dried at 100°C for 24 h before the beginning of the next cycle. Results reveal that the catalytic performance remains nearly unchanged and the degradation of MB is kept at 92 ± 2 % after 5 successive cycles. These provide clear evidence of high physiochemical and photocatalytic stability of as-synthesized nanoparticles. We have added the following reusability studies in the photocatalytic section.

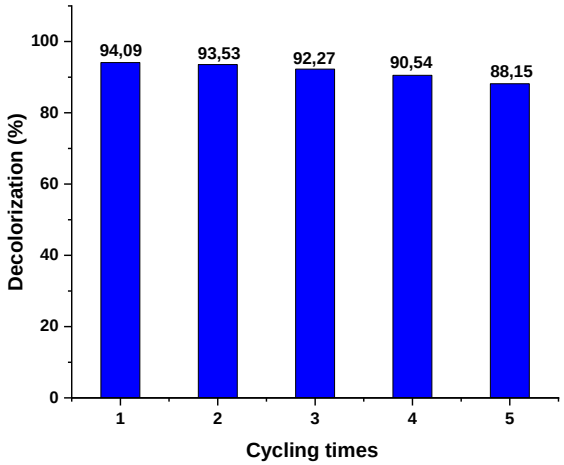


***Figure III.12***: Reusability of the ZnS-AHA nanocatalysts for the photodegradation of MB.

# IV. Conclusion

In summary, the present findings demonstrate that AHA-capped ZnS NPs synthesized via a stable, simple and colloidal route at room temperature. An innovative green method for preparing luminescent ZnS nano-photocatalysts was developed, for the first time, using *Artemisia Herba Alba*. FTIR results confirmed the functionalization of nano-adsorbents surface by AHA. XRD analysis indicated the formation of nanocrystals with an almost pure cubic phase. The average size of AHA-capped ZnS nanocrystals calculated by using the Debye-Scherrer formula and observed by HR-TEM was 4 nm. The optical absorption spectra showed the appearance of an absorption edge shifted towards short wavelengths compared to that of the solid-state semiconductor ZnS. PL spectroscopy indicated that no significant emission intensity was observed which clearly revealed that AHA ligands could play the same role as organic ligands for use in luminescence applications. Capped-ZnS NPs were used for MB removal under sunlight irradiation source from an aqueous colloidal solution to investigate the adsorption-photocatalysis synergy. Results showed spontaneous exothermic adsorption with an adsorption capacity of up to 29.92 mg/g. Adsorption isotherms and statistical physics calculations were used to analyze the steric and energetic parameters associated with MB adsorption on the surface of nano-adsorbents. The green ZnS nanoparticles showed a remarkable sunlight photocatalytic activity for MB dye with a conversion rate of 89.18 % in the first hour. ZnS-AHA nanoparticles exhibited high adsorption and photocatalytic capacity indicating that new plant extracts are a promising capping agent for potential eco-friendly and environmental applications.

# V. Supplementary Information

## V.1 Experimental details

Chemicals and reagents together with Artemisia Herba Alba plant extraction were demonstrated in the first section of the Supplementary Materials.

### V.1.1 Chemicals and Reagents

Analytical-grade chemicals were used from commercial sources without any further purification. Zinc (II) acetate dihydrate (Zn $[CH_3COO]_2.2H_2O \geq 98\%$), sodium sulfide ($Na_2S \geq 98\%$), and methylene blue dye ($C_{16}H_{18}ClN_3S \geq 50\%$, MW = 319,85 g/mol) were purchased from Sigma-Aldrich. Ultra-pure water (UPW) from the Millipore system was employed in all aqueous solutions (resistivity > 18 MOhm.com).

### V.1.2 Artemisia Herba Alba extraction

*Artemisia Herba Alba* (AHA) plants were collected from Tunisia. The selected leaves of AHA plants were washed with deionized water and then dried in the shade at room temperature and ground into powder. 11.5 g of powder was added to 200 mL of distilled water. The mixtures were boiled at 100 °C for 2h and filtered at room temperature. The filtered aqueous solution constitutes the extract of *A. herba alba*, which was used for ZnS nanoparticles fabrication in the present study. ***Figure III.S1*** shows a picture of *A. herba alba* leaves and their extract.


***Fig III.S1*****:** *Artemisia Herba Alba* plant and its extract.

### V.1.3 Synthesis of ZnS nanoparticles

The detailed preparation method of ZnS nanoparticles was reported elsewhere using the colloidal wet chemical route [10]. The green synthesis of the ZnS NPs was carried out employing *Artemisia Herba Alba* (AHA) extract as a complexing agent. In the typical synthesis process of AHA-capped ZnS NPs, 20 mL of AHA aqueous extract was mixed with 3 mM of $Zn[OOCCH_3]_2 \cdot 2H_2O$ solution (50 ml). The mixture was then agitated and degassed in the presence of $N_2$ for 30 min. In a second step, under stirring, 1.2 mM of $Na_2S$ solution (30 mL) were added to the solution containing Zn-AHA complexes at room temperature. Then, the mixture was heated under $N_2$ reflux at 100 °C for 3 h to obtain AHA-capped ZnS NPs. The final solution was allowed to cool down naturally at room temperature to stop the growth of NPs. The nanoparticles powder was separated by centrifugation for 20 min and washed with water and ethanol and then it was stored at room temperature to be used later in dye removal studies.

### V.1.4 Adsorbent characterization

Numerous techniques were used to characterize AHA-capped ZnS NPs. XRD measurements were carried out using Panalytical X' Pert Pro diffractometer with a CuKα radiation source (λ=1,542Å). Fourier transforms infrared (FTIR) spectrum were obtained in the transmission mode using a Perkin Elmer version 5.3 spectrophotometer in the spectral range of 400-4000 $cm^{-1}$ at room temperature using KBr pellet disks. High-resolution transmission electron

microscopy (HR-TEM) images were recorded using a JEM-2100 microscope operating at 200 kV and equipped with an Energy Dispersive X-ray (EDX) system for element chemical analysis. A drop of nanocrystal solution was poured on carbon-coated copper grids to obtain HR-TEM samples where the excess solvent was evaporated. The nanocrystal size and size-distribution data were collected based on the HR-TEM images by measuring at least 100 randomly selected nanocrystals using an image processing program (ImageJ, version 1.50). Absorbance spectra were registered using a SPECORD 210 Plus spectrophotometer in the range of 200-800 nm at room temperature with a quartz cuvette. Photoluminescence (PL) spectroscopy was used to study the defects and emission properties of the ZnS NAs using helium-cadmium laser as an exciting source of 325 nm.

### V.1.5 Dye adsorption experiments

Adsorption is the process by which molecules or particles adhere to the surface of a material or substrate. The study of the adsorption of MB on AHA capped ZnS nanoparticles involves investigating the interaction between the dye and the surface of the nanoparticles. This can be done by preparing a suspension of the nanoparticles and adding a known concentration of MB to it. The suspension is then stirred and allowed to equilibrate for a certain amount of time, after which the concentration of MB remaining in the solution is measured using UV-Vis spectrophotometer (SPECORD 210 Plus, Tunisia). All adsorption tests were performed with magnetic stirring in the dark.

The adsorption capacity of the nanoparticles can be determined by calculating the difference between the initial and final concentrations of MB in the solution. This information can be used to determine the effectiveness of the nanoparticles as an adsorbent for MB. Factors that can affect the adsorption of MB on AHA capped ZnS nanoparticles include the concentration of MB, the pH of the solution, the temperature, and the size and surface area of the nanoparticles. These parameters can be varied to optimize the adsorption capacity of the nanoparticles. To check the effect of these parameters, each one was tested individually by holding all the other variables fixed. Contact time (0-120 min), initial concentrations of MB (10-30 mg/L), adsorbent dose (0.1-2 g/L), different medium pH (5-9) and temperature range (298-318 K) were studied for finding the effect of these variables on the adsorption operation of ZnS nanoparticles in aqueous solutions. The MB adsorbed amount Qe (mg/g) as well as the percent dye removal efficiency (%) by the ZnS NPs can be expressed as [8]:

$$Q_e = \frac{(C_0 - C_e)V}{m} \quad \text{(S.1)}$$

$$Dye\ Adsorption\ efficiency\ (\%) = \frac{(C_0 - C_e)}{C_0} x\ 100 \quad \text{(S.2)}$$

where $C_0$ and $C_e$ are the initial and the equilibrium concentration of dye in the solution, in (mg/L), respectively, V is the volume of the MB solution in (mL), and m is the mass of the ZnS-AHA in (mg). The plot of equilibrium adsorption capacity $Q_e$ against equilibrium concentration $C_e$ in the liquid phase is graphically illustrated to determine the equilibrium isotherm.

Furthermore, the density ρ was calculated using the following expression [8]:

$$\rho = \frac{ZM}{N_A V} \quad \text{(S.3)}$$

Where $Z$ is the number of atoms per unit cell, $M$ (g $mol^{-1}$) is the molecular weight of the ZnS, $V$ is the volume of the unit cell ($cm^{-3}$) and $N_A$ is the Avogadro number. The specific surface area $S$ ($cm^2$ $g^{-1}$) of ZnS nanoparticles was calculated using the next equation [8]:

$$S = \frac{6}{\rho D} \quad \text{(S.4)}$$

Where $\rho$ (g $cm^{-1}$) and $D$ (nm) are the x-ray density of cubic or hexagonal nanoparticles and the average particle size, respectively.

### V.1.6 Photocatalytic degradation measurements

The photocatalytic performance of ZnS-AHA NPs was measured by the photodegradation of MB as model dye. The photocatalytic experiments were carried out at 300 K and pH 7 with the initial concentration and volume of 10 mg/L and 20 mL respectively in the presence of 20 mg ZnS NAs. At midday on a clear day in Tunisia, the intensity of sunlight at the Earth's surface is typically around 1000 watts per square meter ($W/m^2$). By contrast to sunlight, UV radiation represented only 5% (50 $Wm^{-2}$) of the total available solar flux received at the surface of the earth in the most favorable sunlight conditions [10]. After the adsorption phase (in the dark), the suspensions were submitted to sunlight irradiation between 11 am and 2 pm to rate the dye degradation. The photocatalytic activity was examined by monitoring the concentration in samples of 2 mL of the preparation suspension taken after filtration at different irradiation periods (0, 10, 20, 30, 45, 60, 120, 180 min). According to the Beer-Lambert law, the degradation performance was evaluated by measuring the optical absorption at the maximum absorption wavelength of MB at 664 [8]. The degradation efficiency and rate were calculated using the following equations [8]:

$$\eta = \frac{C_0 - C_t}{C_0} \text{ x } 100 \quad \text{(S.5)}$$

$$kt = Ln\left(\frac{C_0}{C_t}\right) \quad \text{(S.6)}$$

$$t_{1/2} = \frac{Ln(2)}{K} \quad \text{(S.7)}$$

Where $C_0, C$, are the concentrations $(mg/L)$ and $A_0$ and $A$ are the absorbances of MB dye solution before and after irradiation, respectively, at different times using the NPs. Note that K ($min^{-1}$) is the apparent reaction rate constant, which is calculated from of *Ln* ($C/C_0$) or *Ln* ($A/A_0$) versus *t*.

## V.2 Results and discussion

### V.2.1 ZnS-AHA Nanoparticles characterization

### V.2.2 Structural study of ZnS-AHA NPs

FTIR spectrometer was used to measure the vibrational frequencies of bonds in the molecules and to confirm the presence of different functional groups on the surface of ZnS nanoparticles (***Figure III.S2***). The absorption band at 540 $cm^{-1}$ was observed due to the Zn-S stretching vibrations [25]. The presence of Zn-S vibration clearly indicated that ZnS NPs were successfully formed. Absorption peak was observed at 3319 $cm^{-1}$ which is due to the alcohol/phenol group (-OH) stretching vibration [26]. The strong broad peak at 3665 $cm^{-1}$ is attributed to N-H stretching mode of the secondary amides coming particularly from the identified molecule dihydroxanthin of plant extract [27]. The peak at 2978 $cm^{-1}$ is probably ascribed to C-H alkane stretching, while the band at 2893 $cm^{-1}$ could be assigned to the C–H stretching branched alkene, particularly from the identified molecule cis-hydroxydavanone compound of AHA extract [27]. The peak at 1575 $cm^{-1}$ could be due to C=O carbonyl stretching group and the peak at 1057 $cm^{-1}$ was assigned to the stretching vibrations of primary alcohol groups in the AHA extracts [28]. Hence, these two peaks confirmed the presence of flavonoids or polyphenolic compounds in AHA-capped ZnS NPs [28]. The peaks at 1393 and 1259 $cm^{-1}$ corresponded to $CH_3$ and C-O stretching vibration coming mainly from the identified molecule vulgarin [27]. FTIR analysis evidenced that green nanoparticles were stabilized with the major phyto-constituents of AHA extract.

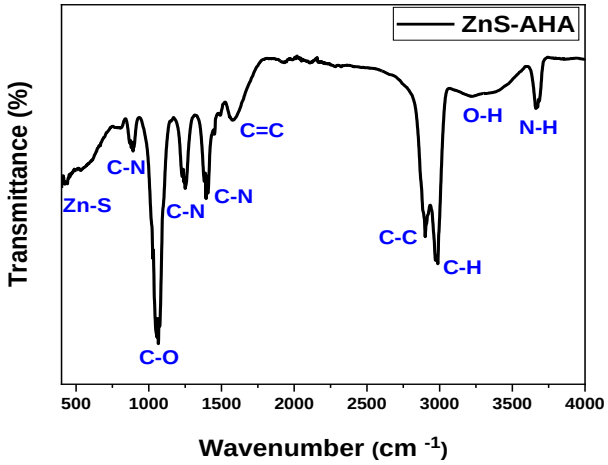


***Figure III.S2***: FTIR spectrum of AHA-capped ZnS nanoparticles.

The crystal structures of the as-synthesized ZnS nanoparticles prepared using AHA as a capping agent were studied by X-ray diffraction (XRD) and the obtained XRD patterns are shown in ***Figure III.S3***. The diffraction peaks are broadly confirming the nanometric size of the ZnS particles. For the phase identification, diffraction patterns of the ZnS were compared and analyzed using the diffraction standards of the wurtzite phase (JCPDS card No.80-0020) and zinc blend phase (JCPDS card No.80-0007). XRD patterns can be indexed as cubic zinc blende structure, and they appear in good agreement with JCPDS data card No. 80-0007 with prominent peaks corresponding to the reflections at (111) (220) and (311) planes. The non-appearance of diffraction peaks related to the wurtzite phase demonstrates that AHA capping favors the cubic structure. To better quantify the effect of the stabilizers, the size of the nanoparticles was estimated through the Scherrer formula [22]:

$$D = \frac{K\lambda}{\beta \cos(\theta)} \qquad \text{(S.8)}$$

Where $D$ is the average crystallite size (Å), $k$ = 0.9 is the Scherrer constant, $\lambda$ is the wavelength of X-ray (1.5402 Å) Cu Kα radiation, $\beta$ is the full width at half maximum of the diffraction peak (in radian) and $\theta$ is the Bragg diffraction angle, respectively. The estimated average size of the ZnS-AHA nanocrystals was found to be nearly equal to 4 nm. The smaller size of the ZnS crystallites encapsulated by AHA extract is most likely due to the strong interaction of AHA molecules with ZnS nanocrystals which makes the growth slower [29]. On the other hand, the lattice constant of the cubic phase of ZnS nanocrystals can be estimated using the following expressions:

$$d_{hkl}^2 = \frac{a_c^2}{h^2+k^2+l^2} \qquad \text{(S.9)}$$

Where $d_{hkl}$ is the inter-reticular distance for the cubic structure; *h*, *k*, and *l* are Miller indices; $\lambda$ is the wavelength of the X-ray radiation; $a_c$, *is* the lattice constant of the cubic phase of ZnS nanocrystals. The calculated average value of the lattice and the inter-reticular distance parameters of AHA ZnS nanocrystals was a= 5.4 Å and $d_{hkl}$=0.31 nm. It should be kept in mind that the Scherrer formula considers only the size effects coming from the diffraction results, and it then offers a lower limit for the nanocrystals size and neglects the micro-strain [30].

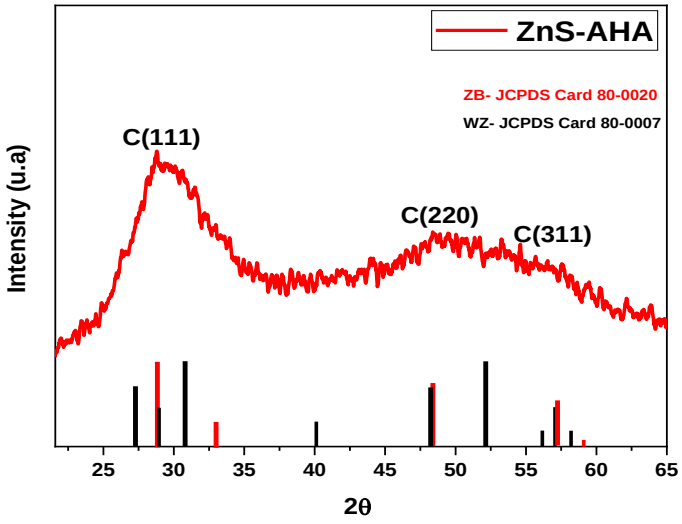


***Figure III.S3***: DRX patterns of AHA-capped ZnS nanocrystals.

***Figure III.S4a*** shows the HR-TEM images of the AHA-capped ZnS NPs, exhibiting a spherical shape, and their size distribution histogram. Their aggregation could be due to the high concentration of nanoparticles. The histogram of nanocrystals size distribution shows that the average crystal size is 4.3 ± 0.5 nm. These results are in good agreement with the XRD results. The d-spacing determined from the digital micrograph for ZnS is 0.30 nm, which is close to the spacing of (111) diffraction plane of the cubic phase [2]. Comparing the values calculated by Bragg law, it is evident that the growth of ZnS-AHA occurs preferentially along the direction [111]. NPs elemental composition was determined by EDX (***Figure III.S4b***). Zn and S are the major elemental components. The presence of C is related to the TEM grid and other peaks, Si and P, are probably due to residues coming from the synthesis and the grid.

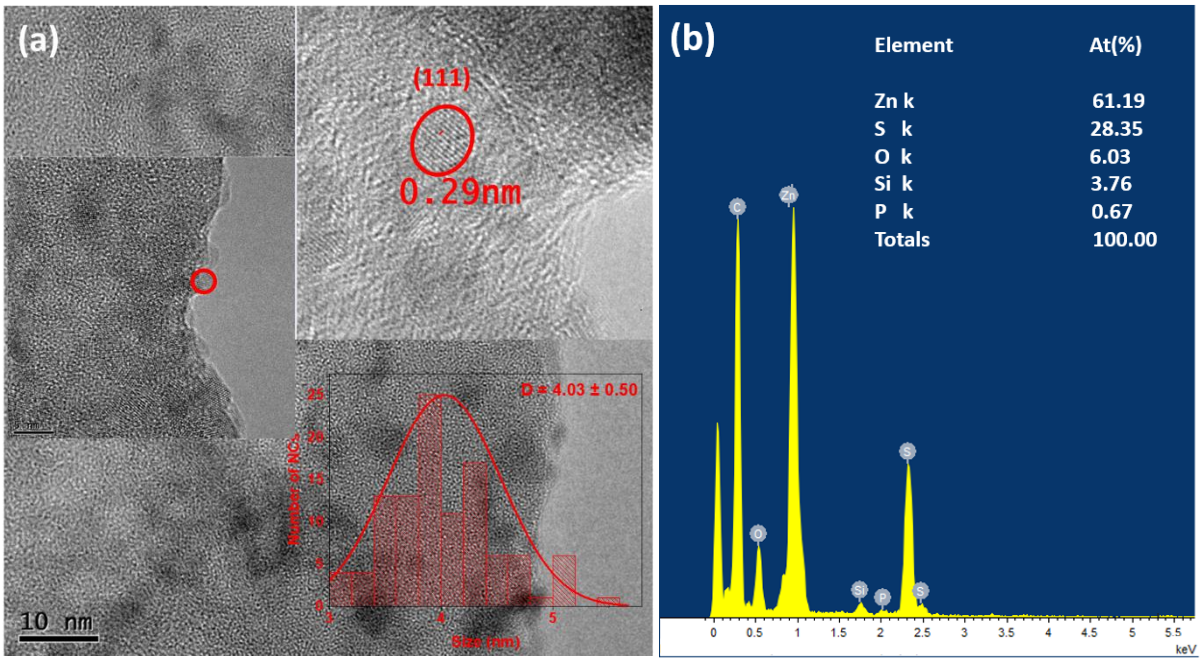


***Figure III.S4***: (a) HR-TEM images of ZnS-AHA nanocrystals with an inset showing the 0.29 nm lattice spacing that corresponded to the (111) plane and (b) EDX results.

### V.2.3 Optical study of ZnS-AHA NPs

In order to investigate the optical properties and the impact of ligand on the stability and size distribution of the nanoparticles, the optical absorption spectra of the ZnS NAs dispersed in water were recorded in (***Figure III.S5***). The UV-Visible absorption spectrum of ZnS NAs suspension shows an absorption band at 325 nm related to the first electronic transition $1S_e$-$1S_h$ [31]. The blue shift compared to bulk ZnS (344 nm, $E_g$ = 3.6 eV) is due to the quantum confinement of charge carriers due to the small particle size. This tendency is characteristic of semiconductors II-VI, mainly associated with the nanocrystals size distribution and sub-bandgap transitions arising from the intrinsic-extrinsic defect states. We have determined graphically the value of the optical and band-gap energy *Eg* using the following Tauc relation [32]:

$$\alpha h\nu = A\,(h\nu - Eg)^n \qquad \text{(S.10)}$$

optical gap energy of the capped ZnS NPs is obtained by extrapolating the plot of the function $(\alpha h\nu)^2$ to the value $\alpha = 0$. The intersection of the line with the horizontal axis gives the band gap energy value, (see insert in ***Figure III.S5***). The estimated band gap energy for the green ZnS is 3.70 eV. It is clear that the gap energy of these ZnS NPs shifts towards the blue, compared to that of the bulk ZnS ($E_g$ = 3.6 eV); this is due to the very small size of NPs, which induces a quantum confinement effect (QCE) [33].

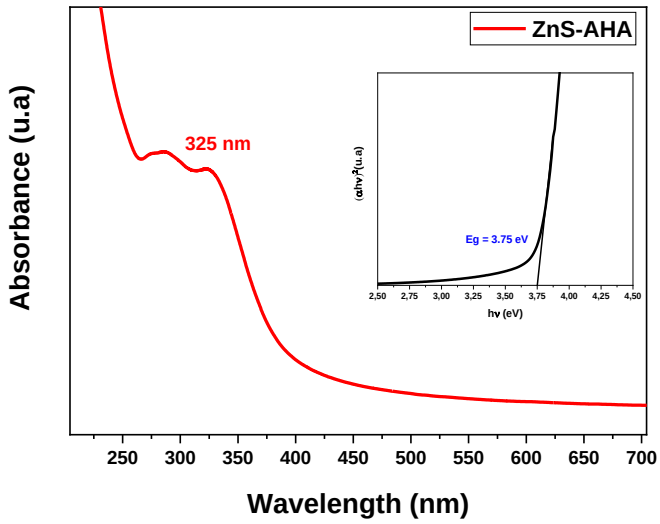


***Figure III.S5***: Absorption spectra for ZnS nanoparticles prepared with AHA plant extract. The determination of the energy band gap using Tauc Relation is shown in the inset.

***Figure III.S6*** shows the emission spectra of ZnS NPs obtained with an excitation wavelength $\lambda_{exc}$= 325 nm at room temperature. An intense and wide band centered at 450 nm dominates the spectrum. The emission spectra are deconvoluted using three Gaussian profiles associated with three main bands. The first band is less intense and has a spectral width of a few nm and is strongly correlated with the size of the nanoparticles. This band was attributed to the direct band-to-band recombination of excitons. The second emission band in the blue region (450 nm), which dominates the spectrum, was attributed to recombination between electrons and holes at the edges of conduction and valence bands respectively, or involves very shallow recombination centers (sulfur vacancies Vs) [33]. Finally, the green emission band (500 nm) was attributed to the interstitial zinc atom ($I_{Zn}$) [34]. The FWHM of the main emission band is equal to 62 nm which is related to the size dispersion of the ZnS-AHA NPs.

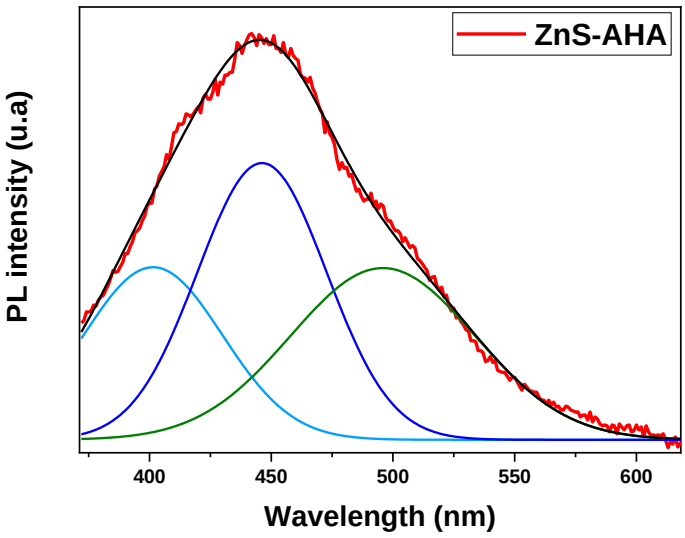


***Figure III.S6***: Gaussian fitting of PL spectra of AHA capped ZnS NPs.

# VI. References


[1] R. Mia, M. Selim, A.M. Shamim, M. Chowdhury, S. Sultana, M. Armin, M. Hossain, R. Akter, S. Dey, H. Naznin, Review on various types of pollution problem in textile dyeing & printing industries of Bangladesh and recommendation for mitigation, J. Text. Eng. Fash. Technol. 5 (2019). https://doi.org/10.15406/jteft.2019.05.00205.

[2] L. Yu, Y. Luo, The adsorption mechanism of anionic and cationic dyes by Jerusalem artichoke stalk-based mesoporous activated carbon, J. Environ. Chem. Eng. 2 (2014) 220–229. https://doi.org/10.1016/j.jece.2013.12.016.

[3] A.K. Kushwaha, N. Gupta, M.C. Chattopadhyaya, Removal of cationic methylene blue and malachite green dyes from aqueous solution by waste materials of Daucus carota, J. Saudi Chem. Soc. 18 (2014) 200–207. https://doi.org/10.1016/j.jscs.2011.06.011.

[4] G. Pérez, P. Gómez, I. Ortiz, A. Urtiaga, Techno-economic assessment of a membrane-based wastewater reclamation process, Desalination. 522 (2022) 115409. https://doi.org/10.1016/j.desal.2021.115409.

[5] C. Liu, H. Mao, J. Zheng, S. Zhang, Tight ultrafiltration membrane: Preparation and characterization of thermally resistant carboxylated cardo poly (arylene ether ketone)s (PAEK-COOH) tight ultrafiltration membrane for dye removal, J. Membr. Sci. 530 (2017) 1–10. https://doi.org/10.1016/j.memsci.2017.02.005.

[6] C. Ding, M. Yi, B. Liu, C. Han, X. Yu, Y. Wang, Forward osmosis-extraction hybrid process for resource recovery from dye wastewater, J. Membr. Sci. 612 (2020) 118376. https://doi.org/10.1016/j.memsci.2020.118376.

[7] X. Li, L. Fu, F. Chen, S. Zhao, J. Zhu, C. Yin, Application of Heterogeneous Catalytic Ozonation in Wastewater Treatment: An Overview, Catalysts. 13 (2023) 342. https://doi.org/10.3390/catal13020342.

[8] N. Mohamed, S. Ouni, B. Mohamed, M. Bouzidi, A. Bonilla-Petriciolet, M. Haouari, Synthesis and preparation of acid capped CdSe nanocrystals as successful adsorbent and photocatalyst for the removal of dyes from water and its statistical physics analysis, Environ. Sci. Pollut. Res. (2022). https://doi.org/10.1007/s11356-022-20990-9.

[9] S. Ouni, N.B.H. Mohamed, N. Chaaben, A. Bonilla-Petriciolet, M. Haouari, Fast and effective catalytic degradation of an organic dye by eco-friendly capped ZnS and Mn-doped ZnS nanocrystals, Environ. Sci. Pollut. Res. 29 (2022) 33474–33494. https://doi.org/10.1007/s11356-021-17860-1.

[10] S. Ouni, N. Mohamed, M. Bouzidi, A. Bonilla-Petriciolet, M. Haouari, High impact of thiol capped ZnS nanocrystals on the degradation of single and binary aqueous solutions of industrial azo dyes under sunlight, J. Environ. Chem. Eng. 9 (2021) 105915. https://doi.org/10.1016/j.jece.2021.105915.

[11] B. Sarangi, S.P. Mishra, N. Behera, Advances in green synthesis of ZnS nanoparticles: An overview, Mater. Sci. Semicond. Process. 147 (2022) 106723. https://doi.org/10.1016/j.mssp.2022.106723.

[12] R. Chaudhary, K. Nawaz, A.K. Khan, C. Hano, B.H. Abbasi, S. Anjum, An Overview of the Algae-Mediated Biosynthesis of Nanoparticles and Their Biomedical Applications, Biomolecules. 10 (2020) 1498. https://doi.org/10.3390/biom10111498.

[13] F.C. Christopher, S.K. Ponnusamy, J.J. Ganesan, R. Ramamurthy, Investigating the prospects of bacterial biosurfactants for metal nanoparticle synthesis – a comprehensive review, IET Nanobiotechnol. 13 (2019) 243–249. https://doi.org/10.1049/iet-nbt.2018.5184.

[14] A. Yadav, K. Kon, G. Kratosova, N. Duran, A.P. Ingle, M. Rai, Fungi as an efficient mycosystem for the synthesis of metal nanoparticles: progress and key aspects of research, Biotechnol. Lett. 37 (2015) 2099–2120. https://doi.org/10.1007/s10529-015-1901-6.

[15] S. Munyai, L.M. Mahlaule-Glory, N.C. Hintsho-Mbita, Green synthesis of Zinc sulphide (ZnS) nanostructures using S. frutescences plant extract for photocatalytic degradation of dyes and antibiotics, Mater. Res. Express. 9 (2022) 015001. https://doi.org/10.1088/2053-1591/ac4409.

[16] A. El Nady, R.N. Abbas, N.M. Sorour, Biomediated nanosized ZnS using Ulva fasciata and Citrus japonica: A new bio-photocatalyst for textile wastewater treatment, Rendiconti Lincei Sci. Fis. E Nat. 33 (2022) 537–553. https://doi.org/10.1007/s12210-022-01076-7.

[17] H.R. Rajabi, F. Sajadiasl, H. Karimi, Z.M. Alvand, Green synthesis of zinc sulfide nanophotocatalysts using aqueous extract of Ficus Johannis plant for efficient photodegradation of some pollutants, J. Mater. Res. Technol. 9 (2020) 15638–15647. https://doi.org/10.1016/j.jmrt.2020.11.017.

[18] S. Kannan, N.P. Subiramaniyam, M. Sathishkumar, A novel green synthesis approach for improved photocatalytic activity and antibacterial properties of zinc sulfide nanoparticles using plant extract of Acalypha indica and Tridax procumbens, J. Mater. Sci. Mater. Electron. 31 (2020) 9846–9859. https://doi.org/10.1007/s10854-020-03529-x.

[19] S. Simon, N.R.S. Sibuyi, A.O. Fadaka, S. Meyer, J. Josephs, M.O. Onani, M. Meyer, A.M. Madiehe, Biomedical Applications of Plant Extract-Synthesized Silver Nanoparticles, Biomedicines. 10 (2022) 2792. https://doi.org/10.3390/biomedicines10112792.

[20] R. Belhattab, L. Amor, J.G. Barroso, L.G. Pedro, A. Cristina Figueiredo, Essential oil from Artemisia herba-alba Asso grown wild in Algeria: Variability assessment and comparison with an updated literature survey, Arab. J. Chem. 7 (2014) 243–251. https://doi.org/10.1016/j.arabjc.2012.04.042.

[21] H. Ekiert, M. Klimek-Szczykutowicz, A. Rzepiela, P. Klin, A. Szopa, Artemisia Species with High Biological Values as a Potential Source of Medicinal and Cosmetic Raw Materials, Molecules. 27 (2022) 6427. https://doi.org/10.3390/molecules27196427.

[22] M. Adoni, M. Yadam, S. Gaddam, R. Usha, V.S. Kotakadi, Antimicrobial, Antioxidant, and Dye Degradation Properties of Biosynthesized Silver Nanoparticles From Artemisia Annua L, Lett. Appl. NanoBioScience. 10 (2021) 1981–1992. https://doi.org/10.33263/LIANBS101.19811992.

[23] I. Khan, K. Saeed, I. Zekker, B. Zhang, A.H. Hendi, A. Ahmad, S. Ahmad, N. Zada, H. Ahmad, L.A. Shah, T. Shah, I. Khan, Review on Methylene Blue: Its Properties, Uses, Toxicity and Photodegradation, Water. 14 (2022) 242. https://doi.org/10.3390/w14020242.

[24] N. Bel Haj Mohamed, M. Bouzidi, S. Ouni, A.S. Alshammari, Z.R. Khan, M. Gandouzi, M. Mohamed, N. Chaaben, A. Bonilla-Petriciolet, M. Haouari, Statistical physics analysis of adsorption isotherms and photocatalysis activity of MPA coated $CuInS_2$/ZnS nanocrystals for the removal of methyl blue from wastewaters, Inorg. Chem. Commun. 144 (2022) 109933. https://doi.org/10.1016/j.inoche.2022.109933.

[25] D. Amaranatha Reddy, C. Liu, R.P. Vijayalakshmi, B.K. Reddy (2014) Effect of Al doping on the structural, optical and photoluminescence properties of ZnS nanoparticles, J. Alloys Compd. 582: 257–264. https://doi.org/10.1016/j.jallcom.2013.08.051

[26] H. Asoufi, T. Al-Antary, A. Awwad (2018) biosynthesis and characterization of iron sulfide (FeS) nanoparticles and evaluation their aphicidal activity on the green peach aphid myzus persicae (Homoptera: aphididae), Fresenius Environ. Bull. 27: 7767–7775.

[27] Q.F. Nafa, S.M. Hussin, W.F. Hamadi (2021) Characterization of some active organic compound from Cold and Hot aqueous solvent and Study their Antibiotic of Artemisia herba-alba Asso plant oil, Egypt. J. Chem. 64: 6691–6709. https://doi.org/10.21608/ejchem.2021.72074.3587

[28] U.S. Senapati, D. Sarkar, Structural (2015) spectral and electrical properties of green synthesized ZnS nanoparticles using Elaeocarpus floribundus leaf extract, J. Mater. Sci. Mater. Electron. 26: 5783–5791. https://doi.org/10.1007/s10854-015-3137-6

[29] Y. Yu, L. Xu, J. Chen, H. Gao, S. Wang, J. Fang, S. Xu (2012) Hydrothermal synthesis of GSH–TGA co-capped CdTe quantum dots and their application in labeling colorectal cancer cells, Colloids Surf. B Biointerfaces. 95: 247–253. https://doi.org/10.1016/j.colsurfb.2012.03.011

[30] M. Jothibas, C. Manoharan, S. Johnson Jeyakumar, P. Praveen, I. Kartharinal Punithavathy, J. Prince Richard (2018) Synthesis and enhanced photocatalytic property of Ni doped ZnS nanoparticles, Sol. Energy. 159: 434–443. https://doi.org/10.1016/j.solener.2017.10.055

[31] V. Mote, Y. Purushotham, B. Dole (2012) Williamson-Hall analysis in estimation of lattice strain in nanometer-sized ZnO particles, J. Theor. Appl. Phys. 6: 6. https://doi.org/10.1186/2251-7235-6-6

[32] H. Matsumoto, T. Sakata, H. Mori, H. Yoneyama (1996) Preparation of Monodisperse CdS Nanocrystals by Size Selective Photocorrosion, J. Phys. Chem. 100: 13781–13785. https://doi.org/10.1021/jp960834x

[33] N. Ben Brahim, M. Poggi, N.B. Haj Mohamed, R. Ben Chaâbane, M. Haouari, M. Negrerie, H. Ben Ouada (2016) Synthesis, characterization and spectral temperature-dependence of thioglycerol-CdSe nanocrystals, J. Lumin. 177: 402–408. https://doi.org/10.1016/j.jlumin.2016.05.026

[34] Y. Piña-Pérez, O. Aguilar-Martínez, P. Acevedo-Peña, C.E. Santolalla-Vargas, S. Oros-Ruíz, F. Galindo-Hernández, R. Gómez, F. Tzompantzi (2018) Novel ZnS-ZnO composite synthesized by the solvothermal method through the partial sulfidation of ZnO for $H_2$ production without sacrificial agent, Appl. Catal. B Environ. 230: 125–134. https://doi.org/10.1016/j.apcatb.2018.02.047

[35] P.K. Jaseela, J. Garvasis, A. Joseph (2019) Selective adsorption of methylene blue (MB) dye from aqueous mixture of MB and methyl orange (MO) using mesoporous titania ($TiO_2$) – poly vinyl alcohol (PVA) nanocomposite, J. Mol. Liq. 286: 110908. https://doi.org/10.1016/j.molliq.2019.110908

[36] B.H. Hameed (2009) Evaluation of papaya seeds as a novel non-conventional low-cost adsorbent for removal of methylene blue, J. Hazard. Mater. 162: 939–944. https://doi.org/10.1016/j.jhazmat.2008.05.120

[37] M. Arshadi, F. SalimiVahid, J.W.L. Salvacion, M. Soleymanzadeh (2014) Adsorption studies of methyl orange on an immobilized Mn-nanoparticle: kinetic and thermodynamic, RSC Adv. 4: 16005–16017. https://doi.org/10.1039/C3RA47756H

[38] M. Ghaedi, H. Hossainian, M. Montazerozohori, A. Shokrollahi, F. Shojaipour, M. Soylak, M.K. Purkait (2011) novel acorn-based adsorbent for the removal of brilliant green, Desalination. 281: 226-233. https://doi.org/10.1016/j.desal.2011.07.068

[39] Y. Bulut, H. Aydın (2006) A kinetics and thermodynamics study of methylene blue adsorption on wheat shells, Desalination. 194: 259–267. https://doi.org/10.1016/j.desal.2005.10.032

[40] H. Khojasteh, M. Salavati-Niasari, A. Abbasi, F. Azizi, M. Enhessari, Synthesis (2016) characterization and photocatalytic activity of $PdO/TiO_2$ and $Pd/TiO_2$ nanocomposites, J. Mater. Sci. Mater. Electron. 27: 1261–1269. https://doi.org/10.1007/s10854-015-3884-4

[41] M. Ghasemi, N. Ghasemi, G. Zahedi, S.R.W. Alwi, M. Goodarzi, H. Javadian (2014) Kinetic and equilibrium study of Ni(II) sorption from aqueous solutions onto Peganum harmala-L, Int. J. Environ. Sci. Technol. 11: 1835–1844. https://doi.org/10.1007/s13762-014-0617-9

[42] S. Dawood, T.K. Sen (2012) Removal of anionic dye Congo red from aqueous solution by raw pine and acid-treated pinecone powder as adsorbent: Equilibrium, thermodynamic, kinetics, mechanism and process design, Water Res. 46: 1933–1946. https://doi.org/10.1016/j.watres.2012.01.009

[43] P. Luo, Y. Zhao, B. Zhang, J. Liu, Y. Yang, J. Liu (2010) Study on the adsorption of Neutral Red from aqueous solution onto halloysite nanotubes, Water Res. 44: 1489–1497. https://doi.org/10.1016/j.watres.2009.10.042

[44] Q. Hu, Z. Xu, S. Qiao, F. Haghseresht, M. Wilson, G.Q. Lu (2007) A novel color removal adsorbent from heterocoagulation of cationic and anionic clays, J. Colloid Interface Sci. 308: 191–199. https://doi.org/10.1016/j.jcis.2006.12.052

[45] C.H. Giles, D. Smith, A. Huitson (1974) A general treatment and classification of the solute adsorption isotherm. I. Theoretical, J. Colloid Interface Sci. 47: 755–765. https://doi.org/10.1016/0021-9797(74)90252-5

[46] I. Langmuir (1918) The adsorption of gases on plane surfaces of glass, mica and platinum, J. Am. Chem. Soc. 40, 1361-1403. https://doi.org/10.1021/ja02242a004

[47] X. Liu,X. Zhang, Y. Liu,M. Liu,X. Miao,Y. Wang (2022) Influence of ZnS crystal morphology on adsorption-photocatalytic efficiency of pseudocrystal ZnS nanomaterials for methylene blue degradation, J. Mol. Struct.1256:132514-132524. https://doi.org/10.1016/j.molstruc.2022.132514

[48] A. Q. Abed , A. M. Al Hindawi , H. F. Alesary (2022) Green Synthesis of Zinc Sulfide Nanoparticles for the Removal of Methylene Blue Dye from Aqueous Solution, Nanoworld J.8:79-84. http://doi.org/10.17756/nwj.2022-103.

[49] C. Lu, C. Liu, R. Chen, X. Fang, K. Xu, D. Meng (2016) Synthesis and characterization of ZnO/ZnS/CuS ternary nanocomposites as high efficient photocatalyst in visible light, J. Mater. Sci. Mater. Electron. 27: 6947–6954. https://doi.org/10.1007/s10854-016-4649-4

[50] A. A.P. Mansura, H. S. Mansura, F. P. Ramanerya, L. Carlos Oliveirab, P. P. Souza (2014) “Green” colloidal ZnS quantum dots/chitosan nano-photocatalysts for advanced oxidation processes: Study of the photodegradation oforganic dye pollutants, Appl. Catal. 158–159 (2014) 269–279. https://doi.org/10.1016/j.apcatb.2014.04.026

[51] J. Chen, B. Hu, J. Zhi (2015) Optical and photocatalytic properties of Corymbia citriodora leaf extract synthesized ZnS nanoparticles, Physica E Low Dimens. Syst. 79 :103-106. https://doi.org/10.1016/j.physe.2015.12.015

[52] S. k. Mani, S. Manickam, V. Muthusamy, R. Thangaraj (2018) Antimicrobial Activity and Photocatalytic Degradation Properties of Zinc Sulfide Nanoparticles Synthesized by Using Plant Extracts, J Nanostruct 8(2): 107-118.

[53] Z. Ye, L. Kong, F. Chen, Z. Chen, Y. Lin, C. Liu (2018) A comparative study of photocatalytic activity of ZnS photocatalyst for degradation of various dyes, Optik. 164: 345–354. https://doi.org/10.1016/j.ijleo.2018.03.030

[54] A.A.P. Mansur, H.S. Mansur, F.P. Ramanery, L.C. Oliveira, P.P. Souza (2014) “Green” colloidal ZnS quantum dots/chitosan nano-photocatalysts for advanced oxidation processes: Study of the photodegradation of organic dye pollutants, Appl. Catal. B Environ. 158–159: 269–279. https://doi.org/10.1016/j.apcatb.2014.04.026

[55] J. Lin, Z. Luo, J. Liu, P. Li (2018) Photocatalytic degradation of methylene blue in aqueous solution by using ZnO-$SnO_2$ nanocomposites, Mater. Sci. Semicond. Process. 87: 24–31. https://doi.org/10.1016/j.mssp.2018.07.003

# *Chapitre IV*

## *A novel conductometric micro-sensor for methanol detection based on chitosan/zinc sulfide-nanoparticles composite obtained by green synthesis*

## Résumé

Un transducteur microconductométrique est proposé pour la détection de vapeur de méthanol. La partie sensible de ce microcapteur de méthanol est préparée par l'encapsulation des nanoparticules de sulfure de zinc (ZnS) dans le chitosane. Les NPs de ZnS ont été préparées par une voie colloïdale aqueuse et l'extrait de plante d'Artemisia Herba Alba (AHA) étant utilisé comme agent de capsulage. Ces nanoparticules de ZnS ont été largement caractérisées, et les résultats ont démontré que les molécules d'AHA étaient des ligands de capsulage efficaces pour produire directement une dispersion aqueuse des NPs de ZnS avec une taille moyenne de nanocristaux de 3,93 nm. Un film mince de chitosane/ZnS-NPs composite a été électrodéposé sur les électrodes d'or interdigitées par chronoampérometrie. Les réponses des films à l'éthanol, au méthanol et à l'acétone ont été mesurées à température ambiante, par des mesures conductimétriques différentielles à 10 kHz. Le temps de réponse des catalyseurs ($t_{Rep}$) pour le méthanol est de 11 à 25 s entre les concentrations inférieures et supérieures. La limite de détection du méthanol est de 1400 ppm en phase gazeuse. Le capteur de méthanol présente une sensibilité 3,8 fois inférieure pour l'éthanol et 30 fois inférieure pour l'acétone. La durée de conservation du capteur de méthanol est d'un mois.

# *A novel conductometric micro-sensor for methanol detection based on chitosan/zinc sulfide-nanoparticles composite obtained by green synthesis*


## Abstract

A microconductometric transducer is proposed for the detection of methanol vapor. The sensitive part of this methanol microsensor is prepared by the encapsulation of zinc sulfide (ZnS) nanoparticles (NPs) in chitosan. ZnS NPs were prepared through an aqueous colloidal route, *Artemisia Herba Alba* (AHA) plant extract being used as a capping agent. These capped ZnS nanoparticles (NPs) were widely characterized, and the results demonstrated that AHA were effective capping ligands for directly producing an aqueous dispersion of ZnS NPs with an average nanocrystal size of 3.93 nm. A thin film of chitosan/ZnS-NPs composite was electrodeposited on the interdigitated gold electrodes through chronoamperometry. The ethanol, methanol and Acetone gas-sensing responses of the films were measured at room temperature, through differential conductometric measurements at 10 kHz. The sensors' response time ($t_{Res}$) for methanol is from 11 to 25 s from lower to higher concentrations. The limit of detection for methanol is 1400 ppm in the gas phase. The methanol sensor presents 3.8 times lower sensitivity for ethanol and 30 times lower sensitivity for acetone. The shelf life of the methanol sensor is one month.



***Keywords***: Chitosan film; ZnS nanoparticles; Artemisia Herba Alba extract; conductivity; methanol; gas sensor.


## I. Introduction

Methanol, the simplest alcohol, is harmless on its own, but its metabolites formic acid and formate are very hazardous after ingestion [1, 2]. It is well known that consuming MeOH may harm the neurological and circulatory systems permanently, leading to blindness, organ failure, or even death. It can be found in alcoholic drinks made by distillation or spontaneous fermentation. Blindness cases have been documented following the ingestion of as little as 4 mL of MeOH. It is often stated that 100 mL of consumed MeOH is the least deadly dosage [1]. MeOH is often employed as a cleaning agent and solvent in industry, and it is an alternate energy carrier to hydrogen [3]. For repeated exposure during the working day without experiencing serious health consequences. It is thus necessary to create assays and sensors that are sensitive, reasonably priced, and easy to use for industrial laboratories, suppliers, and end users. MeOH has been identified using a variety of methods, such as gas chromatography [4], Fourier transform infra-

red spectrometry [5], Raman spectroscopy [6], and surface plasmon resonance [7]. These methods are not suited for routine usage because of their limitations, which include high costs and the requirement for skilled personnel. To address the issue, a gas sensor approach has been used to detect MeOH or other volatile organic chemicals (VOCs). Numerous sensors are based on semiconducting metal oxides such as SnO2 [8, 9], ZnO [10, 11], WO3 [12]. The main drawbacks of these nanomaterials are their high working temperature and their rather poor specificity. Metal sulfides as sensing materials for gas detection have been poorly studied. By studying physical and chemical properties of nanostructured metal sulfides, it arose that such materials may be very good candidates to be further investigated in the chemoresistive gas sensing field. Indeed, by using these materials, we expect an improvement from an energy consumption point of view, both in thermal and photo-activation modes, due to their lower bandgap than for metal-oxide semiconductors [13]. The comparison between CdO and CdS, for the detection of 5 ppm ethanol, carried out at the relative best working temperature (300 °C) for both sensing materials, highlights the negligible response of CdO with respect to CdS. The response of SnS2 sensor for 2500 ppm of methane was higher than the SnO2 one, and the response/recovery times of SnS2 were faster than $SnO_2$ [13]. The detection of methanol, ethanol and acetone was tested on different thicknesses of $In_2S_3$, in the range 2000 ppm to 10,000 ppm (for methanol), at a working temperature of 350 °C. A higher sensitivity was observed for ethanol [14]. SnS was able to detect ethanol in the range 14.86 ppm to 100 ppm at 160 °C [15]. Some published gas sensors were based on ZnS nanoparticles, working as chemoresistors under thermoactivation. A study reports the ZnS quantum dots (QDs) synthesis by a hot-injection method for acetone gas sensing applications. This sensor was highly selective to acetone, at 175 °C, in the range of 20 ppm to 100 ppm [16]. Novel Au nanoparticles decorated wurtzite ZnS hollow spheres (Au NPs-ZnS HSs) were successfully synthesized by simple hydrothermal and deposition–precipitation methods. The obtained chemoresistive sensor was used at 260 °C for the detection of ethanol, n-propanol and n-butanol for 50 ppm concentration [17]. ZnS NPs have recently drawn special attention because of their abundance, low cost, good stability, non-toxicity, physical and chemical stability, good light UV absorption, and high catalytic efficiency [18–20]. Several chemical and physical methods are widely used to elaborate ZnS NPs like pulsed laser deposition [21], solvothermal [22], sol–gel [23] and hydrothermal [24]. Researchers have eveloped a new approach to synthesize functionalized ZnS NPs using capping agents. These surface capping agents bind on the surface of the nan particles and provide colloidal stability, passivation of surface defects, and water solubility [25]. Among the capping agents most often used, we can cite layers of organic thiol ligands such as mercaptopropionic acid [26], β-mercaptoethanol

[27], thioglycerol [28], cysteine [29], glutathione [30] and thioglycolic acid [31]. However, another alternative method and technique is the biosynthesis of ZnS NPs by the green route due to its simplicity, non-toxicity, stability, and cheapness [32]. The synthesis of nanoparticles using plant extracts can potentially eliminate the problem of the organic capping agents, which are expensive and toxic, by making the nanoparticles more biocompatible. To the best of the author's knowledge, several researchers have been focused on the green synthesis of ZnS NPs by different plants like Acalypha indica [33], Tridax procumbens [33], Abrus precatorius [34], Ficus Johannis [35], Azadirachta Indica [36]. In this context, Artemisia Herba-Alba (AHA) or "desert wormwood", also known as 'Chih', is an herbaceous plant with woody, branched stems, 30–50 cm high, leafy, and a thick stump. Artemisia Herba-Alba is a grayish perennial dwarf shrub growing in arid climates (the Middle East and North Africa) [37]. The leaves are small, sessile, pubescent, and showy silver.

The flowers are grouped in clusters and have ovoid flower heads [37]. Artemisia species have practical applications such as food additives [38], antiviral agents [39], antimalarial agents [40], antimicrobial agents [41], anti-inflammatory agents [42], and anti-hepatotoxic agents [43]. Moreover, some Artemisia species have practical applications in medicine for the treatment of various diseases, such as stopping pain, invigorating blood, relieving cough, and acting as a diuretic, anthelminthic, antiallergenic, and antitoxic agent [44]. This desert wormwood has more than 160 individual components, including many essential oils, terpenoids, flavonoids, luteolin and flavones [44]. The phytobioactive constituents present in the aqueous extract of AHA play an important role in capping and stabilizing the biosynthesized ZnS NPs. There are several studies on green synthesis. In this work, a rapid and new straightforward method for the green synthesis of ZnS-AHA NPs, using for the first time an extract of Artemisia Herba Aba is implemented, and these green nanoparticles are studied for their applications in gas sensors. ZnS-AHA NPs will be encapsulated in a chitosan film as a conductive film deposited on an interdigitated electrode for the detection of gaseous compounds. Chitosan (CS) is a natural polymer derived from chitin, which is found in the exoskeletons of crustaceans such as crabs, shrimp, and lobsters. It is obtained by deacetylating chitin through a chemical process that contains functional groups such as hydroxyl (-OH) and amino ($-NH_2$), displays sufficient affinity to small analytes [45]. It has gained attention in recent years due to its unique properties, such as abundance, biocompatibility, biodegradability, low cost, and low toxicity [46]. Chitosan can be used as a coating material for electrodeposition due to its ability to form a film on metal surfaces. The electrodeposition of chitosan is based on its local insolubility, caused by the local increase of the pH value through the electroreduction of protons [47]. Its biocompatibility and

biodegradability also make it an attractive alternative, making it applicable to electrochemical sensors [47], biosensors [48], gas sensors [49], and volatile organic compound sensors [50, 51]. It presents appropriate interactions with the capped nanoparticles due to their functional groups. In this work, after morphological and spectroscopic characterizations, ZnS-AHA NPs is encapsulated in an electrodeposited chitosan film, allowing the electroaddressing of the chitosan/ZnS-NPs film on the working pair of interdigitated electrodes, the reference pair being covered with a chitosan film for differential measurements. The detection of methanol and other VOC (ethanol, acetone) were measured in the headspace of aqueous liquid mixtures, at ambient temperature.

# II. Experimental

Chemicals, *Artemisia herba alba* plant extract, synthesis of AHA-capped ZnS NPs, fabrication process and packaging of micro-conductometric chips, electrodeposition of chitosan/ZnS-AHA films on the interdigitated electrodes, characterization techniques, and conductometric measurements are presented in the Supplementary Information.

# III. Results and discussion

## III.1 Nanoparticle characterization

### III.1.1 Morphological study of ZnS-AHA NAs

FTIR spectroscopy was used to measure the vibrational frequencies of bonds in the molecules and to confirm the presence of different functional groups on the surface of ZnS nanoparticles (***Figure IV.1a***). The absorption band at 540 $cm^{-1}$ was observed due to the Zn-S stretching vibrations [52]. The presence of Zn-S vibration clearly indicated that ZnS NPs were successfully formed. The absorption peak was observed at 3319 $cm^{-1}$ which is due to the alcohol/phenol group (-OH) stretching vibration [53]. The strong broad peak at 3665 $cm^{-1}$ is attributed to N-H stretching mode of the secondary amides, coming particularly from the identified molecule dihydroxanthin in plant extract [54]. The peak at 2978 $cm^{-1}$ is probably ascribed to C-H alkene stretching, while the band at 2893 $cm^{-1}$ could be assigned to the C-H stretching branched alkane coming particularly from the identified molecule cis-hydroxydavanone compound of AHA extract [54]. The peak at 1575 $cm^{-1}$ could be due to the C=O carbonyl stretching group, and the peak at 1057 $cm^{-1}$ was assigned to the stretching vibrations of primary alcohol groups in the AHA extracts [55]. Hence, these two peaks confirmed the involvement of flavonoids or polyphenolic compounds in AHA-capped ZnS NPs [55]. The peaks at 1393 and 1259 $cm^{-1}$ corresponded to $CH_3$ and C-O stretching vibrations coming particularly from the identified molecule

vulgarin [54]. FTIR analysis evidenced that green nanoparticles were stabilized with the major phytoconstituents of the AHA extract.

The crystal structures of the as-synthesized ZnS nanoparticles prepared using AHA as a capping agent were studied by X-ray diffraction (XRD), and the obtained XRD patterns are shown in ***Figure IV.1b***. The diffraction peaks are broad, confirming the nanometric size of the ZnS particles. For the phase identification, diffraction patterns of the ZnS were compared and analyzed using the diffraction standards of the wurtzite phase (JCPDS card No. 80-0020) and the zinc blende phase (JCPDS card No. 80-0007). XRD patterns can be indexed as cubic zinc blende structures, and they appear in good agreement with JCPDS data card No. 80-0007, with prominent peaks corresponding to the reflections at the (111), (222), and (311) planes. The non-appearance of diffraction peaks related to the wurtzite phase, demonstrates that AHA capping favors the cubic structure. To better quantify the effect of the stabilizers, the nanoparticle size was estimated through the Scherrer formula [53]:

$$D = \frac{K\lambda}{\beta \cos(\theta)} \quad (1)$$

where $D$ is the average crystallite size (Å), $k = 0.9$ is the Scherrer constant, $\lambda$ is the wavelength of X-ray (1.5402 Å) Cu Kα radiation, $\beta$ is the full width at half maximum of the diffraction peak (in radian) and $\theta$ is the Bragg diffraction angle, respectively. The estimated average sizes of the ZnS-AHA nanocrystals were equal to 3.93 nm. The smaller size of the ZnS crystallites encapsulated by AHA extract is most likely due to strong interaction of AHA molecules with ZnS nanocrystals which makes the growth slower [56]. On the other hand, the lattice constant of cubic phase of ZnS nanocrystals can be estimated using the following expressions:

$$d_{hkl}^2 = \frac{a_c^2}{h^2+k^2+l^2} \quad (2)$$

where $d_{hkl}$ is the inter-reticular distance for the hexagonal and cubic structure; $h$, $k$, and $l$ are Miller indices; $\lambda$ is the wavelength of the X-ray radiation; $a_c$, *is* the lattice constant of cubic phase of ZnS nanocrystals. The calculated average value of the lattice parameter of AHA ZnS nanocrystals was a= 5.4 Å. It should be kept in mind that the Scherrer formula considers only the size effects coming from the diffraction results, and it then offers a lower limit for the nanocrystals size and neglects the micro-strains [57,58].

The density ρ of ZnS-AHA NPs was calculated using the following expression [31]:

$$\rho = \frac{ZM}{N_A V} \quad (3)$$

where Z is the number of atoms per unit cell, M (g $mol^{-1}$) is the molecular weight of the ZnS, V is the volume of the unit cell ($cm^{-3}$) and NA is the Avogadro number. The specific surface

area S ($cm^2$ $g^{-1}$) of ZnS nanoparticles was calculated using the next equation [31]:

$$S = \frac{6}{\rho D} \quad (4)$$

where ρ (g $cm^{-1}$) and D (nm) are the x-ray density of cubic or hexagonal nanoparticles and the average particle size, respectively. The specific surface area of ZnS-AHA was found to be 36.82 $cm^2$ $g^{-1}$; this high specific surface area is a key factor to reaching the gas adsorption process.

***Figure IV.1c*** shows the HR-TEM images of the sample and the corresponding size distribution histogram. The aggregates could be due to high NPs concentrations (most likely during the solvent evaporation process for HR-TEM sample preparation). AHA-capped ZnS nanocrystals exhibit a spherical shape. The histogram of nanocrystals size distribution shows that the average crystal size is 4.03 ± 0.5nm. These results are in good agreement with XRD results. The d-spacing determined from the digital micrograph of ZnS is 0.29 nm, which is close to the spacing of (111) diffraction plane of cubic phase [59] and which shows that the growth of ZnS-AHA occurs preferentially along the direction [111]. Nanocrystals elemental composition was determined by EDX; the results presented in ***Figure IV.1d*** indicate that Zn and S are the major elemental components. The presence of C was related to the TEM grid. Other small peaks (Si and P) are also detected, probably due to residues coming from the synthesis and from the grid.

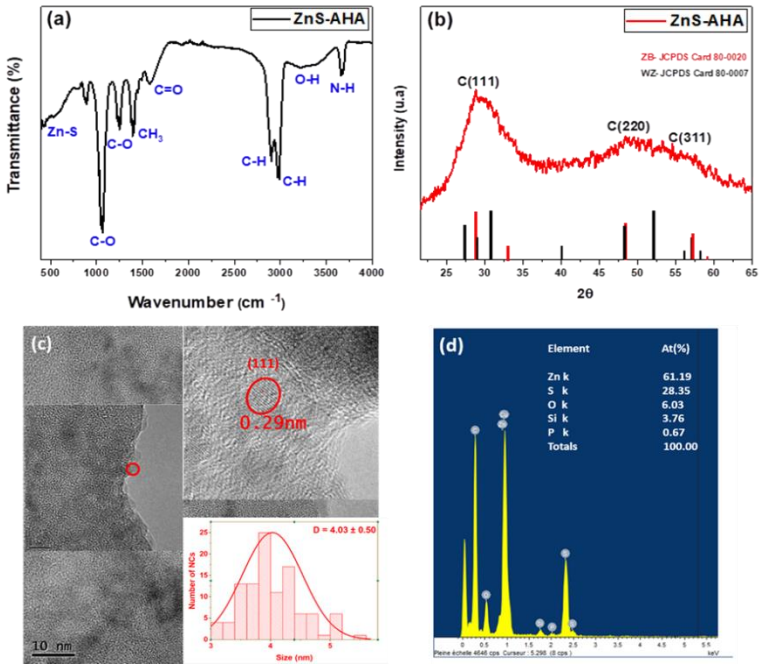


***Figure IV.1***:(a) FTIR spectra, (b) DRX patterns, (c) HR-TEM images with inset showing the 0.29 nm lattice spacing that corresponded to the (111) plane with the size distribution of ZnS-AHA nanocrystals and (d) EDX results of ZnS-AHA NPs.

### III.1.2 Optical study of ZnS-AHA NPs

In order to investigate the optical properties and the impact of the ligand on the stability and size distribution of the nanoparticles, the optical absorption spectra of the ZnS NPs dispersed in water were recorded (***Figure IV.2a***). The UV-visible absorption spectrum of ZnS NPs suspension shows an absorption band at 325 nm related to the first electronic transition 1Se-1Sh [60]. The blue shift as compared to bulk ZnS (344 nm, $Eg$ = 3.6 eV) is due to the quantum confinement of charge carriers as a result of the small particle size. This tendency is characteristic of semiconductors II-VI and is mainly associated with the nanocrystal size distribution and sub-band gap transitions arising from the intrinsic–extrinsic defect states. We have determined graphically the value of the optical and band-gap energy $Eg$ using the following relation of Tauc [61]:

$$\alpha h\nu = A\,(h\nu - Eg)^n \qquad (5)$$

Here, $\alpha$ is the absorption coefficient, $A$ is a constant, $h$ is the Planck constant, $v$ is the frequency of radiated photons and n is a transition-dependent factor ($n$ = 1/2 for direct semiconductors). The optical gap energy of the capped ZnS NPs is obtained by extrapolating the plot of the function $(\alpha h\nu)^2$ to the value $\alpha = 0$. The intersection of the line with the horizontal axis gives the value of the band gap energy, see insert in ***Fig. 2a***. The estimated band gap energy for the green ZnS is 3.70 eV. It is clear that the gap energy of these NPs shifts towards the blue compared to the bulk ZnS ($E_g$ = 3.6 eV) due to the very small size of NPs, which induces a quantum confinement effect (QCE) [62].

***Figure IV.2b*** shows the emission spectra of ZnS NPs obtained with an excitation wavelength $\lambda_{exc}$= 325 nm at room temperature. An intense and wide band centered at 450 nm dominates the spectrum. The obtained emission spectra are deconvoluted using three Gaussian profiles associated with three main bands. The first band is the less intense and has a spectral width of a few nm, which is strongly correlated with the size of the nanoparticles. This band was attributed to the direct band-to-band recombination of excitons. The second emission band in the blue region (450 nm), which dominates the spectrum, was attributed to recombination between electrons and holes at the edges of the conduction and valence bands, respectively, or involved very shallow recombination centers (sulfur vacancies) [63]. Finally, the green emission band (500 nm) was attributed to the interstitial zinc atom ($I_{Zn}$) [22]. The FWHM of the main emission is equal to 62 nm, which is related to the size dispersion of the ZnS-AHA NPs.

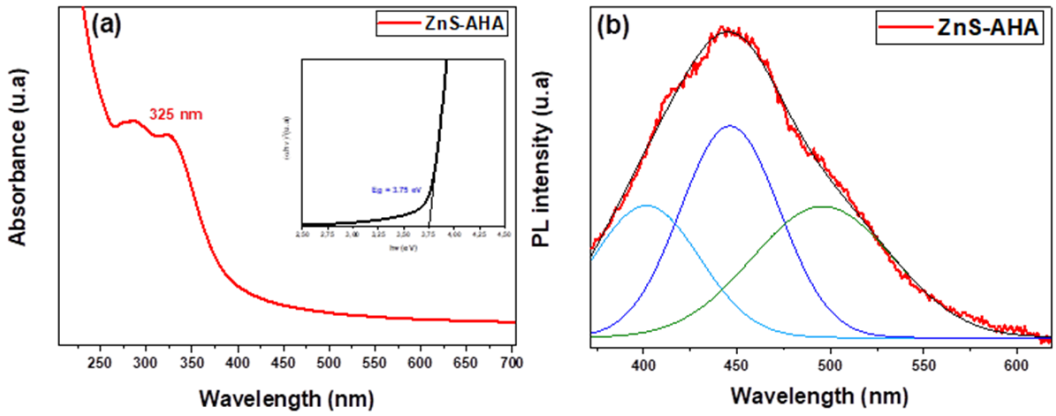


***Figure IV.2***: (a) Absorption spectra and (b) Gaussian adjustment of PL spectra of ZnS-AHA NPs.

### III.1.3 The EDS mapping of CS/ZnS

CS/ZnS is a composite consisting of a chitosan (CS) matrix combined with zinc sulfide (ZnS) nanoparticles. EDS mapping can be used to determine the spatial distribution of these elements on micro-conductometric chips. According to ***Figure IV.3a***, we observe the presence of different chemical elements such as Au, Si, Ti, C, Zn, and S, which are at the origin of the deposit of CS/ZnS on the electrodes, which are already based on Au, Si, and Ti. Zn mapping (***Fig. 3b***) was obtained when focusing on the ZnKa2 Xray at 8.639 keV, which is at the foot of the AuLL Xray at 8.484 keV. A contribution of Au is then observed on the interdigitated electrodes. The dispersion of Zn is well observed between the interdigitated electrodes, in the insert of ***Figure IV.3b***. S mapping (***Figure IV.3c***) was obtained when focusing on the Ska Xray at 2.307 keV, which is partly covered by the AuMb Xray at 2,203 keV. A contribution of Au is then observed on the interdigitated electrodes. The dispersion of S is well observed between the interdigitated electrodes, in the insert of ***Figure IV.3c***. EDS elemental mapping results suggest that Zn and S are homogeneously distributed on the micro-conductometric chips, showing that the AHA-ZnS NPs are well dispersed in the chitosan film.

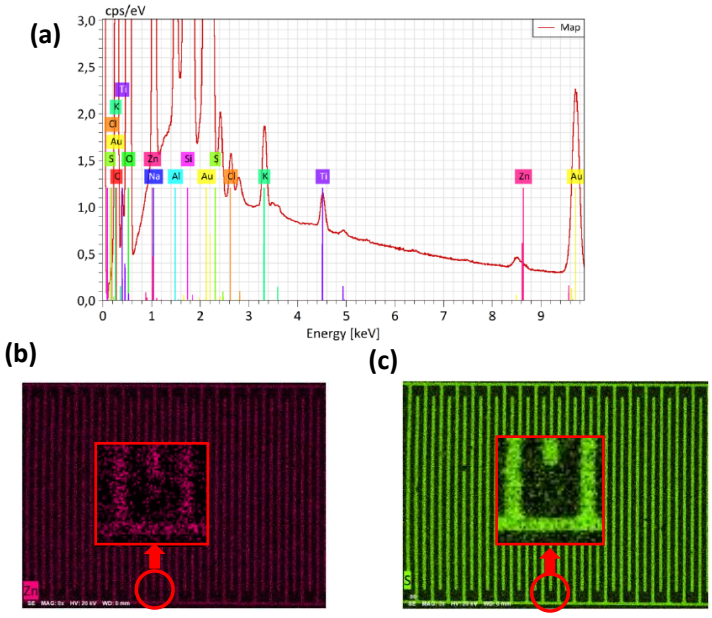


***Figure IV.3*:** The EDS mapping of Chitosan/ZnS composite for atomic distribution of Zn and S. (a) EDS spectrum, (b) Zn EDS mapping, (c) S EDS mapping.

## III.2 The conductometric measurements

### III.2.1 Conductimetric response to vapors and proposed mechanism

The preparation of the standard solution and calculation of the gas phase content through Henry's law [64,65] are presented in ***section 8*** of the Supplementary Information.

To evaluate the response to target gas and to find the best gas sensing, the conductometric detection of several volatile organic compounds 'VOCs' (methanol, ethanol, acetone, chloroform and water) were performed.

The conductivity of the Chitosan-ZnS composite-based sensor, read in differential mode by the lock-in amplifier, increased dramatically when exposed to the headspace of pure solvents, as it is observed in ***Figure IV.4***. As clearly seen, the response of the sensor shows a higher response to methanol compared to the other VOCs. It can be supposed that AHA-capped ZnS NPs promote surface defect formation with the creation of more active sites, which consequently enhances the gas sensing performances.

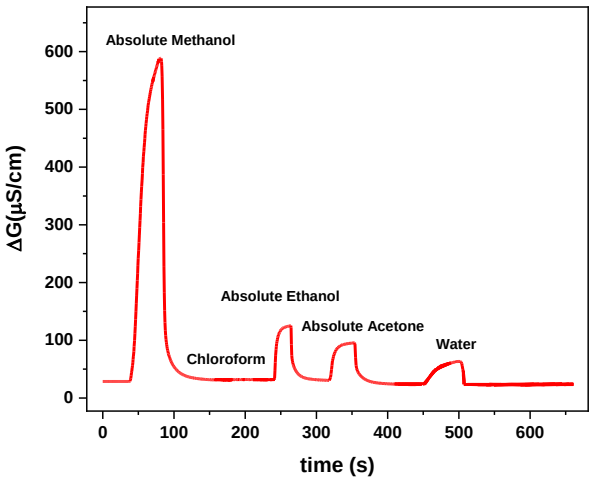


***Figure IV.4***: Detection of gas-phase concentration for pure liquid phase of methanol, acetone, chloroform, ethanol, water.

***Figure IV.5*** describes the proposed schematic illustration of methanol gas sensing using ZnS-AHA NPs sensor. The sensing mechanism occurring during methanol detection on chitosan/ZnS-NPs sensor, can be described as follows: The first step is the oxygen adsorption on the sensor's surface, adsorbed from the outside air. The oxygen ions adsorbed on the surface of the AHA-capped ZnS NPs (Reaction (5)) and can form a depletion layer, withdrawing electrons from the bulk, which leads to an increase in the electrical resistance. $O^-$ species are then formed (Reaction (6)). Once exposed to reducing gas (methanol, $CH_3OH$), $O^-$ species will react with the gas (Reaction (7)) and enable the electrons injected back into the active material, causing an increase in electronic conductivity [66]. Recombination $e^-/h^+$ will then occur (Reaction (8)).

$$O_2\,(gas) \rightarrow O_2\,adsorbed \tag{6}$$

$$O_2\,adsorbed + 2e^- \leftrightarrow 2O^-\,(adsorption) \tag{7}$$

$$CH_3OH\,(vapor) + 3O^-\,(adsorption) \leftrightarrow CO_2 + 2H_2O + 3e^- \tag{8}$$

$$e^- + h^+ \rightarrow null + energy \tag{9}$$

The $h^+$ means the holes with positive charge.

After the methanol vapor is introduced, the oxygen species containing $O^-$ will react with gas molecules, resulting in an increase in sensor sensitivity. The high response and short response and recovery times of chitosan and ZnS-NPs are mainly based on the large surface-to-volume ratio of ZnS-AHA NPs, which is a vital factor for high sensing performance. In addition, the quantity of sulfur vacancies on ZnS-AHA NPs is also increased due to the large concentration

of AHA ligand on the NPs surface. The high content of sulfide vacancies is confirmed by the photoluminescence spectra (***Figure IV.2***), which are dominated by the recombination between sulfur vacancies (Vs) and the valence band. Thus, more oxygen species were adsorbed on the surface of chitosan/ZnS-NPs which yielded a greater response. The sensor response towards methanol is much higher than that towards ethanol, acetone due to the fact that the sensor works on the principle of adsorption, in which methanol has a higher polarity and less steric hindrance than ethanol or acetone. This more favorable interaction with the sensor is achieved through hydrogen bonding [67].

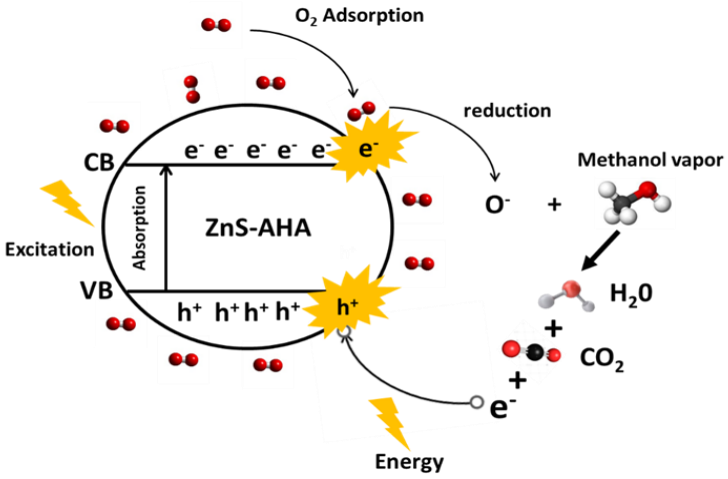


***Figure IV.5***: Schematic illustration of methanol gas sensing using chitosan/ZnS-NPs sensor.

### III.2.2 Analytical performance

Microconductometric measurements in the headspace of different methanol/water solutions are given in ***Figure IV.6***. It is clear that the sensor conductance increases with an increase in the concentration of methanol in the gas phase.

The response time ($t_{Res}$) of the chitosan/ZnS-NPs based conductometric sensor varies from 11 to 25 s from lower to higher concentrations (***Figure IV.7***). Whereas the time to be recovered ($t_{Rec}$) back to the baseline, immediately after removal from the headspace, varies from 5 to 11 s. The calibration curve of the chitosan/ZnS-NPs based sensor for methanol, ethanol, and acetone are presented in ***Figure IV.8***. Calibration curve for methanol sensor presents the best linearity ($R^2 = 0.99988$) and the highest sensitivity S: 52.42 $\mu S.cm^{-1}(v/v)$, 3.8 times higher than that of ethanol (13.8 $\mu S.cm^{-1}(v/v)$) and 30 times higher that of acetone (1.75 $\mu S.cm^{-1}(v/v)$). The sensor-based on chitosan/ZnS-NPs presents a detection limit for methanol of 0.14 v/v% (1400 ppm) in the gas phase, this concentration corresponds to 0.31 M in the aqueous phase, the detection limit being calculated according to the following expression: $2\sigma/S$, $\sigma$ being the noise

from the blank. The relative standard deviation for the described sensor, over ten determinations, ranged from 2% for higher concentrations to around 8 % for lower concentrations. The reproducibility was studied, using 5 different methanol sensors. The obtained relative standard deviation ranges from 10 % for all concentrations.

The reusability experiment for the CS/ZnS-AHA film sensor was performed in 4 cycles with a time interval of 15 days. The main object of reusability was to investigate the results reproducibility of a methanol gas sensor. The optimum response given by CS/ZnS-AHA for methanol was 85 %, whether the same results are reproduced by the film sensor was investigated in the experiment. With a time interval of 15 days in four turns, a slight decrease in response was observed for methanol due to visible degradation in the homogeneity of the prepared film sensor of CS/ZnS-AHA. The results obtained in the experiment are expressed in ***Figure IV.9***. The sensor keeps its sensitivity of detection for two months, when kept in the fridge at 4 °C between the measurements.

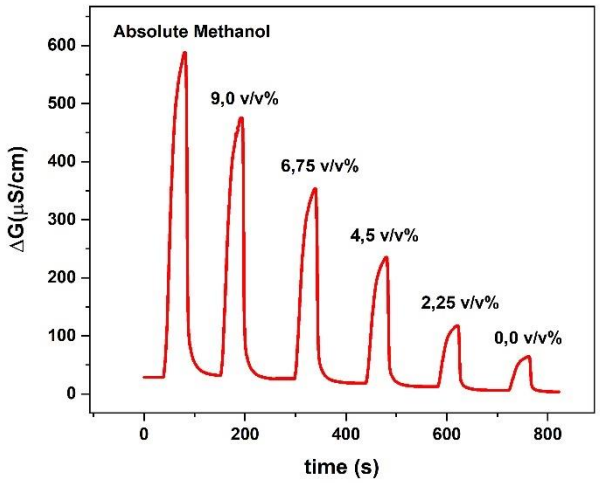


***Figure IV.6*:** Detection of gas-phase concentration for different methanol/water solutions chitosan/ZnS-NPs sensor, using a lock-in amplifier.

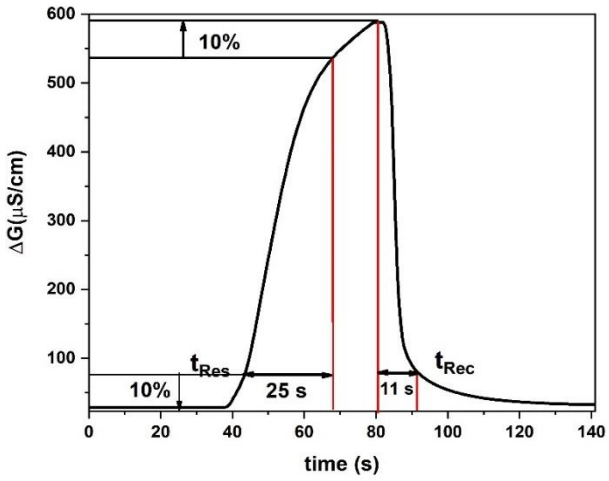


***Figure IV.7***: Response time ($t_{Res}$) and recovery time ($t_{Rec}$) on the real-time registration of the ethanol sensor response.

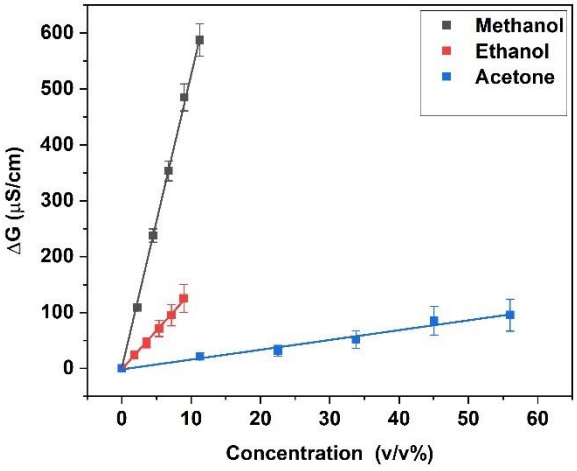


***Figure IV.8***: Calibration curve of the gas-phase concentrations of acetone, ethanol, and methanol.

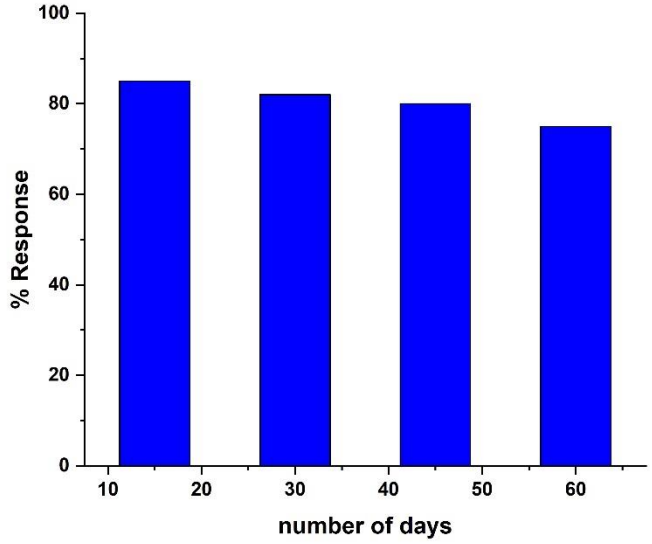


***Figure IV.9***: Reusability for Chitosan/ZnS-NPs sensor for methanol gas.

To confirm the sensor selectivity, methanol was measured in the presence of ethanol and acetone (***Figure IV. S5***). It is observed that the methanol signal is increased by a factor of 10% in the presence of ethanol (2%) and by a factor of 4 % in the presence of acetone (2%), which is in the range of relative standard deviation. We noticed from ***Figure IV.4*** that the detection signal of the pure methanol gaseous phase is 587 $\mu S.cm^{-1}$ and that of pure water is 63 $\mu S.cm^{-1}$. Even though chitosan is hygroscopic, the differential measurement decreases the signal from the water and limits its interfering effect.

A lot of methanol sensors have been fabricated (***Table IV.1***) but this is the first time that green synthesized ZnS-AHA is used for the conductometric detection of methanol. The obtained sensor works at ambient temperature and has a short response time. The interferences of water and of ethanol are quite limited.

***Table IV.1***: Response times and detection limits of previously published methanol sensors based on various materials.

| Methanol sensors | Operating temperature (°C) | Response time ($t_{Res}$) | Detection limit (ppm) | Refs |
|---|---|---|---|---|
| TiO2 doped CdS/amperometry | 360 | 10 s | 0.18 | [68] |
| ADH/Amperometry | 36 | 5 s | 10 | [69] |
| Pd doped SnO2 nanoparticles/ conductivity | 350 | 25s-10s | 1 | [70] |
| graphene oxide/polyindole / conductivity | 26 | 7 | 0.015 | [71] |
| Pd–Pt–$In_2O_3$/$SnO_2$ | 160 | 32 | 0.1 | [72] |
| ZnO/$MoO_3$ | 200 | 54 | 34 | [73] |
| rGO–$TiO_2$ nanotubes | 110 | 41 | | [74] |
| dPIn pellet | 26 | 26 | 48 | [75] |
| PVC-NiPc nanofibers | 25 | 13 | 15 | [76] |
| Chitosan-NiPc/Conductometry | 25 | 32s-25s | 700 | [77] |
| Chitosan-ZnS/Conductometry | 25 | 25s-11s | 1400 | This work |

### III.2.3 Application of methanol sensor

The new standard 10% methanol ice washer is a product made from 10% methanol and used as a degreaser and windshield cleaner. After detection in the gas phase of an absolute and of a 20% methanol solution, the detection in the gas phase of the new standard 10% methanol ice washer was carried out (***Figure IV. S6***). The conductivity found in the ice washer gas phase was 67.1 µS/cm. This value corresponds to 1.27 ± 0.16 v/v% in the gas phase. The determined concentration of ice washer is then 2.79 ± 0.35 M, corresponding to 11.29 ± 2.83 %, which is in good agreement with the value given by the producer, 10%.

In the same domain of gas/vapor sensors, previously published, a chemiresistor sensor based on palladium nanoparticles allows the detection of methanol in perfumes and dyes and presents a detection range of 0.31 mM–3.5 mM [78]. Our fabricated microconductometric methanol sensor is comparatively less sensitive, with a relatively large detection limit (310 mM). In order to improve the sensor's sensitivity, the gas detection could be done under UV light illumination, which may enhance the production of $O^-$ species.

## IV. Conclusion

In summary, the present findings demonstrate the new synthesized AHA-capped ZnS NPs via a stable, simple, colloidal route at room temperature. Therefore, for the first time, an innovative green method for preparing luminescent ZnS nanoparticles was developed using *Artemisia Herba Alba*. FTIR results confirmed the functionalization of nanoparticle surfaces by AHA ligands. XRD analysis indicated the formation of nanocrystals with a cubic phase. The average

size of AHA-capped ZnS nanocrystals calculated using the Debye-Scherrer formula and measured by HRTEM was around 4 nm. These new nanoparticles were used for methanol vapor detection, after their introduction in a chitosan film. The new sensor shows excellent sensitivity toward methanol 3.8 times higher than toward ethanol, 30 times higher than toward acetone. The response time ($t_{90}$) of the sensor varies from 11 to 25 s for lower to higher concentrations. The detection limit is 1400 ppm in the gas phase, corresponding to 0.31 M in the liquid phase. This detection limit could be improved under UV light illumination, and this sensor could then be used for the measurements of methanol in exhaled breath.

# V. Supplementary Information

## V.1 Experimental section

### V.1.1 Chemicals and Reagents

Analytical grade chemicals were used from commercial sources without any further purification. Zinc (II) acetate dihydrate (Zn $[CH_3COO]_2.2H_2O \geq 98\%$), sodium sulfide ($Na_2S \geq 98\%$), sodium hydroxide (NaOH, 99%), Chitosan lower molecular weight (deacetylated chitin, degree of acetylation 85-95% Mw=230 kDa) and glacial acetic acid (99.9%) were purchased from Sigma-Aldrich. Ultra-pure water (UPW) from Millipore System was employed in all aqueous solutions (resistivity >18 MOhm.com).

### V.1.2 Artemisia Herba Alba extraction

Artemisia Herba Alba (AHA) leaves were collected in Tunisia. The selected parts of AHA plants were washed with deionized water, dried in the shade at room temperature, and ground into powder. 11.5 g of powder was added to 200 mL of distilled water. The mixtures were boiled at 100 °C for 2h and filtrated at room temperature. The filtrated aqueous solution is the extract of A. herba-alba, which is used for ZnS nanoparticle fabrication in the present study. ***Figure IV. S1*** shows a picture of A. herba-alba leaves and their extract.


***Figure IV.S1***: Artemisia Herba Alba plant and its extract.

### V.1.3 Synthesis of AHA-capped ZnS NPs

The detailed preparation method of ZnS nanoparticles was reported elsewhere using the colloidal wet chemical route [31,59]. *Artemisia Herba Alba* (AHA) was used as a stabilizer for preparing the green ZnS NPs. The typical synthesis process of AHA capped ZnS NPs is the following one: 20mL of *Artemisia Herba Alba* aqueous extract were mixed with 3mM of Zn[OOCCH3]2·2H2O solution. The mixture was agitated and degassed in the presence of N2 for 30 min. In a second step, 1.2 mM of Na2S solution was added to the solution containing Zn-AHA complexes at room temperature under stirring. Then, the mixture was heated under N2 reflux at 100 °C for 3 h to obtain the final AHA-capped ZnS NPs. The dried precipitate was allowed to cool down naturally at room temperature in order to stop the growth of NPs. A nanocolloidal suspension was formed and centrifuged at 2500 rpm for 20 min; After removing the supernatant and replacing it with ethanol, the suspension was centrifuged, and after removing the supernatant, the obtained nanoparticles were stored at room temperature.

### V.1.4 Fabrication process and packaging of micro-conductometric chips

The interdigitated microelectrode chip was fabricated using UV lithography and thin film e-beam evaporation deposition. The fabrication procedures were carried out at the Institute of Nanotechnology of Lyon (INL), Lyon, France. The size of the interdigitated chip was 5x 28.7 mm. Finger width was 20 µm, the finger distance was also 20 µm. The flowchart for the process of fabrication of the microconductometric chip is presented in ***Figure IV.S2***.

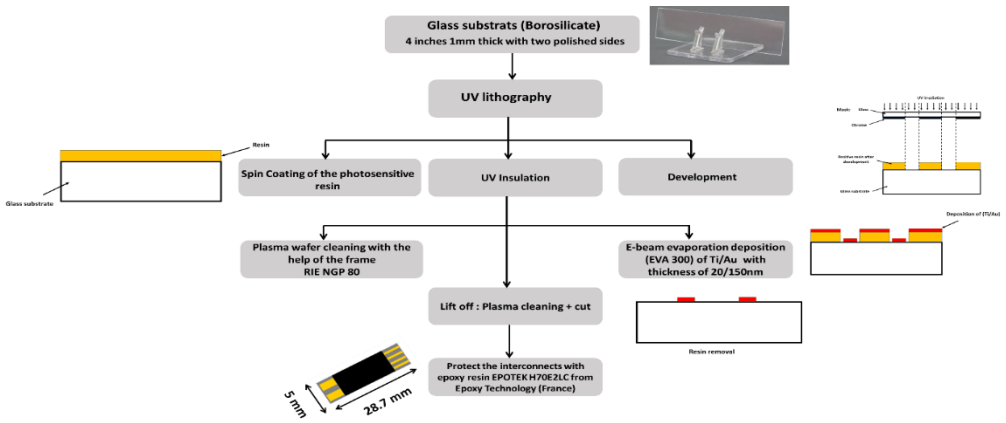


***Figure IV.S2***: Flow-chart for the process of fabrication of microconductometric chips

### V.1.5 Electrodeposition of chitosan/ZnS-AHA films on the interdigitated electrodes

The fabricated microelectrode chips were cleaned through sonicating in ethanol for 15 min, in acetone for 15 min, rinsed in water, dried under a nitrogen flow, and then exposed to UV-Ozone Pro Cleaner (BioForce) for 30 min before electrodeposition of chitosan/ZnS-AHA on the electrode surfaces. The chemical composition of the ZnS-AHA NPs suspension was: 1% (v/v) of acetic acid, 1% (w/w) of chitosan; (lower molecular weight). The pH was adjusted at 7 by carefully adding drops of 0.1M NaOH into the chitosan suspension while agitating using a magnetic. The electrodeposition process for the fabrication of the conductimetric sensor is presented in ***Figure IV.S3***.

For the chronoamperometric deposition technique, a three-electrode format was used: the working sensor as a working electrode, an Ag/AgCl as reference electrode, and a platinum wire as counter electrode. The next step was carried out by putting the three electrodes in a 5 mL beaker of Chitosan + ZnS NPs solution (working electrode). The chronoamperometric deposition was conducted at an applied potential of -1.4 V for 4 min by using an EC LAB potentiostat [51]. The cathodic current at the electrode, measured as a function of time, fluctuated according to the diffusion of $H^+$ from the bulk solution towards the sensor surface. The current (mA) continued to decrease until it became stable within 4 min, which assumes the (chitosan/chitosan + NPs) film is well deposited on the gold surface to form a film. A current of 50 µA is observed through the proton reduction, and then a decrease in this current is observed, due to the deposition of the chitosan (chitosan/ZnS-NPs) film on the interdigitated electrodes (IDEs). A stable value of 3 µA is observed after the first minute (***Figure IV.S4***). The same procedure is used for the reference sensor, a chitosan film is deposited without ZnS-NPs. After electrodeposition, the chips were carefully rinsed in ultrapure water (UPW), kept dry in air for 45 min, and then stored in the fridge at 4 °C before use. The fabricated sensor from chitosan/ZnS-AHA is ready for gas detection using conductometric measurements in the differential mode.

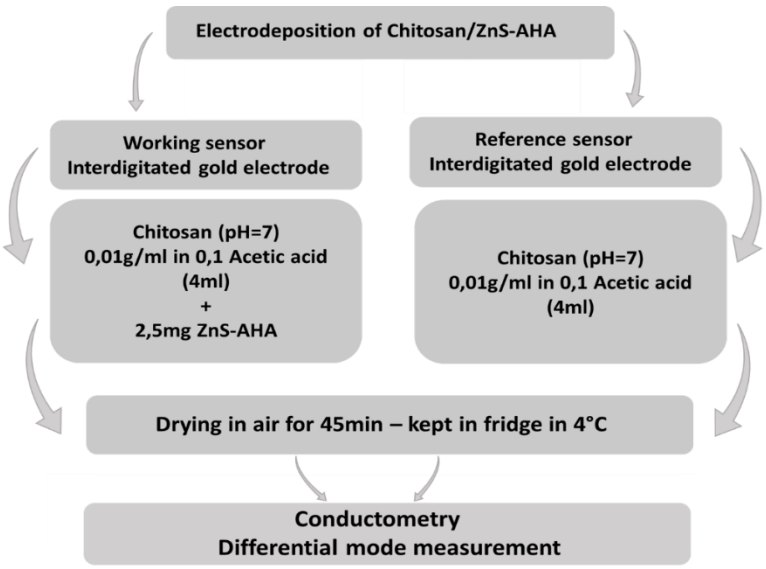


***Figure IV.S3***: Flow-chart for the process of fabrication of microconductometric chips

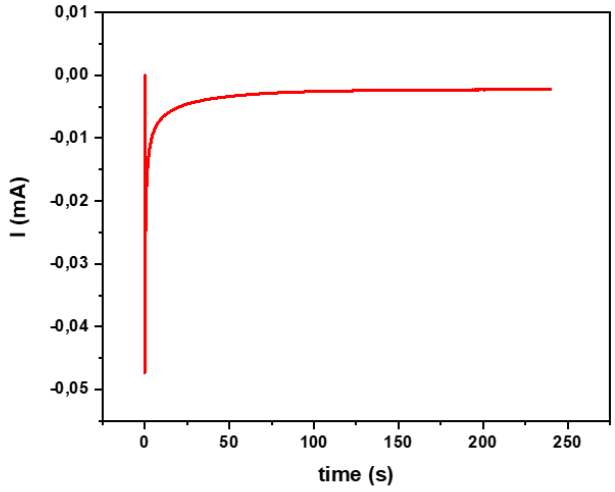


***Figure IV.S4***: Chronoamperometric measurement monitoring of electrodeposition of chitosan.

### V.1.6 . Characterization techniques

Various techniques were applied to characterize AHA-capped ZnS NPs. XRD measurements were performed using Panalytical X' Pert Pro diffractometer with a CuKα radiation source (λ=1,542Å).

The Fourier transform infrared (FTIR) spectrum of ZnS-AHA NPs was obtained in the transmission mode at room temperature using a Perkin Elmer version 5.3 spectrophotometer in the spectral range of 400–4000 $cm^{-1}$ using KBr pellet disks.

HR-TEM images were obtained using a JEM-2100 analytical electron microscope operating at an accelerating voltage of 200 kV and equipped with an Energy Dispersive X-ray (EDX) system for elemental chemical analysis. A drop of nanocrystal solution was poured on carbon-coated copper grids to obtain HR-TEM samples after the excess solvent was evaporated. The nanocrystal size and size distribution data were obtained based on the HR-TEM images by measuring at least 100 randomly selected nanocrystals using an image processing program (ImageJ, version 1.50).

SEM images were obtained using a Tescan Vega SBU scanning electron microscope, operating at an accelerating voltage of 20 kV, equipped with a Bruker Esprit Compact EDS detector.

Absorbance spectra were recorded using a SPECORD 210 Plus spectrophotometer with a quartz cuvette in the range of 200-800 nm at room temperature. Photoluminescence (PL) spectroscopy was applied to analyze the defects and emission properties of the ZnS using as exciting source the 325 nm of a helium-cadmium laser source.

### V.1.7 Conductometric measurements

Conductometric detection was achieved by applying to each pair of interdigitated electrodes (sensors) a small-amplitude sinusoidal voltage (10 mV peak-to-peak at 0 V) at a 10 kHz frequency generated by "VigiZMeter" conductometer which is manufactured by the company “Covarians”, and the responses of the gas sensor were recorded as a function of time. These conditions were used to reduce faradaic processes, multi-layer charging, and polarization at the microelectrode surface [51]. The differential output signal was recorded between the working and the reference pairs of interdigitated electrodes. The working sensor was obtained by electro-deposition of a chitosan/ZnS-AHA NPs film and the reference sensor was obtained by the electro-deposition of a chitosan film. Conductometric measurements were done by introducing the working sensor and the reference sensor in the headspace over the liquid phase in a cylindrical container for one minute and then by withdrawing it (***Figure IV.S5***). The differential measurement of conductance ($\Delta G$) was recorded versus time. The response time ($t_{Res}$) describes the time necessary to reach 90% of the total change of conductance and the recovery time ($t_{Rec}$) characterizes the time necessary to recover 10% of the total change in conductance.

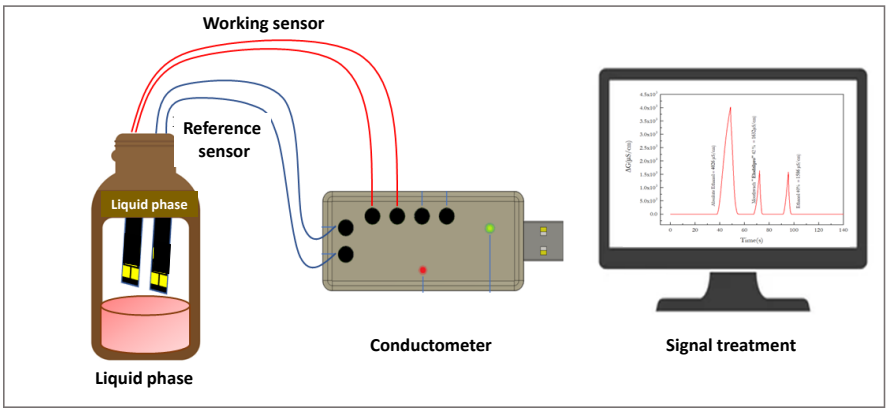


***Figure IV.S5***: Diagram of the experimental setup.

### V.1.8 Preparation of VOC samples

The gas sensor performance was tested in methanol, ethanol and acetone samples which were collected from the headspace above aqueous solutions with known concentrations of (0-100%). The as-mentioned gas phase concentration depends on Henry's law constants of the given analyte in water and was calculated from Henry's law following the equation announced at 25°C by Sander in 1999 [63].

$$k_H^0 = \frac{c_a}{p_g} \tag{S.4}$$

Where $k_H^0$ is the Henry's law constant for standard conditions; $[k_H^0]$ = M/atm, $c_a$ is the aqueous concentration of the analyte; [ca] = M and $p_g$ is the partial pressure of the analyte in the gas phase; [pg] = atm.

For the gas analytes listed above at (25°C) i.e, methanol, ethanol, and acetone; Henry's law constants value of $2.2 \times 10^2$ M/atm, $1.9 \times 10^2$ M/atm, and $0.24 \times 10^2$ M/atm were considered respectively [65]. In ***Table IV.S1***, the calculated equilibrium gas-phase concentrations of methanol, ethanol and acetone above the aqueous phase are listed.

***Table IV.S1***: Equilibrium gaseous phase concentrations above aqueous methanol, ethanol, and acetone solution at 25 °C per Henry's law constants reported by Sander et al [65].

| S/N | % Volumetric concentration | Concentration of methanol in the gaseous phase (% v/v) | Concentration of ethanol in the gaseous phase (%v/v) | Concentration of acetone in the gaseous phase (% v/v) |
|---|---|---|---|---|
| 1 | 0% | 0 | 0 | 0 |
| 2 | 20% | 2.25 | 1.79 | 11.26 |
| 3 | 40% | 4.5 | 3.58 | 22.52 |
| 4 | 60% | 6.75 | 5.37 | 33.78 |
| 5 | 80% | 9 | 7.16 | 45.04 |
| 6 | 100% | 11.25 | 8.95 | 56.03 |

To confirm the sensor selectivity, in addition to the methanol/water solutions we have tested the Measurement of methanol when ethanol and acetone are presented. From ***Figure IV.S5***, it is observed that the methanol signal is increased by a factor of 10% in the presence of ethanol (2%) and by a factor of 4 % in the presence of acetone (2%).

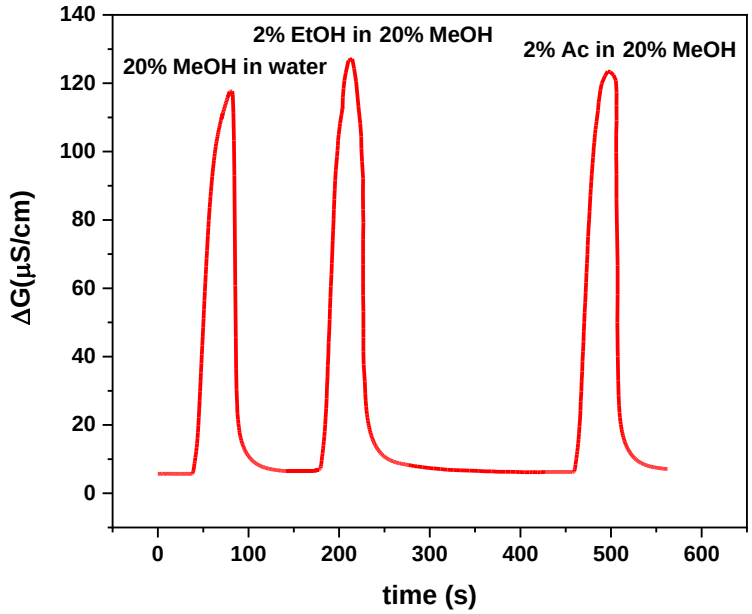


***Figure IV.S6***: Effect of the presence of 1/5 of ethanol and of acetone compared to methanol on the sensor signal.

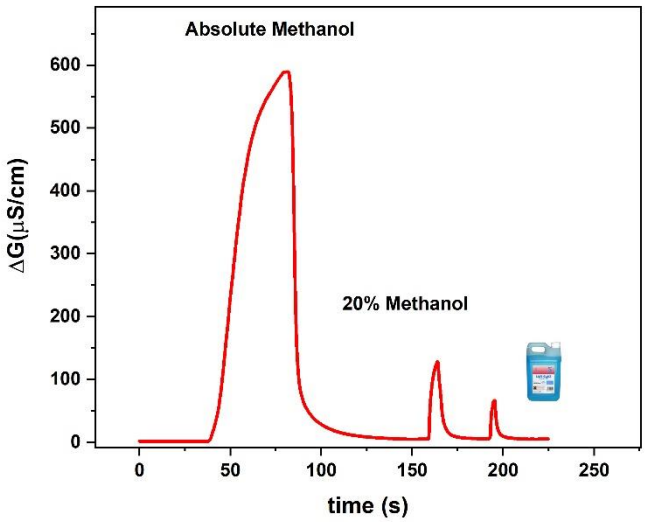


***Figure IV.S7***: Detection of gas-phase concentrations for different methanol/water solutions and commercial ice washer product, with the chitosan/ZnS-NPs sensor.

# VI. References


[1] J.A. Kruse, Methanol poisoning. Intens. Care Med. 18, 391–397(1992). https:// doi.org/ 10. 1007/ BF016 94340

[2]K.E. Hovda, O.H. Hunderi, A. Tafjord, O. Dunlop, N. Rudberg, D. Jacobsen, Methanol outbreak in Norway 2002–2004: epidemiology, clinical features and prognostic signs. J. Intern. Med. 258, 181–190 (2005). https:// doi. org/ 10. 1111/j. 1365- 2796. 2005. 01521.x

[3] F. Schorn, J.L. Breuer, R.C. Samsun, T. Schnorbus, B. Heuser, R. Peters, D. Stolten, Methanol as a renewable energy carrier: an assessment of production and transportation costs for selected global locations. Adv. Appl. Energy. 3, 100050 (2021). https:// doi.org/ 10. 1016/j. adapen. 2021. 100050

[4] J.A. Joseph, S. Akkermans, J.F.M. Van Impe, Processing method for the quantification of methanol and ethanol from bioreactor samples using gas chromatography-flame ionization detection. ACS Omega 7, 24121–24133 (2022). https:// doi. org/ 10. 1021/ acsom ega. 2c000 55

[5]K. Sharma, S.P. Sharma, S. Lahiri, Novel method for identification and quantification of methanol and ethanol in alcoholic beverages by gas chromatography-fourier transform infrared spectroscopy and horizontal attenuated total reflectancefourier transform infrared spectroscopy. J. AOAC Int. 92, 518–526 (2009). https:// doi. org/ 10. 1093/ jaoac/ 92.2. 518

[6]P. Maksimov, A. Laari, V. Ruuskanen, T. Koiranen, J. Ahola, Gas phase methanol synthesis with Raman spectroscopy for gas composition monitoring. RSC Adv. 10, 23690–23701 (2020). https:// doi. org/ 10. 1039/ D0RA0 4455E

[7] S. Kumar, G. Sharma, V. Singh, Modelling of surface plasmon resonance sensor for detection of mass concentration of ethanol and methanol in a binary mixture. Infrared Phys. Technol. 67, 190–196 (2014). https:// doi. org/ 10. 1016/j. infra red. 2014. 07. 021

[8]K.W. Khalid, A.A. Abadi, F.A. Dawood, Synthesis of SnO nanowires on quartz and silicon substrates for gas sensors. J. Inorg. Organomet. Polym. Mater. 30, 3294–3304 (2020). https:// doi. org/ 10. 1007/ s10904- 020- 01617-3

[9] V. Shah, J. Bhaliya, G.M. Patel, P. Joshi, Room-temperature chemiresistive gas sensing of SnO nanowires: a review. J. Inorg. Organomet. Polym. Mater. 32, 741–772 (2022). https:// doi. org/ 10. 1007/ s10904- 021- 02198-5

[10] S.T. Hezarjaribi, S. Nasirian, An enhanced fast ethanolsensor based on zinc oxide/nickel oxide nanocompositein dynamic situations. J. Inorg. Organomet. Polym. Mater. 30, 4072–4081 (2020). https:// doi. org/ 10. 1007/ s10904- 020- 01556-z

[11] M. Shahabi, H. Raissi, Assessment of DFT calculations and molecular dynamics simulation on the application of zinc oxide nanotube as hydrogen cyanide gas sensor. J. Inorg. Organomet. Polym. Mater. 27, 1878–1885 (2017). https:// doi. org/ 10. 1007/ s10904- 017- 0656-z

[12] P.S. Kolhe, P.S. Shirke, N. Maiti et al., Facile hydrothermal synthesis of WO nanoconifer thin film: multifunctional behavior for gas sensing and field emission applications. J. Inorg. Organomet. Pol8
ym. Mater. 29, 41–48 (2019). https:// doi. org/ 10. 1007/ s10904- 018- 0962-0

[13]A. Gaiardo, B. Fabbri, V. Guidi, P. Bellutti, A. Giberti, S. Gherardi, L. Vanzetti, C. Malagu, G. Zonta, Metal sulfides as sensing materials for chemoresistive gas sensors. Sensors 16, 296 (2016). https:// doi. org/ 10. 3390/ s1603 0296

[14] R. Souissi, N. Bouguila, B. Bouricha, C. Vazquez-Vazquez, M. Bendahan, A. Labidi, Thickness effect on VOC sensing properties of sprayed In2S3 films. RSC Adv. 10, 18841 (2020). https:// doi. org/ 10. 1039/ d0ra0 1573c

[15] W. Shan, Z. Fu, M. Ma, Z. Liu, Z. Xue, J. Xu, F. Zhang, Y. Li, Facile chemical bath synthesis of sns nanosheets and their ethanol sensing properties. Sensors 19, 2581 (2019). https:// doi. org/ 10. 3390/ s1911 2581

[16] R.K. Mishra, G.J. Choi, H.J. Choi, J.S. Gwag, ZnS quantum dot-based acetone sensor for monitoring health-hazardous gases in indoor/outdoor environment. Micromachines 12, 598 (2021). https:// doi. org/ 10. 3390/ mi120 60598

[17] L. Zhang, R. Dong, Z. Zhu, S. Wang, Au nanoparticles decorated ZnS hollow spheres for highly improved gas sensor performances. Sens. Actuators B 245, 112–121 (2017). https:// doi. org/ 10. 1016/j. snb. 2017. 01. 179

[18] L. Chang, X. He, L. Chen, Y. Zhang, Mercaptophenylboronic acid-capped Mn-doped ZnS quantum dots for highly selective and sensitive fluorescence detection of glycoproteins. Sens. Actuators B 243, 72–77 (2017). https:// doi. org/ 10. 1016/j. snb. 2016. 11. 121

[19] Z. Bujňakova, E. Dutkova, M. Kello et al., Mechanochemistry of chitosan-coated zinc sulfide (ZnS) nanocrystals for bio-imaging applications. Nanoscale Res. Lett. 12, 328 (2017). https:// doi. org/ 10. 1186/ s11671- 017- 2103-z

[20] P.A. Ajibade, A.E. Oluwalana, B.M. Sikakane, M. Singh, Structural, photocatalytic and anticancer studies of hexadecylamine capped ZnS nanoparticles. Chem. Phys. Lett. 755, 137813 (2020). https:// doi. org/ 10. 1016/j. cplett. 2020. 137813

[21] D. Gao, L. Wang, X. Su et al., The role of applied magnetic field in Co-doped ZnS thin films fabricated by pulsed laser deposition. Opt. Mater. 114, 110877 (2021). https:// doi. org/ 10. 1016/j. optmat. 2021. 110877

[22] Y. Pina-Perez, O. Aguilar-Martinez, P. Acevedo-Pena et al., Novel ZnS-ZnO composite synthesized by the solvothermal method through the partial sulfidation of ZnO for $H_2$ production without sacrificial agent. Appl. Catal. B 230, 125–134 (2018). https:// doi. org/ 10. 1016/j. apcatb. 2018. 02. 047

[23] Uzun Cam, Ş., Serin, T., Yazıcı, A.N.: Effect of Sn doping concentration on structural, optical and electrical properties of ZnS/p-Si (111) diodes fabricated by sol-gel dip-coating

method. Mater Sci Semicond Process 127, 105693 (2021). https:// doi. org/ 10. 1016/j. mssp. 2021. 105693

[24] M. Xin, L.M. Liao, F. Han, Optical properties of ZnS: Ce nanocrystals prepared by hydrothermal method. J Lumin 238, 118074 (2021). doi: https://d oi. org/ 10. 1016/j.j lumin. 2021. 118074

[25] J.S. Bradley, B. Tesche, W. Busser et al., Surface spectroscopic study of the stabilization mechanism for shape-selectively synthesized nanostructured transition metal colloids. J. Am. Chem. Soc. 122, 4631–4636 (2000). https:// doi. org/ 10. 1021/ ja992 409y

[26]G. Hosseinzadeh, A. Maghari, S.M.F. Farniya et al., Interaction of insulin with colloidal ZnS quantum dots functionalized by various surface capping agents. Mater. Sci. Eng. C 77, 836–845 (2017).https:// doi. org/ 10. 1016/j. msec. 2017. 04. 018

[27] N. Mohamed, M. Amir, Z. Zaaboub et al., Effect of temperature and etching under light irradiation on the band edge emission of β-mercaptoethanol-capped CdS colloidal nanocrystals. J. Mater. Sci.: Mater. Electron. 31, 2416–2427 (2020). https:// doi. org/ 10. 1007/ s10854- 019- 02777-w

[28] N. Brahim, M. Poggi, J.C. Lambry et al., Density of grafted chains in thioglycerol-capped CdS quantum dots determines their interaction with aluminum(III) in water. Inorg. Chem. 57, 4979–4988 (2018). https:// doi. org/ 10. 1021/ acs. inorg chem. 7b032 54

[29] N. Brahim, N. Mohamed, M. Poggi et al., Interaction of L-cysteine functionalized CdSe quantum dots with metallic cations and selective binding of cobalt in water probed by fluorescence. Sens. Actuators B 243, 489–499 (2016). https:// doi. org/ 10. 1016/j. snb. 2016. 12. 003

[30] Y. Yu, L. Xu, J. Chen, H. Gao, S. Wang, J. Fang, S. Xu, Hydrothermal synthesis of GSH–TGA co-capped CdTe quantum dots and their application in labeling colorectal cancer cells. Colloids. Surf. B 95, 247–253 (2012). https:// doi. org/ 10. 1016/j. colsu rfb. 2012. 03. 011

[31]S. Ouni, N. Mohamed, M. Bouzidi et al., High impact of thiol capped ZnS nanocrystals on the degradation of single and binary aqueous solutions of industrial azo dyes under sunlight. J. Environ. Chem. Eng. 9, 5915 (2021). https:// doi. org/ 10. 1016/j. jece.
2021. 105915

[32] M. Adoni, M. Yadam, S. Gaddam et al., Antimicrobial, antioxidant, and dye degradation properties of biosynthesized silver nanoparticles from Artemisia Annua L. Lett. Appl. NanoBioSci. 10, 1981–1992 (2021). https:// doi. org/ 10. 33263/ LIANB S101. 19811 992

[33] S. Kannan, N.P. Subiramaniyam, M. Sathishkumar, A novel green synthesis approach for improved photocatalytic activity and antibacterial properties of zinc sulfide nanoparticles using plant extract of Acalypha indica and Tridax procumbens. J. Mater. Sci. Mater. Electron. 31, 9846–9859 (2020). https:// doi. org/ 10. 1007/ s10854- 020- 03529-x

[34] M. Biruntha, J. Archana, K. Kavitha et al., green synthesis of zinc sulfide nanoparticles using Abrus precatorius and its effect on coelomic fluid protein profile and enzymatic activity

of the earthworm, Eudrilus eugeniae. BioNanoScience 10, 149–156 (2020). https:// doi. org/ 10. 1007/ s12668- 019- 00694-0

[35] H.R. Rajabi, F. Sajadiasl, H. Karimi, Z.M. Alvand, Green synthesis of zinc sulfide nanophotocatalysts using aqueous extract of Ficus Johannis plant for efficient photodegradation of some pollutants. J. Mater. Res. Technol. 9, 15638–15647 (2020). https:// doi. org/ 10. 1016/j. jmrt. 2020. 11. 017

[36] S.C. Tudu, J. Kusz, M. Zubko, A. Bhattacharjee, Structural, morphological and optical characterization of green synthesized ZnS nanoparticles using Azadirachta Indica (Neem) leaf extract. Int. J. Nano Dimens. 11, 99–111 (2020)

[37] R. Belhattab, L. Amor, J.G. Barroso et al., Essential oil from Artemisia herba-alba Asso grown wild in Algeria: variability assessment and comparison with an updated literature survey. Arab. J. Chem. 7, 243–251 (2014). https:// doi. org/ 10. 1016/j. arabjc. 2012. 04. 042

[38] M. Mojarrab, A. Delazar, S. Esnaashari, F.H. Afshar, Chemical composition and general toxicity of essential oils extracted from the aerial parts of Artemisia armeniaca Lam. and A. incana (L.) Druce growing in Iran. Res. Pharm. Sci. 8, 65–69 (2013)

[39] A. Asdadi, A. Hamdouch, S. Gharby, L.M.I. Hassani, Journal of Analytical Sciences and Applied Biotechnology 2, 2 (2020). https:// doi. org/ 10. 48402/ IMIST. PRSM/ jasab- v2i2. 21589

[40] K.S. Bora, A. Sharma, The Genus Artemisia: a comprehensive review. Pharm. Biol. 49, 101–109 (2011). https:// doi. org/ 10. 3109/ 13880 209. 2010. 497815

[41]Y. Aniya, M. Shimabukuro, M. Shimoji et al., Antioxidant and hepatoprotective actions of the medicinal herb Artemisia campestris from the Okinawa Islands. Biol. Pharm. Bull. 23, 309–312 (2000). https:// doi. org/ 10. 1248/ bpb. 23. 309

[42] M.J. Abad, L.M. Bedoya, L. Apaza, P. Bermejo, The Artemisia L. Genus: a review of bioactive essential oils. Molecules 17, 2542–2566 (2012). https:// doi. org/ 10. 3390/ molec ules1 70325 42

[43] T. El-lamey, A. Kamel, E. Elsharkawy, Volatile oils content of some species of Artemisia growing under different environmental conditions and its effect on germination of seeds of some plants. IOSR J. Agric. Vet. Sci. 11, 83 (2018). https:// doi. org/ 10. 9790/ 2380- 11120 28393.

[44] P. Parameswari, R. Devika, P. Vijayaraghavan, In vitro anti-inflammatory and antimicrobial potential of leaf extract from Artemisia nilagirica (Clarke) Pamp. Saudi J. Biol. Sci. 26, 460 (2019). https:// doi. org/ 10. 1016/j. sjbs. 2018. 09. 005

[45] H. Dai, N. Feng, J. Li et al., Chemiresistive humidity sensor based on chitosan/zinc oxide/single-walled carbon nanotube composite film. Sens. Actuators B 283, 786–792 (2019). https:// doi. org/ 10. 1016/j. snb. 2018. 12. 056

[46] I. Aranaz, A.R. Alcantara, M.C. Civera et al., Chitosan: an overview of its properties and applications. Polymers 13, 3256 (2021). https:// doi. org/ 10. 3390/ polym 13193 256

[47] F. Zouaoui, S. Bourouina-Bacha, M. Bourouina et al., Electrochemical sensors based on molecularly imprinted chitosan: A review. TrAC Trends Anal Chem 130, 115982 (2020). https://doi. org/ 10. 1016/j. trac. 2020. 115982

[48] Y. Jiang, J. Wu, Recent development in chitosan nanocomposites for surface-based biosensor applications. Electrophoresis 40, 2084–2097 (2019). https:// doi. org/ 10. 1002/ elps. 20190 0066

[49] F.I.M. Ali, S.T. Mahmoud, F. Awwad et al., Low power consumption and fast response H2S gas sensor based on a chitosan- CuO hybrid nanocomposite thin film. Carbohydr. Polym. 236, 6064 (2020). https:// doi. org/ 10. 1016/j. carbp ol. 2020. 116064

[50] N.L. Lukman Hekiem, A.A. Md Ralib, M.A. Mohd Hatta et al., Effect of chitosan dissolved in different acetic acid concentration towards VOC sensing performance of quartz crystal microbalance overlay with chitosan. Mater. Lett. 291, 9524 (2021). https:// doi. org/ 10. 1016/j. matlet. 2021. 129524

[51] A. Madaci, G. Raffin, M. Hangouet et al., A microconductometric ethanol sensor prepared through encapsulation of alcohol dehydrogenase in chitosan: application to the determination of alcoholic content in headspace above beverages. J. Mater. Sci.: Mater. Electron. 32, 17752–17763 (2021). https:// doi. org/ 10. 1007/ s10854- 021- 06311-9

[52] D. Amaranatha Reddy, C. Liu, R.P. Vijayalakshmi, B.K. Reddy, Effect of Al doping on the structural, optical and photoluminescence properties of ZnS nanoparticles. J. Alloys Compd. 582, 257–264 (2014). https:// doi. org/ 10. 1016/j. jallc om. 2013. 08. 051

[53] H. Asoufi, T. Al-Antary, A. Awwad, Biosynthesis and characterization of iron sulfide (FeS) nanoparticles and evaluation their aphicidal activity on the green peach aphid myzus persicae (Homoptera: aphididae). Fresenius Environ. Bull. 27, 7767– 7775 (2018)

[54] Q.F. Nafa, S.M. Hussin, W.F. Hamadi, Characterization of some active organic compound from Cold and Hot aqueous solvent and Study their Antibiotic of Artemisia herba-alba Asso plant oil. Egypt J. Chem. 64, 6691–6709 (2021). https:// doi. org/ 10. 21608/ejchem. 2021. 72074. 3587

[55] U.S. Senapati, D. Sarkar, Structural, spectral and electrical properties of green synthesized ZnS nanoparticles using Elaeocarpus floribundus leaf extract. J. Mater. Sci.: Mater. Electron. 26, 5783– 5791 (2015). https:// doi. org/ 10. 1007/ s10854- 015- 3137-6

[56] Y. Yu, L. Xu, J. Chen et al., Hydrothermal synthesis of GSH–TGA co-capped CdTe quantum dots and their application in labeling colorectal cancer cells. Colloids Surf. B 95, 247–253 (2012). https:// doi. org/ 10. 1016/j. colsu rfb. 2012. 03. 011

[57] M. Jothibas, C. Manoharan, S. Johnson Jeyakumar et al., Synthesis and enhanced photocatalytic property of Ni doped ZnS nanoparticles. Sol. Energy 159, 434–443 (2018). https:// doi. org/ 10. 1016/j. solen er. 2017. 10. 055

[58]B. Poornaprakash, U. Chalapathi, Y. Suh et al., Terbiumdoped ZnS quantum dots: structural, morphological, optical, photoluminescence, and photocatalytic properties. Ceram. Int. 44, 11724–11729 (2018). https:// doi. org/ 10. 1016/j. ceram int. 2018. 03. 250

[59]S. Ouni, N.B.H. Mohamed, N. Chaaben et al., Fast and effective catalytic degradation of an organic dye by eco-friendly capped ZnS and Mn-doped ZnS nanocrystals. Environ. Sci. Pollut. Res. 29, 33474–33494 (2022). https:// doi. org/ 10. 1007/ s11356- 021- 17860-1

[60] V. Mote, Y. Purushotham, B. Dole, Williamson-Hall analysis in estimation of lattice strain in nanometer-sized ZnO particles. J. Theor. Appl. Phys. 6, 6 (2012). https:// doi. org/ 10. 1186/ 2251- 7235-6-6

[61] H. Matsumoto, T. Sakata, H. Mori, H. Yoneyama, Preparation of monodisperse CdS nanocrystals by size selective photocorrosion. J. Phys. Chem. 100, 13781–13785 (1996). https:// doi. org/ 10. 1021/ jp960 834x

[62]A. Iqbal, U. Saidu, F. Adam, S. Sreekantan, N. Jasni, M.N. Ahmad, The effects of zinc oxide (ZnO) quantum dots (QDs) embedment on the physicochemical properties and photocatalytic activity of titanium dioxide ($TiO_2$) nanoparticles. JPS 32, 71 (2021). https:// doi. org/ 10. 21315/ jps20 21. 32.2.6

[63] N. Ben Brahim, M. Poggi, N.B. Haj Mohamed et al., Synthesis, characterization and spectral temperature-dependence of thioglycerol- CdSe nanocrystals. J. Lumin. 177, 402–408 (2016). https:// doi. org/ 10. 1016/j. jlumin. 2016. 05. 026

[64] J.R. Snider, G.A. Dawson, Tropospheric light alcohols, carbonyls, and acetonitrile: Concentrations in the southwestern United States and Henry's Law data. J. Geophys. Res. Atmos. 90, 3797–3805 (1985). https:// doi. org/ 10. 1029/ JD090 iD02p 03797

[65] Sander, R.: Compilation of Henry's Law Constants for Inorganic and Organic Species of Potential Importance in Environmental Chemistry, version 3, 8 Apr 1999 http://www.mpch-mainz.mpg. de∼sander\res\henry.html. Errata (collected from the above web site 4 June 2003) Wel. H - PHA KH H - PHA Thanks J C Wheel

[66] N. Lavanya, S.G. Leonardi, S. Marini et al., MgNi2O3 nanoparticles as novel and versatile sensing material for non-enzymatic electrochemical sensing of glucose and conductometric determination of acetone. J. Alloys Compd. 817, 152787 (2020). https:// doi. org/ 10. 1016/j. jallc om. 2019. 152787

[67] R. Krishna, J.M. Van Baten, Water/alcohol mixture adsorption in hydrophobic materials: enhanced water ingress caused by hydrogen bonding. ACS Omega 5, 28393–28402 (2020). https:// doi. org/ 10. 1021/ acsom ega. 0c044 91

[68] C.F. Fong, C.L. Dai, C.C. Wu, Fabrication and characterization of a micro methanol sensor using the CMOS-MEMS technique. Sensors 15, 27047–27059 (2015). https:// doi. org/ 10. 3390/ s1510 27047

[69] Q. Liu, J.R. Kirchhoff, Amperometric detection of methanol with a methanol dehydrogenase modified electrode sensor. J. Electroanal. Chem. 601, 125–131 (2007). https:// doi. org/ 10. 1016/j. jelec hem. 2006. 10. 039

[70] J. Van den Broek, S. Abegg, S.E. Pratsinis, A.T. Guntner, Highly selective detection of methanol over ethanol by a handheld gas sensor. Nat. Commun. 10, 4220 (2019). https:// doi. org/ 10. 1038/ s41467- 019- 12223-4

[71]K. Phasuksom, W. Prissanaroon-Ouajai, A. Sirivat, A highly responsive methanol sensor based on graphene oxide/polyindole composites. RSC Adv. 10, 15206–15220 (2020). https:// doi. org/ 10. 1039/ D0RA0 0158A

[72]Y. Li, D. Deng, X. Xing et al., A high performance methanol gas sensor based on palladium-platinum-$In_2O_3$ composited nanocrystalline $SnO_2$. Sens. Actuators B 237, 133–141 (2016). https:// doi. org/ 10. 1016/j. snb. 2016. 06. 088

[73] B. Mandal, Aaryashree, R. Singh, S. Mukherjee, Highly Selective and Sensitive Methanol Sensor Using Rose-Like ZnO Microcube and MoO3 Micrograss-Based Composite. IEEE Sens J 18, 2659– 2666 (2018). doi: https:// doi. org/ 10. 1109/ JSEN. 2018. 28036 82

[74] D. Acharyya, S. Acharyya, K. Huang et al., Highly sensitive ppb level methanol sensor by tuning C: O ratio of rGO-TiO2 nanotube hybrid structure. IEEE Trans. Nanotechnol. 16, 1122–1128 (2017). https:// doi. org/ 10. 1109/ TNANO. 2017. 27641 24

[75] K. Phasuksom, W. Prissanaroon-Ouajai, A. Sirivat, Electrical conductivity response of methanol sensor based on conductive polyindole. Sens. Actuators B 262, 1013–1023 (2018). https:// doi. org/ 10. 1016/j. snb. 2018. 02. 088

[76] I. Musa, G. Raffin, M. Hangouet et al., Electrospun PVC-nickel phthalocyanine composite nanofiber based conductometric methanol microsensor. Microchem. J. 182, 107899 (2022). https:// doi. org/ 10. 1016/j. microc. 2022. 107899

[77] I. Musa, G. Raffin, M. Hangouet et al., Development of a chitosan/ nickel phthalocyanine composite based conductometric microsensor for methanol detection. Electroanalysis 34, 1338–1347 (2022). https:// doi. org/ 10. 1002/ elan. 20210 0707

[78] A.A. Athawale, S.V. Bhagwat, P.P. Katre, Nanocomposite of Pd– polyaniline as a selective methanol sensor. Sens. Actuators B 114, 263–267 (2006). https:// doi. org/ 10. 1016/j. snb. 2005. 05. 009

# *Conclusion générale & Perspectives*

Au cours de cette thèse, nous avons étudié la préparation ainsi que les propriétés de NCs non toxiques et respectueux de l'environnement, qui sont susceptibles de constituer une alternative aux différents applications environnementales. Un échange de ligand a également été effectué sur les NCs de ZnS afin de passer de l'organique vers la chimie verte. La performance de ces nanocristaux a été valorisé par les applications dans la photocatalyse des polluants organiques et dans les capteurs de gaz.

***Dans la première partie de cette thèse,*** des nanocristaux de Sulfure de Zinc (ZnS) ont été préparés en utilisant une voie colloïdale aqueuse avec de l'acide thioglycolique (TGA) comme stabilisant. Ces nanocristaux de ZnS-TGA ont été utilisés comme alternative peu coûteuse et respectueuse de l'environnement pour la photodégradation du bleu de méthylène et de l'orange de méthyle à partir de solutions aqueuses par irradiation solaire. Les propriétés structurelles et optiques des nanocristaux ont été déterminées par diffraction des rayons X, spectroscopie infrarouge à transformée de Fourier, microscopie électronique à transmission, spectroscopie UV-Visible et photoluminescence. Les résultats ont montré un décalage vers le bleu de la bande d'absorbance et des valeurs de bande interdite d'énergie plus élevées que les matériaux ZnS massifs, ce qui était en accord avec l'effet de confinement quantique. La diffraction des rayons X a confirmé la formation d'une phase cubique de ZnS-TGA contenant également une légère phase wurtzite. La taille moyenne calculée des nanocristaux de ZnS par la relation Debye Scherrer était de 3,5 nm. Les résultats de la caractérisation ont montré la fixation de TGA sur les NCs de ZnS via des fonctionnalités soufrées et carboxyliques à la surface du catalyseur. Les spectres de photoluminescence obtenus sous une longueur d'onde d'excitation à 325 nm ont montré trois bandes d'émission (416, 441 et 484 nm), qui étaient principalement liées au bord de bande et aux émissions activées par défaut. L'activité photocatalytique des nanocristaux de ZnS-TGA sous irradiation solaire pour dégrader les colorants MB et MO testés et leur mélange dans des solutions aqueuses a été évaluée. Une efficacité élevée de dégradation du colorant a été obtenue en très peu de temps (27 min) et cette performance a été attribuée à la charge de surface négative, à la surface, aux défauts de surface et à la forte dispersion des nanocristaux de ZnS-TGA sur le milieu aquatique. Dans l'ensemble, cette étude démontre que ces nanocristaux pourraient être utilisés comme nanocatalyseurs à faible coût pour la dégradation des colorants organiques dans le traitement des eaux usées.

***Dans la deuxième partie de cette thèse,*** Nous rapportons une voie facile et verte pour une nouvelle synthèse de nanoparticules de ZnS à l'aide d'extrait de plante d'Artemisia Herba Alba (AHA) pour une adsorption/photodégradation efficace du colorant bleu de méthylène. Les

résultats ont montré un décalage vers le bleu dans la bande d'absorbance et des valeurs de bande interdite d'énergie plus élevées que les matériaux ZnS massifs, ce qui était dû aux effets de confinement quantique. La diffraction des rayons X a confirmé la formation de la phase cubique de nanocristaux de ZnS-AHA avec une taille moyenne calculée de 4 nm. Les NPs de ZnS synthétisées vertes montrent une efficacité d'adsorption améliorée de MB. Les NPs de ZnS-AHA ont montré une surface spécifique de 36,82 cm2 $g^{-1}$ et une capacité d'adsorption de 31,17 mg $g^{-1}$ pour bleu de méthylène. Le modèle Langmuir–Freundlich a été utilisé pour extraire les données d'adsorption. Les performances de dégradation photocatalytique des nanoparticules vertes sous irradiation solaire ont montré un taux de dégradation remarquable du colorant de 94,09 % en 180 min. En résumé, ces nouveaux matériaux, respectueux de l'environnement, représentent une alternative très prometteuse dans le traitement des eaux usées pour l'élimination des composés organiques.

***Dans la dernière partie de cette thèse,*** Un transducteur microconductométrique est proposé pour la détection de vapeur de méthanol. La partie sensible de ce microcapteur de méthanol est préparée par encapsulation de nanoparticules de ZnS dans le chitosane. Les NPs de ZnS ont été préparées par voie colloïdale aqueuse, l'extrait de plante d'Artemisia Herba Alba (AHA) étant utilisé comme stabilisant. Ces nanoparticules ont été largement caractérisées et les résultats ont démontré que les AHA étaient des stabilisants efficaces pour produire directement une dispersion aqueuse de NPs de ZnS avec une taille moyenne de nanocristaux de 3,93 nm. Un film mince de composite chitosane/ZnS-NPs a été électrodéposé sur les électrodes d'or interdigitées par essai chrono-ampérométrique. Les réponses de détection de gaz d'éthanol, de méthanol et d'acétone des films ont été mesurées à température ambiante, par des mesures conductométriques différentielles à 10 kHz. Le temps de réponse des capteurs ($t_{Rep}$) pour le méthanol est de 11 à 25 s des concentrations les plus faibles aux plus élevées. La limite de détection du méthanol est de 1400 ppm en phase gazeuse. Le capteur de méthanol présente une sensibilité 3,8 fois plus faible pour l'éthanol et 30 fois plus faible pour l'acétone. La durée de conservation du capteur de méthanol est d'un mois.

***Parmi les perspectives envisagées pour ce travail***, nous pouvons citer :

- Étude de l'effet de la modification de la surface des NCs en utilisant d'autre types des ligans à base des extraits de plantes comme Artemisia campestris et le juniperus communis sur les propriétés et sur les différentes applications visées.

- Réaliser le dopage des NCs ZnS avec des ions métalliques tels que $Co^{2+}$ ou $Ni^{2+}$ dans le but de les doter de propriétés magnétiques et permettre leur utilisation comme sondes bimodales pour des applications en bioimagerie.
- Développer d'autres nanocristaux par la chimie verte comme $Fe_3O_4$, ZnSe et étudier leurs performances dans les applications de photocatalyse et les capteurs de gaz.
- Exploiter les propriétés de fluorescences de nanocristaux synthétisés pour faire la détection des gaz sous irradiation.

## Liste des publications :


[1] S. Ouni, N. Bel Haj Mohamed, M. Bouzidi, A. Bonilla-Petriciolet, M. Haouari, High impact of thiol capped ZnS nanocrystals on the degradation of single and binary aqueous solutions of industrial azo dyes under sunlight, J. Environ. Chem. Eng. 9 (2021) 105915. https://doi.org/10.1016/j.jece.2021.105915.

[2] S. Ouni, N. Mohamed, N. Chaaben, A. Bonilla-Petriciolet, M. Haouari, Fast and effective catalytic degradation of an organic dye by eco-friendly capped ZnS and Mn-doped ZnS nanocrystals, Environ. Sci. Pollut. Res. (2022). https://doi.org/10.1007/s11356-021-17860-1.

[3] N. Bel Haj Mohamed, S. Ouni, M. Bouzid, M. Bouzidi, A. Bonilla-Petriciolet, M. Haouari, Synthesis and preparation of acid capped CdSe nanocrystals as successful adsorbent and photocatalyst for the removal of dyes from water and its statistical physics analysis, Environ Sci Pollut Res. 29 (2022) 72747–72763. https://doi.org/10.1007/s11356-022-20990-9.

[4] N. Bel Haj Mohamed, M. Bouzidi, S. Ouni, A.S. Alshammari, Z.R. Khan, M. Gandouzi, M. Mohamed, N. Chaaben, A. Bonilla-Petriciolet, M. Haouari, Statistical physics analysis of adsorption isotherms and photocatalysis activity of MPA coated CuInS2/ZnS nanocrystals for the removal of methyl blue from wastewaters, Inorganic Chemistry Communications. 144 (2022) 109933. https://doi.org/10.1016/j.inoche.2022.109933.

[5] S. Ouni, N.B.H. Mohamed, M. Haouari, A. Elaissari, A. Errachid, N. Jaffrezic-Renault, A Novel Green Synthesis of Zinc Sulfide Nano-Adsorbents Using Artemisia Herba Alba Plant Extract for Adsorption and Photocatalysis of Methylene Blue Dye, Chemistry Africa. (2023). https://doi.org/10.1007/s42250-023-00667-7.

[6] S. Ouni, A. Madaci, M. Haouari, N.B.H. Mohamed, F. Bessueille, A. Elaissari, A. Errachid, N. Jaffrezic-Renault, A Novel Conductometric Micro-sensor for Methanol Detection Based on Chitosan/Zinc Sulfide-Nanoparticles Composite Obtained by Green Synthesis, J Inorg Organomet Polym. (2023). https://doi.org/10.1007/s10904-023-02696-8.

# *Annexe : Techniques de caractérisation*

Les techniques de caractérisation structurales et optiques utilisées pour la caractérisation des NCs synthétisés au cours de cette thèse sont les suivantes :

- **Spectroscopie UV-Visible**

La spectroscopie UV-visible est une méthode d'analyse qui permet principalement de mesurer l'absorbance (appelée aussi densité optique D.O.) d'une substance chimique donnée en solution à l'aide d'un spectrophotomètre.
Les spectres d'absorption UV-Visible des différentes solutions de NCs ont été mesurés avec un spectrophotomètre UV-visible SPECORD 210 Plus.

- **Spectroscopie de photoluminescence (PL)**

La spectroscopie de photoluminescence est une technique de caractérisation optique permettant de caractériser les propriétés luminescentes des matériaux.
Les spectres d'émission de photoluminescence (PL) dans cette thèse ont été enregistrés en utilisant comme source d'excitation de laser hélium-cadmium (325 nm) à température ambiante.

La mesure de la fluorescence couplée à celle de l'absorption permet de calculer le rendement quantique de photoluminescence des nanomatériaux préparés par rapport à une référence qui peut être un colorant organique tel que la fluorescéine ou la rhodamine.

- ## Spectroscopie infrarouge à transformée de Fourrier (FTIR)

La spectroscopie infrarouge à transformée de fourrier (FT-IR : Fourier Transformation Infra-Red spectroscopy en anglais) est une méthode d'analyse vibrationnelle de la matière permettant l'identification des fonctions chimiques présentent à la surface des NCs.
Les mesures FT-IR dans cette thèse, ont été réalisées en mode transmission à température ambiante à l'aide d'un spectrophotomètre Perkin Elmer version 5.3 dans la gamme spectrale de 400 à 4000 cm-1 à l'aide de disques de pastilles KBr.

- ## La diffraction des rayons X (DRX)

La diffraction de rayon X (DRX) est une technique qui permet d'identifier la structure cristalline des NCs en poudre et elle est utilisée principalement pour l'identification des phases existante dans un matériau. La DRX permet également d'avoir des informations sur les paramètres de maille, la taille des cristallites et de déterminer les positions des atomes qui constituent le matériau.
Les diagrammes de DRX dans cette thèse, ont été enregistrés à l'aide d'un diffractomètre Panalytical X'Pert Pro en utilisant un rayonnement Cu Kα ($\lambda$ = 0, 1542 nm). Les échantillons ont été placés sur un support d'échantillon en silicium et les mesures ont été enregistrés à température ambiante.

- ## La microscopie électronique à transmission et de haute résolution (MET et HR-MET)

La microscopie électronique à transmission est une technique de caractérisation structurale et microstructurale indispensable pour l'étude des matériaux à l'échelle nanométrique. Elle permet d'évaluer la dispersion et la taille des NCs et d'enregistrer des diagrammes de diffraction des électrons.
Les mesures de microscopie électronique à transmission (MET) et de haute résolution (HR-MET) ont été effectuées à l'aide d'un instrument Electron FEI Tecnai G2 et JEM-2100 analytical electron fonctionnant à 200 kV. Une goutte d'une solution de NCs dispersés dans l'eau, est déposée sur une grille de cuivre supportée par un film de carbone. Un faisceau d'électrons de forte énergie (10 à 100 keV) est envoyé pour traverser cette goutte, conduisant à l'obtention sur le film photographique d'une image ou d'un diagramme de diffraction électronique des particules.

À haute résolution (HR-TEM), cette technique permet d'identifier le type de réseau cristallin d'une nanoparticule, les défauts d'empilement ainsi que le changement de phase à l'échelle de la maille cristalline.

- **La spectroscopie de rayons X à dispersion d'énergie (EDX ou EDS)**

La spectroscopie de rayons X à dispersion d'énergie (EDX ou EDS) est une technique utilisée en science des matériaux et en chimie analytique pour analyser la composition élémentaire d'un échantillon. Il est souvent associé à la microscopie électronique à balayage ou transmission (SEM/TEM) pour fournir à la fois des capacités d'imagerie et d'analyse élémentaire.

La spectroscopie EDX peut fournir des informations qualitatives et quantitatives sur les éléments présents dans un échantillon. Qualitativement, il peut identifier les éléments en comparant les pics d'énergie dans le spectre aux énergies de rayons X connues de différents éléments.

Les images de EDX dans cette thèse, ont été enregistrés à l'aide d'un microscope électronique à balayage Tescan Vega SBU, fonctionnant à une tension d'accélération de 20 kV, équipé d'un détecteur Bruker Esprit Compact EDS et à l'aide d'un microscope électronique à transmission Electron FEI Tecnai G2 et JEM-2100 analytical electron fonctionnant à 200 kV .

## *Liste des figures*

### *Chapitre I*



### *Chapitre II*

## *Chapitre III*

## *Chapitre IV*

***Figure IV.S2***: Flow-chart for the process of fabrication of microconductometric chips.

***Figure IV. S3***: Flow-chart for the process of fabrication of microconductometric chips.

***Figure IV. S4***: Chronoamperometric measurement monitoring of electrodeposition of chitosan.

***Figure IV S5***: Diagram of the experimental setup.

***Figure IV. S6***: Effect of the presence of 1/5 of ethanol and of acetone compared to methanol on the sensor signal.

***Figure IV. S7***: Detection of gas-phase concentrations for different methanol/water solutions and commercial ice washer product, with the chitosan/ZnS-NPs sensor.

## *Liste des tableaux*

### *Chapitre I*



### *Chapitre II*



### *Chapitre III*



### *Chapitre IV*

***Table IV.1***: Response times and detection limits of previously published methanol sensors based on various materials.

***Table IV.S1***: Equilibrium gaseous phase concentrations above aqueous methanol, ethanol, and acetone solution at 25 ◦C per Henry's law constants reported by Sander et al [65].